Viscous Damping of Moored Containership in Confined Berths

An Experimental Investigation of Viscous Damping of a Containership Moored at Low Under Keel Clearance Alongside a Quay Wall

Master of Science Thesis

Christina Troullou



TU Delft

Haskoning
Enhancing Society Together

Viscous Damping of Moored Containership in Confined Berths

An Experimental Investigation of Viscous Damping of a Containership Moored at Low Under Keel Clearance Alongside a Quay Wall

by

Christina Troullou

Supervisor TU Delft:	Dr. Sebastian Schreier
Supervisor Haskoning:	Dr. Alex van Deyzen
Faculty:	Faculty of Mechanical Engineering, TU Delft

Cover Image by International Institute of Marine Surveying [1]

TU Delft

Haskoning
Enhancing Society Together

Acknowledgements

This thesis concludes my MSc in Offshore and Dredging Engineering at Delft University of Technology, and I would like to thank those who contributed to it.

First of all, I would like to express my sincere gratitude to my supervisors, Sebastian Schreier from TU Delft and Alex van Deyzen from Haskoning, for their guidance throughout this project. They encouraged me to look at the broader picture rather than only the details, and helped me find my way whenever I lost direction. Their feedback greatly improved this work. I am also grateful to Peter Wellens for being part of my graduation committee and for the time he dedicated to this thesis, and to Haskoning for the opportunity to carry out this research within the company.

The experimental work would not have been possible without the help of others. I would like to thank Jasper den Ouden for building the model, and Pascal Taudin Chabot, Angela Piras and Vittorio Garofano for their assistance and advice during the experiments.

Finally, I am deeply grateful to my friends and family for their support throughout my studies. A special thanks goes to the friends who went beyond moral support and spent their own time in the laboratory helping me run the experiments. Their help made a real difference, and it is something I will not forget.

Christina Troullou
Delft, November 2026

Summary

Large container ships are often moored with a small under keel clearance (UKC) and a narrow gap to the quay wall. In dynamic mooring analysis, the viscous damping of their low frequency sway and yaw motions is usually neglected or taken from model tests under different conditions, and no experimental data existed for a vessel close to a quay wall at a draft to water depth ratio T/h above 0.73. This thesis investigates how this viscous damping changes with lateral and vertical confinement.

A test campaign was carried out with a box-shaped model of a container ship at a scale of 1:87. Moored decay tests in sway and yaw covered T/h of 0.70, 0.80 and 0.90 and gap to beam ratios G/B of 0.079 to 0.160, together with a laterally unconfined reference. The equivalent linear viscous damping was identified by fitting the equation of motion to each decay and subtracting the potential damping, computed with DIFFRAC, and the damping of the mooring pulleys, measured in dry tests.

The viscous damping was found to form most of the total damping in both sway and yaw. It increased as the UKC became smaller, already without the quay wall, and increased further as the gap to the quay wall was reduced. In the most confined case, the damping was about three times larger in sway and in yaw than in the least confined case. The added mass followed the trend of the potential added mass with confinement. Its values were lower than the DIFFRAC values, and the added mass of the second half-cycle was lower than that of the first, which shows a dependence on the amplitude of the motion.

These findings show that confinement has a considerable effect on the viscous damping of a moored vessel, and that damping values should be determined for the vessel and the confinement of the berth. The measurements extend the available data to smaller under keel clearances and can serve as a reference for numerical models. Since the tests were scaled according to Froude, the values are an upper limit for full scale. Forced oscillation tests at the natural periods of the moored vessel, together with measurements of the flow in the gap and under the keel, would identify the added mass and the damping more accurately and explain the amplitude dependence of the added mass. The scale effect could be addressed with computational fluid dynamics at the Reynolds number of the full-scale vessel, using the measurements of this thesis for validation, or with tests of the same configuration at a different scale.

Contents

Acknowledgements i

Summary ii

Nomenclature xii

1 Introduction 1
- 1.1 Evolution and Scaling of Global Shipping . . . 1
- 1.2 Infrastructural and Operational Constraints . . . 1
- 1.3 Project Collaboration . . . 2
- 1.4 Problem Statement . . . 3
- 1.5 Defining Close Proximity . . . 3
- 1.6 Research Objective and Questions . . . 4
- 1.7 Methodological Approach . . . 4
- 1.8 Thesis Outline . . . 5

2 Literature Review 7
- 2.1 Origins in Offshore Engineering . . . 7
- 2.2 Shallow Water Confinement . . . 8
- 2.3 Combined Lateral and Vertical Confinement . . . 8
- 2.4 Computational Fluid Dynamics . . . 9
- 2.5 Research Gap . . . 10

3 Theory 12
- 3.1 Potential Flow Theory . . . 12
  - 3.1.1 Frequency Domain . . . 12
  - 3.1.2 Time Domain: Cummins Equation . . . 13
- 3.2 Equations of Motion for a Moored Vessel . . . 13
- 3.3 Damping Decomposition . . . 14
  - 3.3.1 Potential Damping . . . 15
  - 3.3.2 Viscous Damping . . . 15
  - 3.3.3 Pulley Damping . . . 15
- 3.4 Scaling Laws . . . 16
  - 3.4.1 Correction for Viscous Scale Effects . . . 16

4 Experiment 18
- 4.1 Design Choices . . . 18
  - 4.1.1 Degrees of Freedom . . . 18
  - 4.1.2 Model Geometry and Test Method . . . 18
  - 4.1.3 Facility Selection . . . 19
  - 4.1.4 Scale and Test Cases . . . 19

4.2 Test Facility . . . 20
4.3 Model Vessel . . . 22
4.3.1 Construction . . . 22
4.3.2 Dry Testing . . . 22
4.3.3 Ballasting . . . 23
4.4 Mooring System . . . 25
4.4.1 Target Stiffness . . . 25
4.4.2 Spring and Pulley Arrangement . . . 25
4.5 Pulley Calibration . . . 26
4.6 Experimental Design and Layout . . . 27
4.7 Instrumentation . . . 29
4.8 Test Procedure . . . 30
4.9 Raw Data . . . 31

5 Data Processing and Viscous Damping Extraction 33
5.1 Total Damping from Moored Decay Tests . . . 33
5.1.1 Release Detection, Trimming and Zero Centering . . . 33
5.1.2 Sway and Yaw at the Center of the Model . . . 34
5.1.3 Filtering . . . 35
5.1.4 Equation of Motion Fit . . . 36
5.1.5 Period of the Decay . . . 37
5.1.6 Amplitude Dependent Added Mass . . . 39
5.1.7 Quadratic Damping . . . 40
5.2 Pulley Damping from the Dry Tests . . . 42
5.3 Potential Damping from DIFFRAC . . . 45
5.4 Normalization . . . 46

6 Results 48
6.1 Comparison of the two methods: added mass and damping . . . 48
6.1.1 Added Mass . . . 48
6.1.2 Total Damping and Fit Quality . . . 51
6.2 Viscous Damping . . . 52
6.3 Normalized added mass and damping . . . 53
6.4 Sway Case 6 . . . 55

7 Discussion 57
7.1 Effect of confinement on the viscous damping . . . 57
7.2 Comparison with Literature . . . 57
7.3 Scale effects and transfer to full scale . . . 58
7.4 Added Mass . . . 59
7.5 Limitations of the damping analysis . . . 60

8 Conclusions and Future Work **61**
8.1 Conclusions . . . 61
8.2 Future Work . . . 62

AI Statement **64**

A Experiment **70**
A.1 Additional Photographs of the Setup . . . 70
A.2 Facility Documentation . . . 73
A.3 Mass Properties and Ballasting . . . 74
A.3.1 Yaw Inertia via Torsional Swing Test . . . 75
A.3.2 Ballast Placement . . . 75
A.4 Mooring Stiffness Derivation . . . 76
A.4.1 Line Stiffness Projection . . . 77
A.4.2 Full Scale Stiffness Comparison . . . 78
A.4.3 Froude Scaling of the Target Stiffness . . . 78
A.4.4 As-Built Spring Stiffness . . . 79
A.4.5 Spring Calibration . . . 79
A.5 Instrumentation Specifications . . . 79
A.5.1 OptiTrack Motion Capture . . . 80
A.5.2 Panasonic HG-C1100 Laser Sensor . . . 81
A.5.3 Micro-Epsilon optoNCDT 1420 Laser Sensor . . . 82
A.5.4 Electromagnet Release Mechanism . . . 82
A.5.5 Bench Power Supplies . . . 82
A.5.6 Laser Calibration Coefficients . . . 83

B Data Processing **84**
B.1 Release Detection and Zero Centering . . . 84
B.2 Comparison of the Camera with the Laser Reconstruction . . . 84
B.3 Filtering . . . 84
B.4 Quadratic Damping . . . 85
B.4.1 Convergence of the Fit . . . 87
B.5 Convergence for All Cases . . . 91
B.6 Dry Test Pendulum . . . 94
B.7 DIFFRAC Calculations . . . 94
B.7.1 Quay and Damping Lid . . . 94
B.7.2 Mesh Convergence . . . 95

C Results **98**
C.1 Decay fits per case . . . 98

D Cruise Ship **104**
D.1 Vessel Properties . . . 104
D.2 Mooring Options . . . 104

D.3 Planned Test Matrix 105

List of Figures

1 Comparative evolution of maritime vessel designs. 2

2 Schematic illustration of the close proximity problem: (a) plan view showing the lateral gap G, and (b) cross section view showing both the lateral gap G and the under keel clearance UKC. Only the submerged part of the hull is drawn in (b). 4

3 Overview of the research methodology. 6

4 Reviewed literature and this thesis by confinement level. Gray band: cases without a lateral boundary or with G/B above 0.3. 11

5 Definition of the body fixed coordinate system and the six degrees of freedom: surge (x), sway (y), heave (z), roll (ϕ), pitch (θ), and yaw (ψ). 12

6 Illustration of the viscous effects acting on a vessel, highlighting the distinction between eddy making and skin friction components. 15

7 The Wave Flume Tank before and after the installation of the wooden quay wall. 21

8 Rhino model of the box shaped vessel, showing the internal compartments and the backbone with mooring attachment points, used to calculate the target mass properties. . 22

9 The unballasted model prepared for the dry test, showing the plywood extension and the temporary suspension hooks mounted symmetrically about the measured center of gravity. 23

10 Lead ballast blocks positioned inside the hull, labeled with their individual masses. . . . 24

11 The marked required waterline aligning with the actual waterline after ballasting. 24

12 Pulleys at one mooring station, mounted on the aluminum frame above the flume. Each redirects the string from its spring (mounted further up the frame, not visible here) into a horizontal line of action toward the backbone. 26

13 Dry test of one spring and pulley set, isolated for moored decay testing. 27

14 Top view of the test layout for Case 12, showing the backbone with the electromagnet mounting brackets at each end and the wooden quay wall. All dimensions are in cm. . . . 28

15 Side View of the test layout for Case 12, defining the water depth h, model draft T, and under keel clearance. All dimensions are in mm. 28

16 Photographs of the assembled test setup in the flume. 29

17 Raw laser and OptiTrack signals for Case 2 ($h = 172$ mm, $G = 69$ mm). The two upper panels show the lasers and the remaining panels the OptiTrack signals at the center of the deck. 32

18 Comparison of the camera signal with the laser reconstruction at the center of the model, for a sway run (a) and a yaw run (b) of Case 2, after trimming and zero centering. 35

19 Effect of the filters on the raw signal of a sway run (a) and a yaw run (b) of Case 2. . . . 36

20 Measured decay and fit of the equation of motion with a constant added mass and free damping coefficients B_1 and B_2, for a sway run (a) and a yaw run (b) of Case 12. 37

21 Half-cycles of the filtered signal for a sway run (a) and a yaw run (b) of Case 2. The triangles mark the peaks and the troughs, and the shaded areas the first three half-cycles with their durations $T_{1/2}$. 38

22 Sway decay of run 157 of Case 4, fitted with B_2 free and with $B_2 = 0$ in Method 1 (left) and Method 2 (right). Values: B_1 [N s/m], B_2 [N s^2/m^2], RMSE [mm]. 42

23 Dry test of the aft springs and pulleys for one run: displacement (top) and period of every cycle (bottom). 43
24 Measured displacement and fit of Equation 28 for one run of the aft set. The fit ends where the amplitude has fallen to 2 mm (vertical line). 44
25 Panel mesh of the hull and the two flume walls of an unconfined case, visualized in ParaView. 46
26 Added mass per half-cycle against confinement, sway (case mean ± sd). 49
27 Added inertia per half-cycle against confinement, yaw (case mean ± sd). 50
28 Measured decay and the fits of both methods: sway case 9 (run 357) and yaw case 10 (run 332). Method 1 restarts each half-cycles at the measured turning point. 52
29 Normalized viscous damping against the gap (left) and the water depth (right), sway (top) and yaw (bottom). Dashed lines: unconfined cases. 54
30 Normalized added mass of the first half-cycle against the gap (left) and the water depth (right), sway (top) and yaw (bottom). Dashed lines: unconfined cases. 55
31 Normalized viscous damping against the gap: this study and De Boer and Buchner [2]. Dashed lines: unconfined cases and tests without the structure. Logarithmic vertical axis. 58
32 Overview of the assembled setup from above, showing the model with its backbone and the metal frame at each end, which slides across the flume on the aluminium profile. . . . 70
33 One end of the model seen from above, showing the electromagnet, the bolt mounted on the backbone extender that engages it, the springs attached to the backbone, and the two pulleys that redirect them. 71
34 Setting the lateral gap, with the 69 mm aluminium spacer fitted between the reference bracket and the sliding unit. 71
35 Verification of the gap, with the aluminium spacer fitted between the model and the wooden wall. 72
36 The stainless steel ruler mounted on the wooden wall, used as a fixed reference for measuring the water depth. 72
37 The laser sensor, mounted above the pulley on a plate that extends towards the model, at the fore of the model. The sliding frame carrying the pulley and the vertical spring holder is visible alongside. 73
38 Close up of the flume bottom, showing the weld seam bump and the thin algae layer covering the tank floor. 74
39 Close up of the flume wall, showing the wall bump. 74
40 Plan view of the ballast layout, aft on the left and fore on the right. All dimensions in mm. 76
41 General arrangement of the reference container ship, annotated with the mooring line layout used to derive the target stiffness. 76
42 Projection of a single mooring line's axial force onto the vessel's motion, following the geometry of Figure 41. A displacement x stretches the line by $x\cos\Theta$, producing a line force $F_s = kx\cos\Theta$ whose component along x is $F_x = F_s\cos\Theta = kx\cos^2\Theta$, so the line contributes a stiffness $k\cos^2\Theta$ to that direction. 77
43 Calibration setup. 80
44 The OptiTrack cameras, mounted on aluminium profiles at the ceiling above the flume. . 80

45 Top view of the deck showing the OptiTrack marker positions and the centre of the rigid body, to which the measured motions are referenced. Dimensions in cm. 81
46 Bench power supplies used for the instrumentation. 83
47 Sway decay of the run with the largest quadratic damping in Cases 2, 3 and 6, fitted with B_2 free and with $B_2 = 0$ in Method 1 (left) and Method 2 (right). Values: B_1 [N s/m], B_2 [N s^2/m^2], RMSE [mm]. 86
48 Method 1: B_1 with $B_2 = 0$ against the iteration. Dashed line: best value. 88
49 Method 1: B_1 with B_2 free against the iteration. Dashed line: best value. 88
50 Method 1: B_2 (free) against the iteration. Dashed line: best value. 89
51 Method 2: B_1 with $B_2 = 0$ against the iteration. Dashed line: best value. 89
52 Method 2: B_1 with B_2 free against the iteration. Dashed line: best value. 90
53 Method 2: B_2 (free) against the iteration. Dashed line: best value. 90
54 Sway, Method 1: B_1 with $B_2 = 0$ against the iteration for the worst run of each case. One line per starting point. Dashed line: best value. 92
55 Yaw, Method 1: B_1 with $B_2 = 0$ against the iteration for the worst run of each case. One line per starting point. Dashed line: best value. 93
56 Added mass A_{22} (left) and potential damping B_{22} (right) in sway against the angular frequency for mesh levels 1 to 6, for the smallest gap (G = 34 mm, h = 172 mm). 96
57 Added inertia A_{66} (left) and potential damping B_{66} (right) in yaw against the angular frequency for mesh levels 5 and 6, for the smallest gap (G = 34 mm, h = 172 mm). The shaded band marks the frequency range of the case. 97
58 Measured sway decay and Method 1 fit, h = 172 mm (cases 1 to 4). Thin lines: individual runs. Thick lines: case average. Box: RMSE of the fit (mean ± sd over the runs) and number of runs. 98
59 Measured sway decay and Method 1 fit, h = 194 mm (cases 5 to 8). Thin lines: individual runs. Thick lines: case average. Box: RMSE of the fit (mean ± sd over the runs) and number of runs. Case 6 (grey) is excluded from the results. 99
60 Measured sway decay and Method 1 fit, h = 222 mm (cases 9 to 12). Thin lines: individual runs. Thick lines: case average. Box: RMSE of the fit (mean ± sd over the runs) and number of runs. 100
61 Measured yaw decay and Method 1 fit, h = 172 mm (cases 1 to 4). Thin lines: individual runs. Thick lines: case average. Box: RMSE of the fit (mean ± sd over the runs) and number of runs. 101
62 Measured yaw decay and Method 1 fit, h = 194 mm (cases 5 to 8). Thin lines: individual runs. Thick lines: case average. Box: RMSE of the fit (mean ± sd over the runs) and number of runs. 102
63 Measured yaw decay and Method 1 fit, h = 222 mm (cases 9 to 12). Thin lines: individual runs. Thick lines: case average. Box: RMSE of the fit (mean ± sd over the runs) and number of runs. 103

List of Tables

1 Representative draft and close proximity ranges by ship type. 4
2 Dimensions of the testing facilities available within the Mechanical Engineering faculty at TU Delft. 19
3 Principal particulars of the reference container ship, full scale and model scale. 20
4 Test matrix at full scale and model scale ($\lambda = 87$). Each case was tested in both sway and yaw. 21
5 As-built properties of the model after ballasting. 23
6 As-built model scale mooring stiffness, from the four calibrated springs at their installed lever arm x and attachment height z, against the Froude-scaled target of Equation (42). . 26
7 Summary of the instrumentation used to track the model and release it at the start of each moored decay test. 30
8 Mean duration of the first two half-cycles, $T_{1/2,1}$ and $T_{1/2,2}$, over the runs of each case, for sway and yaw. The number of runs of the case is n and SD is the standard deviation over these runs. All durations are in seconds. 38
9 Sway: B_2 [N s^2/m^2] and B_1 [N s/m] with B_2 free, and B_1 [N s/m] with $B_2 = 0$, for every run of the cases with a positive B_2, in Method 1 and Method 2. ΔRMSE [mm] is the increase of the RMSE when B_2 is set to zero. 41
10 Added mass and potential damping from DIFFRAC at model scale, as the mean over the frequency range of each case. 46
11 Added mass per half-cycle: Method 1, Method 2 and DIFFRAC (case means). 48
12 Added inertia per half-cycle: Method 1, Method 2 and DIFFRAC (case means). 49
13 Repeat runs in which Method 2's change from half-cycle 1 to half-cycle 2 changes sign. . 50
14 Total damping B_1, cost J and RMSE of the fits of Method 1 (M1) and Method 2 (M2), as means over the repeat runs of each case. 51
15 Viscous damping per case (Method 1), obtained from the total damping of Table 14 by subtracting the potential and the pulley damping. sd: standard deviation of the total damping between repeat runs. 53
16 Normalized added mass of the first half-cycle and normalized viscous damping per case. 54
17 Full scale mooring stiffness for eight candidate line configurations. 78
18 OptiTrack calibration result summary. 81
19 Panasonic HG-C1100 specifications (manufacturer datasheet). 81
20 Micro-Epsilon optoNCDT ILD1420-25 factory settings (manufacturer datasheet). 82
21 ITS-MS 2015 electromagnet specifications (manufacturer datasheet). 82
22 Laser calibration points. 83
23 Parameters of the release detection and the zero centering. 84
24 Runs discarded during the processing of the moored decay records. 84
25 Cutoff frequency of the yaw filter. 85
26 Number of starting points that converge in each run: the final B_1 (and B_2 when it is free) is within 1 % of that of the best starting point. 87

27 Number of starting points that converge in each case with $B_2 = 0$ in Method 1. Runs: number of runs of the case. 91
28 Quay position and damping lid dimensions at model scale. The lid is 2.70 m long, and its center lies at 1.35 m along the model. 95
29 Mesh levels of the box shaped hull, with the number of panels along the length n_L, across the half beam n_{Bh} and over the draft n_T, and the number of panels of the damping lid along its length and across its width. 96
30 Principal particulars of the reference cruise ship, full scale and model scale ($\lambda = 75.2$). Full scale data from PIANC MarCom WG 235 [3]. 104
31 Full scale mooring stiffness of the candidate configurations. Option 18 was selected. . . 105
32 Planned test matrix of the cruise ship at full scale and model scale ($\lambda = 75.2$). These cases were prepared but not tested. 106

Nomenclature

Abbreviations

CFD	Computational Fluid Dynamics
CoG	Center of Gravity
DMA	Dynamic Mooring Analysis
DOF	Degree(s) of Freedom
FPSO	Floating Production, Storage and Offloading unit
GBS	Gravity Based Structure
HMSF	High Modulus Synthetic Fiber
ITTC	International Towing Tank Conference
LCG	Longitudinal Center of Gravity
LNG	Liquefied Natural Gas
MARIN	Maritime Research Institute Netherlands
MBL	Minimum Breaking Load
OCIMF	Oil Companies International Marine Forum
PIANC	World Association for Waterborne Transport Infrastructure
PMM	Planar Motion Mechanism
PP	Polypropylene
RANS	Reynolds Averaged Navier Stokes
RAO	Response Amplitude Operator
RMSE	Root Mean Square Error
TCG	Transverse Center of Gravity
TEU	Twenty-foot Equivalent Unit
UKC	Under Keel Clearance
ULCV	Ultra Large Container Vessel
URANS	Unsteady Reynolds Averaged Navier Stokes
VCG	Vertical Center of Gravity

List of Symbols

A	Added mass (sway) or added moment of inertia (yaw)
A_{22}	Added mass in sway
A_{66}	Added moment of inertia in yaw
A_0, A_1	Intercept and slope of the added mass against the amplitude (Method 2)
$\mathbf{A}(\omega)$	Added mass matrix
$\mathbf{A}_\infty$	Added mass matrix at infinite frequency
a_{22}, a_{66}	Dimensionless added mass in sway and added moment of inertia in yaw
$a_{m,i}$	Amplitude of half-cycle i
B	Beam of the vessel

B^1_{kj}, B_1	Linear damping coefficient
B^2_{kj}, B_2	Quadratic damping coefficient
B^{total}_{kj}	Total damping ($B^{\text{viscous}} + B^{\text{potential}} + B^{\text{pulley}}$)
B^{viscous}_{kj}	Viscous damping
$B^{\text{potential}}_{kj}$	Potential (radiation) damping
B^{pulley}_{kj}	Damping of the springs and pulleys of the mooring
$\mathbf{B}(\omega)$	Radiation damping matrix
b_{22}, b_{66}	Dimensionless damping in sway and yaw
C	Mooring stiffness (sway or yaw)
$C_{\text{moor},22}$	Sway mooring stiffness
$C_{\text{moor},66}$	Yaw mooring stiffness
$\mathbf{C}$, $\mathbf{C}_{\text{moor}}$	Hydrostatic restoring matrix and mooring stiffness matrix
C_b	Block coefficient
C_F	Frictional resistance coefficient
f, f_c	Frequency and cutoff frequency of the filter
Fn	Froude number
G	Lateral gap between the vessel side and the quay wall
G/B	Ratio of the gap to the beam
g	Acceleration of gravity
h	Water depth
I_{xx}, I_{yy}, I_{zz}	Roll, pitch and yaw mass moment of inertia about the center of gravity
J	Cost function of the fit
$\mathbf{K}(t)$	Retardation function
k	Form factor
k_{xx}, k_{zz}	Roll and yaw radius of gyration
kj	Index of the degree of freedom, 22 for sway and 66 for yaw
L, L_{bp}	Length between perpendiculars
L_{oa}	Length overall
L_{arm}	Distance of the mooring stations from the center of the model
M	Mass of the model
M_{22}, M_{66}	Mass and yaw mass moment of inertia ($M_{66} = I_{zz}$)
n	Order of the filter
n_w	Window length of the release detection
Rn	Reynolds number
S	Wetted surface
T	Draft
T/h	Ratio of the draft to the water depth
$T_{1/2,i}$	Duration of half-cycle i (half period)
T_d	Damped period
t	Time
V, v	Speed and characteristic velocity
x	Displacement (sway or yaw)

y	Sway displacement

Greek Symbols

δ	Threshold of the release detection
ζ	Damping ratio
λ	Geometric scale factor
ν	Kinematic viscosity
$\boldsymbol{\xi}$	Motion vector
ρ	Density of water
∇	Displaced volume
ϕ	Velocity potential
ψ	Yaw angle
ω	Angular frequency
ω_n, ω_d	Undamped and damped natural angular frequency

1

Introduction

1.1 Evolution and Scaling of Global Shipping

As the primary engine of globalization, the maritime industry facilitates approximately 80% of international trade by volume and over 70% by value [4]. Economists view shipping as a ”derived demand”, meaning its growth is inextricably linked to the fluctuations of global production and consumer needs [5]. Beyond the movement of consumer goods, the industry is a critical component of the energy market, as tankers facilitate the global distribution of oil and liquefied natural gas (LNG), underpinning international energy security.

In recent decades, the pursuit of cost efficiency has propelled seaborne trade to record levels, reaching 12.7 billion tons in 2024 [4]. This growth is not merely defined by volume, the distances cargo must travel have increased significantly due to geopolitical disruptions and the resulting rerouting of major trade lanes. To adapt to these pressures and exploit economies of scale, the global merchant fleet has undergone a structural transformation, shifting toward increasingly larger vessel dimensions to maximize transport efficiency [4].

The systemic drive for capacity has fundamentally altered global fleet characteristics, most notably within the container and leisure markets. This transition has sparked an ”industrial revolution” in the container sector, evolving from modest carriers to Ultra Large Container Vessels (ULCVs) that now frequently reach and even exceed 24,000 TEU to minimize transport costs per unit through massive economies of scale [5–7]. Modern fleets increasingly rely on ULC vessels, which exceed 366 meters in length and possess significantly wider beams to maximize cargo volume within the constraints of updated canal dimensions [3]. A parallel trend defines the cruise industry, where an annual passenger growth rate has driven the construction of ”mega” cruise vessels exceeding 200,000 gross tons [8].

1.2 Infrastructural and Operational Constraints

Figure 1 illustrates the growth in the size of container and cruise ships. This growth has been accompanied by increased demands on terminal layout, nautical accessibility, and berth infrastructure [8]. The deployment of these vessels tightens physical and operational margins at the berth, because many existing facilities were designed for smaller ship classes and more moderate berthing and mooring requirements [6, 7].

A primary infrastructure constraint is nautical accessibility. Larger vessels require deeper approach channels and berth pockets to maintain under keel clearance during transit, maneuvering, and moored stay. Reported developments for terminals targeting Ultra Large Container Vessels can require berth depths on the order of 20 m, with case based discussions indicating requirements of approximately 22 m depending on local conditions [6, 7]. Beyond depth, vessel scale increases loads transferred to the quay through both berthing impacts and mooring actions, which drives the need for higher capacity bollards and robust fender systems [7, 8]. PIANC, the World Association for Waterborne Transport Infrastructure,

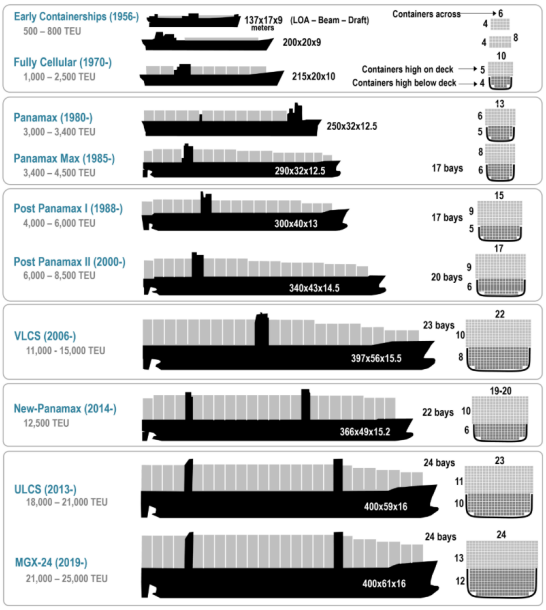

(a) Evolution of Container Ships [9]

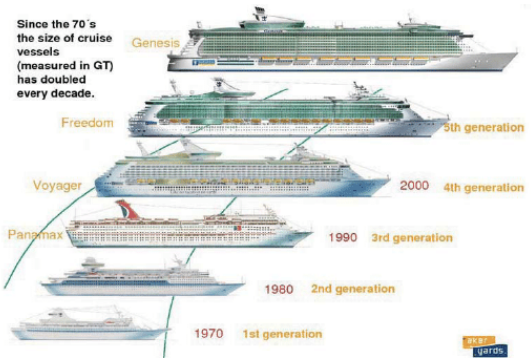

(b) Evolution of Cruise Ships [10]

Figure 1: Comparative evolution of maritime vessel designs.

emphasizes that the selection of berthing and mooring equipment should be based on site specific vessel characteristics and environmental conditions, rather than generic assumptions that may no longer be conservative for modern ship sizes [11].

These constraints translate directly into economic pressure at the terminal. Port competitiveness depends on berth availability, time efficiency, and the ability to sustain high cargo handling rates with minimal disruption [12]. High performing container terminals report ship to shore crane rates in the range of roughly 25 to 40 moves per hour, but such performance depends on the vessel remaining sufficiently stable and safely moored throughout cargo operations [7, 12]. Excessive motions or large transient line loads can trigger operational slowdowns, pauses, or additional safety measures, which reduces throughput and increases time at berth [7].

The consequences extend beyond productivity. From a safety and ethical perspective, mooring operations expose crews and terminal workers to hazards associated with high line tensions and potential line failure, including snap back events, which are explicitly addressed in industry guidance for safe mooring practice [13]. From an environmental perspective, reduced time efficiency at ports can increase system level emissions by extending port stays and propagating delay driven operating changes across the voyage [14]. Together, these economic, safety, and environmental drivers motivate the use of advanced analysis to evaluate moored vessel response and mooring loads under the constrained berth conditions associated with larger modern ships.

1.3 Project Collaboration

This research is conducted in collaboration with Haskoning, an international engineering consultancy with extensive expertise in maritime infrastructure. The study is embedded within the company's work on Dynamic Mooring Analysis (DMA), which is used to evaluate the safety and operability of vessels at berth. By integrating this thesis into Haskoning's professional environment, the research benefits

from real world project insights and industry standard workflows. Professional guidance and supervision within the company are provided by Dr. Alex van Deyzen, ensuring that the methodology and findings remain aligned with current engineering challenges in the maritime sector.

1.4 Problem Statement

Mooring assessments are used to quantify ship motions and the forces in mooring lines, bollards, and fenders under environmental loading, and to determine operational limits for safe cargo handling and safe stay at berth. In practice, a range of modeling levels is used, from static and quasi-static methods to fully dynamic time domain approaches, and the suitability of each depends on the local conditions and the external factors that must be represented [15].

For large modern vessels, the drivers of berth operability are often time varying, including gusting wind, long period excitation, and passing ship effects. PIANC guidance treats gusting wind and passing ships as dynamic load cases and discusses their inclusion within dynamic mooring assessment workflows [15]. From an operational perspective, surge and sway are repeatedly identified as critical motions because they directly constrain cargo handling and safe berth operations [16]. This creates a practical motivation for DMA in both industry studies and academic work that targets downtime and operability limits [17, 18].

A critical uncertainty within such dynamic simulations is the representation of energy dissipation in the coupled vessel-mooring system. In current DMA practice, viscous effects are often represented through simplified equivalent linear damping assumptions that are treated as fixed model inputs [18]. While this approach is attractive for engineering workflows, it becomes difficult to justify when the berth environment differs substantially from the conditions under which the damping values were derived. This concern is amplified in close proximity situations, where interaction effects can modify the flow field around the hull and alter the effective dissipation mechanisms [2].

In particular, when a vessel is moored with low under keel clearance and a narrow lateral gap to a quay wall, confinement can intensify local velocities and promote separation and turbulence. De Boer and Buchner (2005) show that viscous damping behavior can change in close proximity conditions compared with more open configurations, which challenges the transfer of generic damping values into berth specific simulations [2]. Consequently, if damping is prescribed using generalized assumptions, predictions of vessel motions and associated mooring loads can become biased, especially when operability limits under long period excitation must be resolved [18].

1.5 Defining Close Proximity

In this thesis, **close proximity** describes berth conditions where the vessel is constrained by nearby boundaries in two directions. As illustrated in Figure 2, the lateral proximity is defined by the gap G between the vessel side and the quay wall. This gap is primarily set by the fender system, since the fender size and its working compression determine the stand off distance during berthing and mooring operations [11]. The vertical proximity is defined by the under keel clearance UKC, the vertical distance between the vessel keel and the seabed at the berth, as shown in Figure 2b.

Recommended clearances for berth design and operability checks can be taken from PIANC guidelines, and the ranges relevant to this thesis are summarized in Table 1 [3, 6, 8, 11].

Only intermediate and large capacity vessels were considered for the classification presented in

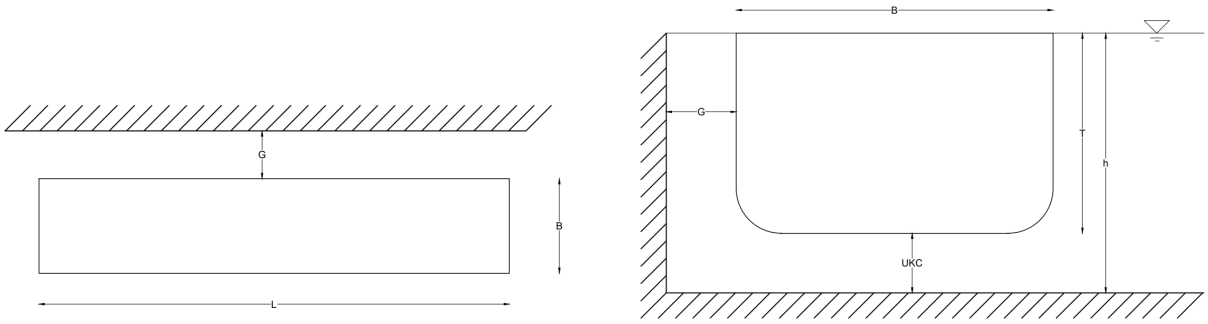

(a) Top View (b) Cross Section

Figure 2: Schematic illustration of the close proximity problem: (a) plan view showing the lateral gap G, and (b) cross section view showing both the lateral gap G and the under keel clearance UKC. Only the submerged part of the hull is drawn in (b).

Table 1: Representative draft and close proximity ranges by ship type [3, 6, 8, 11].

Type	**Draft T (m)**	**Fender size G (m)**	**Minimum UKC (m)**
Containership	7.5 - 17	2 - 3	$0.1T$ - $0.3T$
Cruise ship	4 - 9.3	1 - 3	2.0

Table 1. The specific under keel clearances and lateral gaps investigated experimentally in this thesis are given in Chapter 4.

1.6 Research Objective and Questions

The main objective of this thesis is to investigate how the viscous damping of a container ship moored in close proximity to a quay wall changes with lateral and vertical confinement. A secondary objective is to determine how significant this viscous damping is in the context of Dynamic Mooring Analysis. The following sub-objectives have been defined to work toward these two objectives:

1. How does the added mass change with lateral and vertical confinement?
2. How does the viscous damping change with lateral and vertical confinement?
3. How accurately can added mass and viscous damping be extracted from moored decay model tests?
4. How does the magnitude of the identified viscous damping compare to the damping typically assumed in current Dynamic Mooring Analysis practice?
5. Do the results of De Boer and Buchner align with the results of this study?

1.7 Methodological Approach

To answer the research questions above, this thesis follows a combined experimental and numerical approach. A box-shaped model representing a container ship is tested at the TU Delft flume tank under moored decay conditions in still water, across a matrix of under keel clearances and lateral gaps to a quay wall, together with a laterally unconfined reference case. Before testing, the model's mooring springs and mass properties are calibrated to determine the as-built configuration. Once the mooring line properties are established, the full identification pipeline, wet test, pulley identification, and DIFFRAC

computation, is carried out separately for the sway and yaw degrees of freedom. The resulting decay signals are used to identify the total system damping through an equation of motion fitting procedure. Potential damping is separately computed using DIFFRAC, and the contribution of the spring pulley mooring system is isolated through a dedicated dry test. Subtracting these two components from the total measured damping yields an estimate of the viscous damping associated with each confinement condition and each degree of freedom, treated throughout with explicit attention to the identifiability limits of the fitting procedure. Figure 3 summarizes this pipeline.

1.8 Thesis Outline

- Chapter 2: **Literature Review** presents a condensed synthesis of the state of the art, referencing the full literature review for further depth.
- Chapter 3:**Theory** introduces the theoretical framework: the equations of motion for a moored vessel, the total damping decomposition, potential flow theory, and the scaling laws relevant to a model scale campaign.
- Chapter 4:**Experiment** describes the model, mooring system, instrumentation, and test matrix used at the TU Delft flume tank.
- Chapter 5:**Data Processing and Viscous Damping Extraction** details how viscous damping is extracted from the measured decay signals, including the treatment of identifiability limits, and how the potential and pulley damping components are obtained.
- Chapter 6: **Results** presents the resulting damping and added mass decomposition across the test matrix.
- Chapter 7: **Discussion** interprets these results against the literature and discusses the limitations of the approach.
- Chapter 8: **Conclusions and Future Work** answers the research questions above and outlines recommendations for future work.

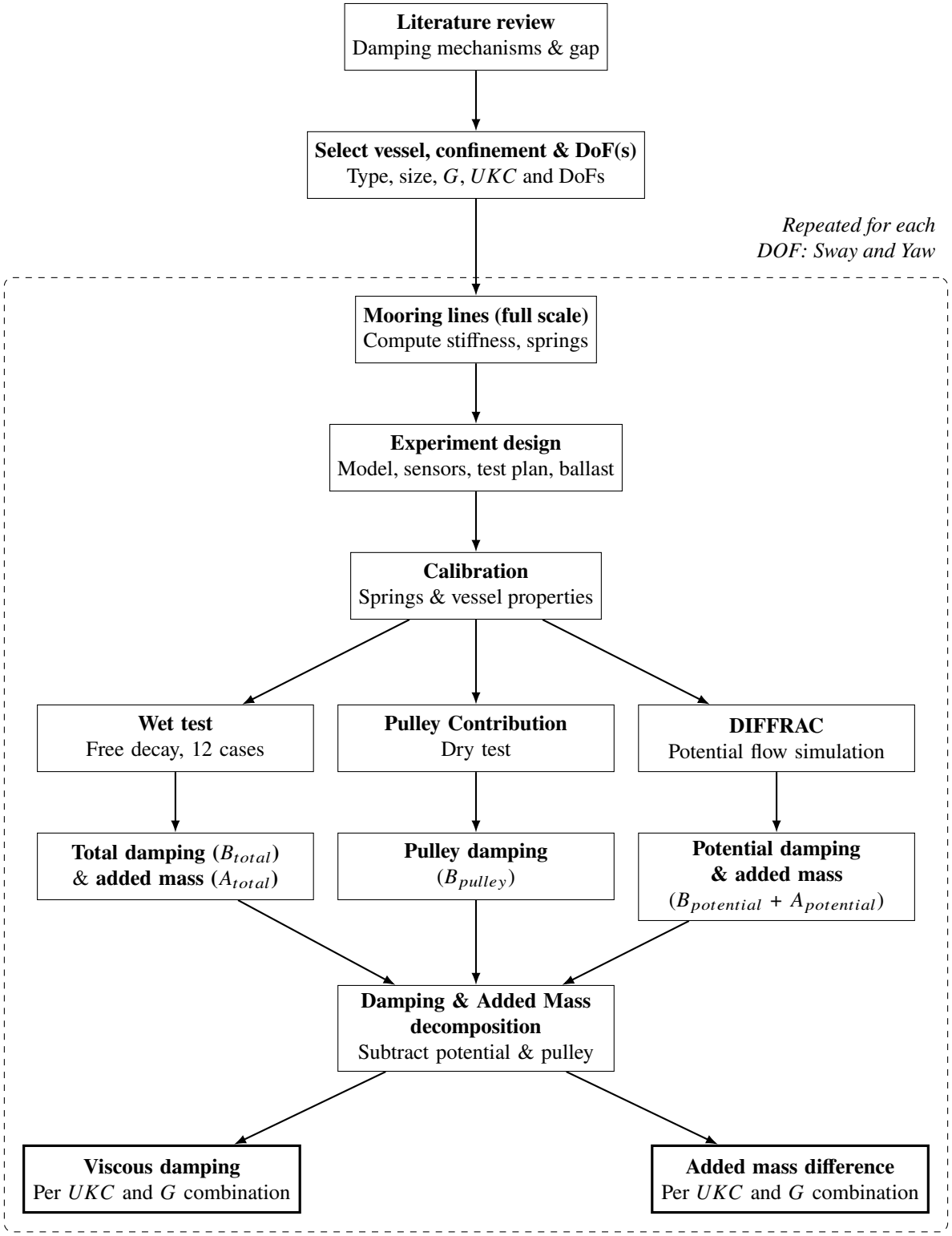

Figure 3: Overview of the research methodology.

2

Literature Review

This chapter reviews the state of the art on the viscous damping of moored vessels, focusing on how the specific problem addressed in this thesis came to be identified. It follows the field from its origins in offshore engineering, through shallow water and combined lateral and vertical confinement, and discusses CFD as an alternative method and why it is not used here. The chapter closes with the research gap that motivates the experimental campaign.

2.1 Origins in Offshore Engineering

Interest in the viscous damping of moored vessels first emerged within the offshore industry, in the context of vessels moored in open water using highly compliant single point mooring systems. Because these systems have very low natural frequencies, they are highly susceptible to resonance driven by second order, slowly varying wave drift forces, and the foundational framework for computing these forces was established by Newman (1974), Faltinsen and Michelsen (1975), and Pinkster (1979) [19–21]. Standard wave radiation damping is negligibly small at these low frequencies, so predicting the actual motion limits required finding the missing damping elsewhere. Wichers and van Sluijs, and later Wichers and Huijsmans, showed that this missing damping actually comes from two distinct sources: viscous damping, and a separate potential damping mechanism they termed wave drift damping, corresponding to the velocity dependent part of the mean wave drift force [22, 23].

Wave drift damping for surge can now be calculated with reasonable reliability, following Hermans' (1999) addition of low forward speed effects to three dimensional potential diffraction theory [24]. A key finding of Wichers' expanded three degree of freedom model, however, was that although wave drift damping is critical for surge, its mean value for the transverse motions of sway and yaw is small enough to ignore [25]. Viscous damping is therefore the dominant limiting factor for these transverse motions. For surge, vessels moored to quay walls also tend to use stiffer mooring arrangements, which shift the natural frequency away from resonant surge and make wave drift damping less of a concern in that context too. Both points leave the viscous damping of the transverse motions as the focus of this thesis.

This finding motivated Wichers to investigate viscous damping directly, which his 1988 PhD thesis did extensively through physical model testing [25]. For surge, standard motion decay tests were run in still water. For the transverse motions, forced oscillation Planar Motion Mechanism (PMM) tests were used instead, chosen over moored decay specifically to decouple sway and yaw, which are heavily coupled through the single point mooring system that lets the vessel weathervane freely [25]. Since viscous drag is spread unevenly along the hull, a combined moored decay test would create complex cross coupled effects that forced PMM testing avoids, letting Wichers isolate the local viscous resistance coefficients along the hull directly [25]. This thesis uses moored decay tests instead. Its barge model is fully symmetric and restrained by linear springs at the bow and stern, which minimizes the cross coupling between sway and yaw that made forced oscillation necessary in Wichers' case.

2.2 Shallow Water Confinement

Moving from open to shallow water changes the picture again. Zhou et al. (2005) and Drobyshevski (2004) both showed that proximity to the seabed squeezes the fluid beneath the hull, sharply increasing added mass as under keel clearance decreases [26, 27]. Because this also lengthens natural periods, it indirectly raises the importance of viscous damping at these lower frequencies, yet both studies remain within potential flow and say nothing about the viscous contribution itself. A smaller set of studies has attempted to capture that contribution directly: Xiong et al. (2015) used moored decay model tests to recover a viscous damping ratio for a moored barge in shallow water, and Tezdogan and Incecik (2016) applied unsteady RANS simulations to vertical ship motions in shallow water, both finding viscous effects that potential theory alone does not predict [28, 29]. Both studies, however, considered vessels in open shallow water without any solid lateral boundary, so the combined effect of shallow water and lateral confinement remains largely unaddressed.

2.3 Combined Lateral and Vertical Confinement

Adding a solid quay wall on top of shallow water introduces gap resonance: the trapped water column resonates at natural modes, most critically the piston mode, whose modes and natural frequencies were identified for rectangular moonpools by Molin [30] and later used to interpret the response in narrow gaps. Because potential theory carries no damping, these resonances are numerically unstable. Several remedies have been proposed that address this numerically: Huijsmans et al. [31] suppress it with a rigid lid, Newman [32] add a linear damping term, Chen [33] propose a dissipative boundary condition, and van der Molen [34] let a small fraction of fluid transmit through the quay wall to drain energy from the gap. Gap resonance sits outside this thesis's scope and is mentioned only because it pushed the field toward experimentally derived viscous damping instead.

That shift is best traced through a progressive body of work by Buchner and co-authors. In 2001, Buchner et al. studied an LNG carrier moored side by side with an FPSO and showed that open water viscous formulations could not capture the vortex shedding driven by water oscillating in the narrow gap between them. Their fix was pragmatic: run decay tests on the moored vessel and on an isolated reference vessel, and treat the difference in damping as the viscous contribution specific to the interaction [35]. In 2004, Buchner et al. formalized this into a repeatable method for an LNG carrier moored alongside a gravity based structure: run a time domain simulation using only diffraction based mass and retardation data, with no viscous damping included, then use a numerical optimization to find the linear and quadratic damping coefficients that best match the measured decay trace [36]. This turned viscous identification from a subtraction between two tests into a fitting problem against a single decay record, conceptually the same approach this thesis follows.

De Boer and Buchner then took this fitting method and applied it systematically, in a study this thesis leans on directly. They ran calm water decay tests for an LNG carrier moored alongside a GBS at two water depths (15 m and 25 m, giving T/h of 0.73 and 0.44) and four lateral gaps (3 m, 6 m, 9 m and an unconfined reference, giving G/B of 0.068, 0.136 and 0.204), reusing the 2004 penalty function optimization to isolate viscous damping at each combination [2]. The results are the clearest evidence available that vertical and lateral confinement behave differently. Vertical confinement acted as a consistent driver, with damping increasing as water depth decreased across every motion tested. The lateral gap produced no single trend: surge damping rose slightly as the gap narrowed, sway damping

fell, and roll and yaw showed no consistent pattern at all. Natural periods behaved more coherently than damping itself, lengthening as both depth and gap decreased. De Boer and Buchner concluded that confinement alters a vessel's restoring, inertial and dissipative properties simultaneously, which is why generic damping values cannot be transferred between berths without geometry specific data.

The study nevertheless has two limitations that matter for how its damping values can be used. The first concerns scaling. The tests were carried out at a scale of 1:50, and the measured decay traces were converted to full scale values and then used directly in the full scale time domain and diffraction analyses [2]. Froude scaling preserves gravity driven phenomena, but it leaves the Reynolds number at model scale several orders of magnitude below that of the full scale vessel. Viscous forces, which depend on boundary layer development and flow separation, therefore do not scale with Froude's law, and viscous damping is typically overestimated at model scale [37, 38]. Because no viscous scale correction was applied, the damping coefficients extracted at full scale inherit this discrepancy. The tests of this thesis are also performed at model scale under Froude similarity, so this effect is not unique to the earlier work and is treated as a limitation of the present results as well.

The second limitation concerns the test configuration. The LNG carrier was moored alongside a gravity based structure of finite length in an offshore setting, rather than against a continuous quay wall [2]. Water can therefore flow around the ends of the structure, which changes the flow in the gap, and the gaps and water depths that were tested differ from those at a container terminal. De Boer and Buchner therefore demonstrate convincingly that viscous damping must be determined for the specific confinement geometry, but their individual coefficients cannot be transferred directly to a quayside berth.

2.4 Computational Fluid Dynamics

Computational Fluid Dynamics (CFD) offers a numerical alternative to physical testing. Most methods solve the Reynolds Averaged Navier Stokes (RANS) equations, or their unsteady form (URANS) for the time dependent, low frequency motions relevant here [39]. Because the viscosity of the fluid is part of the governing equations, CFD resolves the viscous forces directly [39], and a virtual decay test can be analyzed with the same procedure as a physical one [40]. It can also be run at full scale, which avoids the conflict between Froude and Reynolds scaling that affects model tests [41, 42]. For open water vessels, URANS has been shown to predict equivalent damping with reasonable accuracy. Pistidda et al. (2012) matched model tests for the sway and yaw of a float over barge, Jaouën et al. (2019) obtained estimates within 5% of experiments for an LNG carrier, and the Reproducible Offshore CFD Joint Industry Project of Koop et al. (2022) showed that independent practitioners following a common modeling practice agree within about 20% of each other and of the experiments [43–45]. These studies also report a persistent weakness in surge, where damping was underestimated by about 30% in one case and deviated strongly in the benchmark, because standard turbulence models struggle with friction dominated flows [43, 45].

For confined geometries, Jiang et al. (2024) used a two dimensional RANS solver for side by side cylinders in waves and reproduced the frictional shear, the vortices shed at the corners and the wake in the gap directly, so that no calibrated damping lid was needed [46]. Most CFD studies of gap flow, however, concern offshore side by side configurations of two floating bodies, which differ from a stationary vessel against a solid quay wall, and the computational cost remains prohibitive for the long duration, fully coupled time domain simulations of moored vessels.

This thesis does not use CFD as its primary method, for four reasons. First, the benchmarks above

all concern vessels in unhindered open water, so the accepted margin of error cannot be assumed to hold in a narrow gap with a small under keel clearance [44, 45]. Second, turbulence models are simplified submodels of complex phenomena such as separation and vortex shedding [39], which are exactly the mechanisms that dominate damping under confinement. Their uncertainty is already significant in open water, as the surge deviations above show, and it is reasonable to expect it to grow where the flow is squeezed and accelerated. Third, resolving the flow with high accuracy requires very fine grids [39], and the thin gap and under keel passages of a berth, combined with the long simulated durations needed for low frequency decay tests, make the cost high. Fourth, and most importantly, CFD cannot serve as a standalone predictive tool and must be validated against experimental data [39], while no such data exists for the extreme confinement levels targeted here (Section 2.5). Physical model testing is therefore used to establish the experimental reference, and CFD is recommended as future work to be validated against the results of this thesis.

2.5 Research Gap

Figure 4 maps the reviewed studies by their lateral and vertical confinement. The majority of these studies consider a vessel without a lateral boundary, shown in the band on the right of the figure. They cover nearly the full range of water depths, but at the highest values of T/h they are predominantly potential flow or mathematical studies, which do not address the viscous damping (Section 2.2). Studies that include a lateral boundary, either a quay wall or a second fixed or floating structure, are considerably fewer, and none of them extends beyond a T/h of 0.73.

This absence of data coincides with the conditions under which large container ships are moored in practice. A minimum under keel clearance of $0.1T$ to $0.3T$ (Table 1) corresponds to T/h between 0.77 and 0.91, and a fender gap of 2 to 3 m to G/B below 0.1. The closest existing study, that of De Boer and Buchner, reaches this range in terms of the gap, but its smallest under keel clearance corresponds to a T/h of 0.73, and its results are subject to the limitations discussed in Section 2.3. CFD cannot yet fill this gap either, since no experimental data exist in this range against which it could be validated (Section 2.4). Experimental data on the viscous damping of a vessel moored close to a quay wall at a small under keel clearance are therefore lacking, and this thesis aims to provide them through physical model tests.

The confinement levels investigated in this thesis are shown by the star markers in Figure 4. Within the limits imposed by the dimensions of the flume tank (Section 4.1), they were chosen to overlap with the range of De Boer and Buchner, so that the trends of the two studies can be compared, while the two smallest under keel clearances, with T/h of 0.80 and 0.90, extend into the range relevant for large container ships. The original scope also included a cruise ship, which, like a large container ship, is particularly sensitive to wind loading because of its large above water profile. Its planned test cases are shown by the diamond markers. The preparation for these tests was completed (Appendix D), but the tests themselves could not be carried out within the time available in the flume tank.

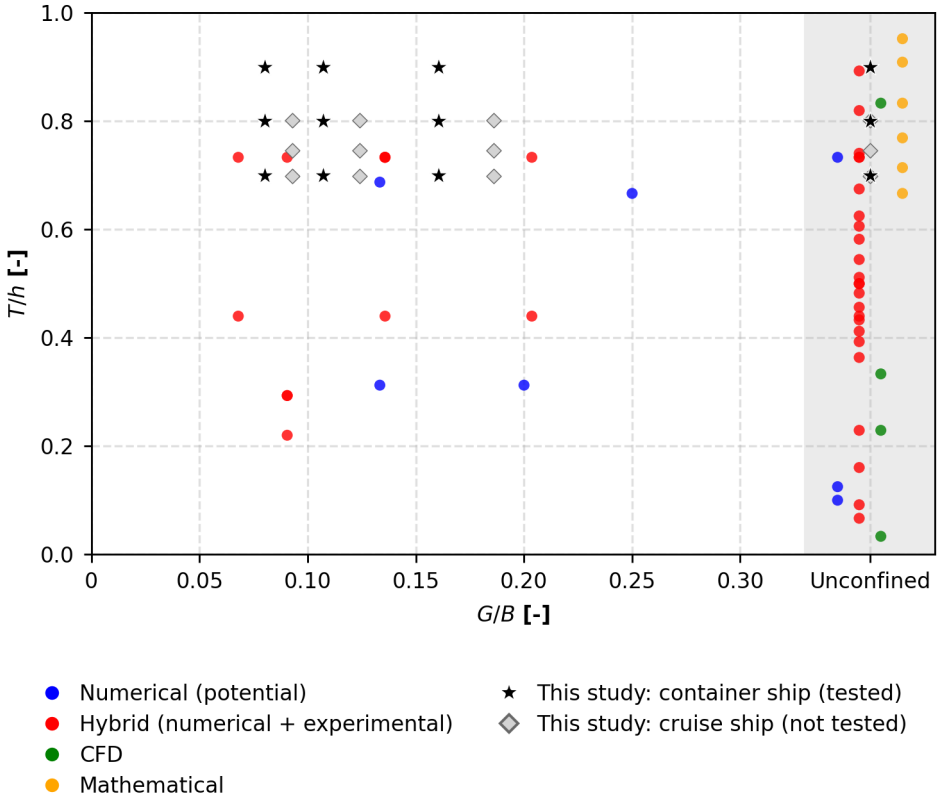

Figure 4: Reviewed literature and this thesis by confinement level. Gray band: cases without a lateral boundary or with G/B above 0.3.

3

Theory

Vessel motions are described in a body fixed coordinate system with origin at the vessel's center of gravity, in the six degrees of freedom shown in Figure 5: surge (x), sway (y), heave (z), roll (ϕ), pitch (θ), and yaw (ψ) [38]. As established in Section 4.1, this thesis investigates sway and yaw.

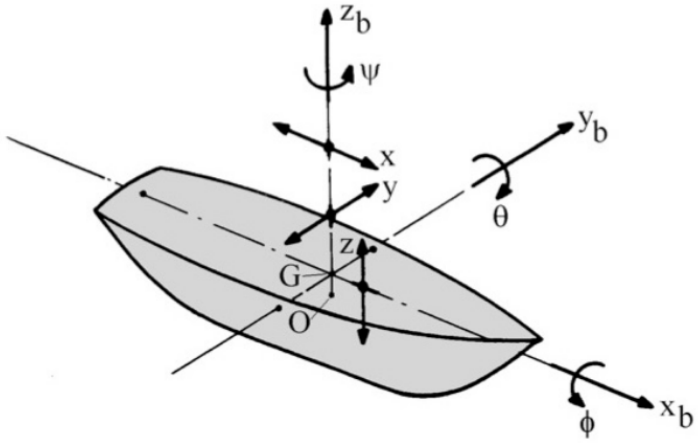

Figure 5: Definition of the body fixed coordinate system and the six degrees of freedom: surge (x), sway (y), heave (z), roll (ϕ), pitch (θ), and yaw (ψ). [47]

3.1 Potential Flow Theory

3.1.1 Frequency Domain

In classical linear potential theory, the fluid is modeled as incompressible, inviscid and irrotational. Under these assumptions the fluid velocity can be expressed as the gradient of a scalar velocity potential $\phi(\mathbf{x}, t)$, and mass conservation yields Laplace's equation in the fluid domain Ω [37, 48]:

$$\nabla^2 \phi = 0 \qquad \text{in } \Omega. \tag{1}$$

On the body surface S_B, impermeability implies that the normal fluid velocity equals the normal velocity of the body boundary,

$$\frac{\partial \phi}{\partial n} = \mathbf{v}_B \cdot \mathbf{n} \qquad \text{on } S_B, \tag{2}$$

where $\mathbf{n}$ is the outward normal and $\mathbf{v}_B$ is the body surface velocity.

At the free surface $z = 0$, the kinematic and dynamic boundary conditions can be linearized about the mean water level. Combining the linearized kinematic and dynamic conditions leads to the standard linear free surface condition for harmonic motion at angular frequency ω [37, 48]:

$$\frac{\partial \phi}{\partial z} - \frac{\omega^2}{g} \phi = 0 \qquad \text{on } z = 0, \tag{3}$$

together with appropriate seabed and radiation conditions (e.g., no-flux at a flat bottom and an outgoing-wave condition at infinity).

Decomposition of the potential.
For small amplitude waves, the total potential is commonly decomposed into an incident wave potential and scattered components. This decomposition assumes the vessel undergoes harmonic oscillations in six degrees of freedom (DOF), as defined in the body fixed coordinate system shown in Figure 5. Following standard potential flow formulations, the total potential ϕ is expressed as:

$$\phi = \phi_I + \phi_D + \sum_{j=1}^{6} \xi_j \phi_{Rj}, \tag{4}$$

where ϕ_I is the incident wave potential, ϕ_D is the diffraction potential for a fixed body, and ϕ_{Rj} are radiation potentials associated with unit oscillatory motion in degree of freedom j and ξ_j denotes the complex motion amplitude in DOF j [38, 48].

Let $\boldsymbol{\xi}(\omega)$ be the complex 6-DOF motion vector. The linearized equation of motion for a moored vessel in regular waves is typically written as [38, 48]:

$$\Big[-\omega^2 \big(\mathbf{M} + \mathbf{A}(\omega)\big) + i\omega\, \mathbf{B}(\omega) + \big(\mathbf{C} + \mathbf{C}_{\text{moor}}\big) \Big] \boldsymbol{\xi}(\omega) = \mathbf{F}_{\text{exc}}(\omega). \tag{5}$$

Here, $\mathbf{M}$ is the rigid body mass/inertia matrix, $\mathbf{A}(\omega)$ and $\mathbf{B}(\omega)$ are the added mass and radiation damping matrices, $\mathbf{C}$ is the hydrostatic restoring matrix and $\mathbf{C}_{\text{moor}}$ represents the linearized mooring stiffness about the equilibrium position. The right hand side $\mathbf{F}_{\text{exc}}(\omega)$ is the external force vector. Solving (5) over a range of ω yields response amplitude operators (RAOs) for wave frequency motions.

3.1.2 Time Domain: Cummins Equation

The frequency domain result only describes the vessel's response to purely harmonic motion. Cummins extended it to arbitrary time domain motion by recognizing that a body moving through a free surface leaves behind a wave field that continues to act on it after the motion that generated it has stopped, a memory effect the frequency domain formulation cannot represent [49]. The resulting time domain equation of motion is

$$\big(\mathbf{M} + \mathbf{A}_\infty\big)\, \ddot{\boldsymbol{\xi}}(t) + \int_0^t \mathbf{K}(t-\tau)\, \dot{\boldsymbol{\xi}}(\tau)\, d\tau + \big(\mathbf{C} + \mathbf{C}_{\text{moor}}\big) \boldsymbol{\xi}(t) = \mathbf{F}_{\text{exc}}(t). \tag{6}$$

where $\mathbf{A}_\infty$ is the added mass at infinite frequency and $\mathbf{K}(t-\tau)$ is the retardation function, recovered from the frequency domain potential damping through

$$\mathbf{K}(t) = \frac{2}{\pi} \int_0^\infty \mathbf{B}(\omega) \cos(\omega t)\, d\omega. \tag{7}$$

3.2 Equations of Motion for a Moored Vessel

A moored decay test oscillates at, or very close to, the vessel's own natural frequency. The frequency dependent hydrodynamic coefficients of Equation (5) therefore only need to be evaluated once, at that

single frequency, and the convolution integral of Equation (6) collapses to a constant coefficient equation. The symmetry of the box shaped model (Section 4.3) also decouples sway and yaw from each other and from the remaining degrees of freedom, so each decay test is described by its own single degree of freedom equation. For sway,

$$(M_{22} + A_{22})\,\ddot{y}(t) + B^1_{22}\,\dot{y}(t) + B^2_{22}\,\dot{y}(t)\,|\dot{y}(t)| + C_{\text{moor},22}\,y(t) = 0 \tag{8}$$

and for yaw,

$$(M_{66} + A_{66})\,\ddot{\psi}(t) + B^1_{66}\,\dot{\psi}(t) + B^2_{66}\,\dot{\psi}(t)\,\left|\dot{\psi}(t)\right| + C_{\text{moor},66}\,\psi(t) = 0 \tag{9}$$

where $y(t)$ is the sway displacement and $\psi(t)$ is the yaw angle, M_{22} is the vessel mass and $M_{66} = I_{zz}$ its yaw mass moment of inertia about the vertical axis through the center of gravity, A_{22} and A_{66} are the added mass and added moment of inertia evaluated at the identified natural frequency, B^1_{22}, B^1_{66} are the linear and B^2_{22}, B^2_{66} the quadratic total damping coefficients, and $C_{\text{moor},22}$, $C_{\text{moor},66}$ are the mooring stiffness in sway and yaw. The hydrostatic restoring matrix $\mathbf{C}$ of Equation (5) contributes nothing to either equation, since a floating vessel has no hydrostatic stiffness in sway or yaw, so all restoring in the moored decay tests of this thesis comes from the mooring springs alone. Each damping term B^1_{kj} and B^2_{kj} is decomposed further in Section 3.3.

The undamped natural frequency and linear damping ratio follow from the linear part of each equation alone,

$$\omega_{n,kj} = \sqrt{\frac{C_{\text{moor},kj}}{M_{kj} + A_{kj}}}, \qquad \zeta_{kj} = \frac{B^1_{kj}}{2(M_{kj} + A_{kj})\,\omega_{n,kj}} \tag{10}$$

with $kj = 22$ for sway and $kj = 66$ for yaw, giving a damped natural frequency $\omega_{d,kj} = \omega_{n,kj}\sqrt{1-\zeta^2_{kj}}$ and damped period $T_{d,kj} = 2\pi/\omega_{d,kj}$. These expressions come from the classical linear damped oscillator and hold exactly only when $B^2_{kj} = 0$. With the quadratic term present, $\omega_{n,kj}$ and ζ_{kj} describe the linear skeleton of the system rather than its complete behavior, and the period actually measured from a decay trace is amplitude dependent, decreasing as the oscillation decays rather than staying fixed at $T_{d,kj}$, and approaching it only in the small amplitude limit where the contribution of B^2_{kj} becomes negligible next to B^1_{kj}.

Because $\omega_{n,kj}$ depends on A_{kj}, which is itself only known once the oscillation frequency has been identified, the frequency used to query A_{kj} (Section 3.1) is read directly from the measured decay trace rather than solved for iteratively, avoiding this circularity.

3.3 Damping Decomposition

The linear and quadratic damping coefficients identified from each decay trace through Equations (8) and (9) are not themselves single physical mechanisms. The linear coefficient splits into three separate contributions and the quadratic coefficient into two,

$$B^1_{kj} = B^1_{\text{potential},kj} + B^1_{\text{viscous},kj} + B^1_{\text{pulley},kj}, \qquad B^2_{kj} = B^2_{\text{viscous},kj} + B^2_{\text{pulley},kj} \tag{11}$$

with $kj = 22$ for sway and $kj = 66$ for yaw.

3.3.1 Potential Damping

The wave radiation damping predicted by linear potential flow theory (Section 3.1), denoted $B^1_{\text{potential},kj}$, is the only damping mechanism that theory contains, and for this reason it enters only the linear coefficient B^1_{kj} and never the quadratic coefficient B^2_{kj}. It is obtained numerically from the diffraction software DIFFRAC [1], evaluated over the frequency range of the measured decay, so that it is consistent with the frequency at which Equations (8) and (9) are fitted.

3.3.2 Viscous Damping

The damping generated by the hull itself, denoted $B_{\text{viscous},kj}$, is the quantity of interest in this thesis. It comprises two mechanisms not captured by potential flow theory, skin friction and eddy making, illustrated in Figure 6. Skin friction arises from viscous shear stresses acting on the submerged hull and is typically categorized as a linear effect. It is present across all degrees of freedom, but is particularly relevant for low frequency surge motions [37]. Eddy making, in contrast, results from flow separation and the resulting pressure loss at sharp hull corners, bilge keels, and other geometric discontinuities. This mechanism is the dominant source of dissipation for roll, sway and yaw [37], the motions investigated in this thesis.

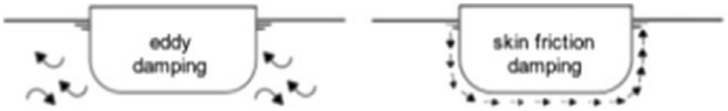

Figure 6: Illustration of the viscous effects acting on a vessel, highlighting the distinction between eddy making and skin friction components.

Both mechanisms contribute to $B^1_{\text{viscous},kj}$ and $B^2_{\text{viscous},kj}$, already carried through Equations (8) and (9).

Both mechanisms are also affected by confinement. When the vessel sways or yaws, it displaces water that has to flow around the hull. In open water this water can move freely, but near the seabed and a quay wall it is forced through the narrow passage under the keel and through the gap between the hull and the wall. The smaller this passage, the higher the velocity of the flow through it. A larger amount of water is then set in motion with the vessel, which increases the added mass [26], and the higher velocities along the hull and around the bilges increase the skin friction and the flow separation, which increases the viscous damping [2].

3.3.3 Pulley Damping

The third contribution, $B^1_{\text{pulley},kj}$ and $B^2_{\text{pulley},kj}$, is specific to this experimental setup rather than a mechanism found in the general mooring literature. The four mooring springs were installed vertically and redirected into the horizontal plane using pulleys, so the horizontal restoring force measured at the vessel also carries damping generated inside these pulleys. Left uncorrected, this damping would be misattributed to the vessel's own viscous damping.

These coefficients were identified independently, through dry decay tests of the spring and pulley assembly alone, isolated from the vessel (Section 5.2), and enter Equation (11) in the same linear and

[1] DIFFRAC, MARIN, `https://www.marin.nl/en/about/facilities-and-tools/software/diffrac`.

quadratic form as the potential and viscous contributions. They are subtracted from the fitted B^1_{kj} and B^2_{kj} of Equations (8) and (9), together with $B^1_{\text{potential},kj}$, to isolate $B^1_{\text{viscous},kj}$ and $B^2_{\text{viscous},kj}$.

3.4 Scaling Laws

Reproducing the vessel's behavior at model scale requires dynamic similarity, the ratio of forces acting on the model matching those acting on the full scale vessel [38]. Two dimensionless numbers govern this. The Froude number,

$$Fn = \frac{v}{\sqrt{gL}} \tag{12}$$

is the ratio of inertial to gravitational forces, with v a characteristic velocity and L a characteristic length, and governs gravity driven phenomena such as wave making, radiation damping and natural periods [38]. The Reynolds number,

$$Rn = \frac{vL}{\nu} \tag{13}$$

is the ratio of inertial to viscous forces, with ν the kinematic viscosity of the fluid, and governs the development of the boundary layer and the points of flow separation, the physical sources of viscous damping [37, 38].

Matching both numbers at model scale is not possible with the same fluid, since Fn requires velocity to scale with $\sqrt{L}$ while Rn requires velocity to scale with $1/L$ [38]. The model tests in this thesis prioritize Froude scaling, so that the natural periods and radiation damping governing the moored decay tests are correctly reproduced [38]. The cost is a model scale Reynolds number several orders of magnitude below full scale, so the boundary layer around the model is thicker, and can be laminar or transitional, where the full scale boundary layer is thin and fully turbulent [37].

Because $B^1_{\text{potential},kj}$ (Section 3.3) is a gravity driven, inviscid quantity, it scales correctly between model and full scale under Froude's law [38]. $B^1_{\text{viscous},kj}$ and $B^2_{\text{viscous},kj}$ do not, since they depend on the Reynolds number through the boundary layer and the flow separation, and the viscous damping is therefore expected to be overestimated at model scale [37, 38].

3.4.1 Correction for Viscous Scale Effects

In ship resistance tests, a similar scale effect on the resistance is corrected with the method that originates from William Froude [38]. The total resistance is divided into a frictional part, which depends on the Reynolds number, and a residual part, which depends on the Froude number. The frictional part is estimated from the friction of a flat plate with the same length and wetted surface as the hull. For this purpose, the ITTC adopted the ITTC-1957 model-ship correlation line [50],

$$C_F = \frac{0.075}{\left(\log_{10} Rn - 2\right)^2}, \tag{14}$$

where C_F is the frictional resistance coefficient, the frictional resistance made dimensionless with $\frac{1}{2}\rho S V^2$, with S the wetted surface and V the speed. This line is based on the friction of a flat plate, but already contains a small correction for the three dimensional form of the hull [50]. The frictional resistance coefficient of the model, calculated with Equation (14) at the Reynolds number of the model, is subtracted

from the measured total resistance coefficient. The remaining coefficient is taken to be the same for the model and the ship at the same Froude number, and the frictional resistance coefficient at the Reynolds number of the ship is added again, together with a correlation allowance based on full scale experience [38, 50].

In the current ITTC procedure, the viscous pressure resistance caused by the shape of the hull is included through a form factor k, which assumes it to be proportional to the friction, so that the viscous part of the resistance becomes $(1 + k)\, C_F$ [50]. The ITTC formulates this decomposition for flows without separation [50]. In the original method of Froude, this form resistance was instead assumed to be independent of the Reynolds number and was scaled with the residual part [38]. Both versions were developed for a model towed at a constant speed through open, deep water.

4

Experiment

4.1 Design Choices

The design of the experiment follows from the motions under investigation. These determine the geometry of the model and the test method, which in turn define the requirements for the test facility, the model scale and the test cases. Each of these choices is discussed below.

4.1.1 Degrees of Freedom

The degrees of freedom investigated in this thesis were selected on the basis of the dominant damping mechanisms and their practical relevance for moored vessels. At the low natural frequencies of a moored vessel, the wave radiation damping is negligible, and the remaining damping originates from wave drift damping and viscous effects (Section 2.1). Wave drift damping is significant in surge, but small in the transverse motions of sway and yaw, for which viscous damping is therefore the dominant contribution [25]. These transverse motions are also of direct practical relevance. Sway is among the motions identified as critical for cargo handling and safe berth operations [16], and the large lateral windage area of modern container and cruise vessels makes gusting wind an important dynamic load in this direction [15]. Moreover, the viscous damping of sway and yaw is governed mainly by eddy making at the bilges and hull corners [37], which is the mechanism intensified by confinement (Section 3.3). Sway and yaw were therefore selected as the degrees of freedom of this thesis.

Roll and surge were not considered. Roll damping is particularly sensitive to the hull form, through the bilge geometry and appendages [38], which a generic model cannot represent. Surge could not be included within the time available for the experimental campaign.

4.1.2 Model Geometry and Test Method

To determine the viscous damping of sway and yaw separately, and as a function of well defined confinement parameters, the experiment was designed as an uncoupled benchmark problem. For this reason, the vessel was represented by a rectangular box rather than by a scaled hull form. The box is symmetric about its midship section, which decouples sway from yaw during the decay tests, whereas the asymmetric distribution of the viscous forces along a real hull would couple the two motions. Its even keel and straight sides give a uniform draft and a uniform distance to the quay wall, so that the under keel clearance and the lateral gap are each defined by a single value. Describing the confinement by these two hull independent parameters also facilitates the application of the results in dynamic mooring analyses, where viscous damping coefficients are assigned per vessel class and confinement condition rather than derived for a specific hull form [18]. In addition, a box is straightforward to manufacture and to ballast, so that a single model can represent the draft and mass of different vessel types through its internal ballast alone. The disadvantage of this choice is that the sharp edges of the box, present along its whole length, promote flow separation. The consequences of this are discussed in Chapter 7.

Moored decay tests were adopted as the test method. Wichers applied forced oscillation tests with a Planar Motion Mechanism (PMM) to decouple sway and yaw, which were coupled through the weathervaning of his single point mooring (Section 2.1). In this thesis, the vessel is restrained by linear springs at the bow and the stern, which prevent weathervaning, and the symmetry of the model further limits the coupling between the two motions. Moored decay tests are therefore sufficient to identify the damping of each degree of freedom directly, following the identification approach of De Boer and Buchner (Section 2.3).

4.1.3 Facility Selection

Three test facilities were available within the Faculty of Mechanical Engineering at TU Delft: two towing tanks and the Wave Flume Tank. Their principal dimensions are compared in Table 2.

Table 2: Dimensions of the testing facilities available within the Mechanical Engineering faculty at TU Delft.

Characteristic	Towing Tank 1	Towing Tank 2	Wave Flume Tank
Length (m)	142	85	7
Width (m)	4.22	2.75	2.3
Water depth (m)	2.50	1.25	0.4

The Wave Flume Tank was selected, since it directly provides the shallow and confined water required for the tests. Its water depth of about 0.4 m allows small under keel clearances to be reached without draining a large tank, and its limited size provides easy access to the model and the setup, which had to be adjusted for every change of gap and water depth. In addition, the flume was available within the testing period of the project, whereas both towing tanks were reserved until later in the year. The larger width of the towing tanks would have reduced the reflection of waves from the side walls, but this did not outweigh the advantages of the flume. The facility and its adaptations are described in Section 4.2.

4.1.4 Scale and Test Cases

The model scale was determined by a wooden box that was already available in the laboratory. Its beam of 0.43 m was retained, and its length was extended to 2.70 m, so that its length to beam ratio of 6.3 corresponds to that of existing vessels. Since the original scope comprised both a container ship and a cruise ship (Section 2.5), vessels of both types with this ratio were selected, allowing the same box to represent both at different scales. With the beam fixed, the geometric scale follows from the beam of the full scale vessel, so that a larger vessel results in a smaller model scale. Representing a ULCV with a beam of 48.2 m would have required a scale of about 1:112. At this scale, a full scale gap of 3 m reduces to 27 mm and an under keel clearance of 1.5 m to 13 mm, which leaves little margin with respect to the initial displacement required for the decay tests. A large model scale is moreover preferable for the identification of viscous damping, since a larger model reduces the difference in Reynolds number with the full scale vessel (Section 3.4). A smaller container ship was therefore selected instead of the ULCV class originally targeted.

The selected container ship has a length overall of 249 m, a length between perpendiculars of 235 m and a beam of 37.4 m, taken from the representative design vessel data compiled by PIANC [3], which

gives a geometric scale of $\lambda = 87$. The full scale draft of 13.5 m was matched through internal ballasting, resulting in a model draft of 155 mm. Table 3 lists the particulars at full scale and model scale. Since the model is a rectangular box rather than a scaled hull form, its block coefficient and displacement differ from those of the full scale vessel. The preparation for the cruise ship, at a scale of $\lambda = 75.2$, is documented in Appendix D.

Table 3: Principal particulars of the reference container ship, full scale and model scale ($\lambda = 87$). Full scale data from PIANC MarCom WG 235 [3].

Parameter	Symbol	Unit	Scaling	Full Scale	Model Scale
Length overall	L_{oa}	m	λ	249	2.862
Length between perpendiculars	L_{bp}	m	λ	235	2.70
Beam	B	m	λ	37.4	0.430
Draft	T	m	λ	13.5	0.155
Depth	D	m	λ	22.1	0.254
Air draft	–	m	λ	54	0.621
Block coefficient	C_b	–	–*	0.63	1.00
Displacement	Δ	t	–*	74750.4	179.8 kg
Yaw radius of gyration	k_{zz}	m	λ	58.75	0.675
Roll radius of gyration	k_{xx}	m	λ	13.84	0.159

*As a rectangular box, the model has $C_b = 1.00$ by construction, so its displacement follows directly from $\Delta = \rho\, L_{bp}\, B\, T$ rather than from λ^3 scaling of the full scale value.

The lateral gaps were selected starting from the smallest realistic fender gap for container vessels recommended by PIANC, 2 m (Table 1). At the adopted scale, this gap reduces to 23 mm. A moored decay test requires an initial displacement of at least approximately 10 mm to be applied reliably, and since the gap changes as the vessel moves, a displacement of this magnitude would substantially alter a 23 mm gap during the decay rather than leaving it effectively constant. The 2 m gap was therefore excluded, and full scale gaps of 3, 4 and 6 m were tested instead, corresponding to G/B of 0.079, 0.107 and 0.160.

In addition to these berth cases, a baseline configuration was included, in which the model is centered in the flume width with a lateral gap of 905 mm. This configuration represents an effectively unconfined lateral condition, while retaining the vertical confinement of the corresponding water depth. The baseline was tested at every water depth, so that the influence of the lateral gap can be separated from that of the under keel clearance by comparing each berth case with the baseline at the same depth.

For the vertical confinement, three water depths were selected relative to the draft of 13.5 m: 19.3, 16.87 and 15 m, corresponding to T/h of 0.70, 0.80 and 0.90. The shallowest depth gives an under keel clearance of 1.5 m, at the lower end of the range for container ships (Table 1), while the deepest is close to the smallest under keel clearance of De Boer and Buchner, at a T/h of 0.73, so that the two studies can be compared. The resulting twelve test cases are listed in Table 4.

4.2 Test Facility

The experiments were conducted in the Wave Flume Tank of the Maritime and Transport Technology laboratory at TU Delft. The flume is 7.0 m long and 2.3 m wide, with a typical water depth of 0.4 m and a maximum flow speed of 0.4 m/s. It is equipped with a vertical plunging wedge wavemaker driven by

Table 4: Test matrix at full scale and model scale ($\lambda = 87$). Each case was tested in both sway and yaw.

		Full scale			Model scale				
Case	Condition	UKC (m)	G (m)	h (m)	UKC (mm)	G (mm)	h (mm)	T/h	G/B
1	Laterally unconfined	1.5	–	15.0	17	905	172	0.90	–
2	Near quay	1.5	6	15.0	17	69	172	0.90	0.160
3	Near quay	1.5	4	15.0	17	46	172	0.90	0.107
4	Near quay	1.5	3	15.0	17	34	172	0.90	0.079
5	Laterally unconfined	3.4	–	16.87	39	905	194	0.80	–
6	Near quay	3.4	6	16.87	39	69	194	0.80	0.160
7	Near quay	3.4	4	16.87	39	46	194	0.80	0.107
8	Near quay	3.4	3	16.87	39	34	194	0.80	0.079
9	Laterally unconfined	5.8	–	19.3	67	905	222	0.70	–
10	Near quay	5.8	6	19.3	67	69	222	0.70	0.160
11	Near quay	5.8	4	19.3	67	46	222	0.70	0.107
12	Near quay	5.8	3	19.3	67	34	222	0.70	0.079

an electric motor, which can generate regular and irregular waves with wavelengths between 0.20 and 1.00 m. Since this thesis relies exclusively on moored decay tests in still water, the wavemaker was not used. All tests were conducted in fresh water with a density of 999 kg/m^3.

The side walls of the flume are not perfectly straight and do not fully meet the tank floor, leaving a gap of approximately 1 cm at the bottom. A dedicated wooden wall was therefore installed along one side of the flume to represent the quay wall. The wall is 5.015 m long, and a thin foam gasket tape was fitted along its bottom edge to seal the joint with the tank floor. Figure 7 shows the flume before and after its installation.



(a) Without the wooden quay wall.



(b) With the wooden quay wall installed.

Figure 7: The Wave Flume Tank before and after the installation of the wooden quay wall.

The flume has a number of known imperfections, which were accounted for rather than corrected. The bottom of the tank is not perfectly level, which results in an estimated uncertainty of approximately 0.5 cm in the nominal water depth, and a weld seam near the middle of the flume forms a small bump on

the bottom. In addition, a thin layer of algae covers the bottom. Its removal was not possible within the available time, and it is assumed to have no measurable influence on the results. Photographs of these imperfections are given in Appendix A.

4.3 Model Vessel

4.3.1 Construction

The model was made by extending the existing plywood box (Section 4.1) to the principal dimensions of Table 3, using a different grade of marine plywood. One of the end walls of the box is not perfectly perpendicular to the centerline, but the resulting angular error is smaller than 1° and is considered negligible. A backbone was mounted along the centerline of the deck to provide fixed attachment points for the mooring lines. Its length sets the moment arm through which the mooring springs generate the yaw stiffness, and it was sized to help reach the target mooring stiffness derived in Section 4.4.

The construction and the ballasting were planned with a Rhino[2] model of the hull and the backbone (Figure 8), from which the mass and the mass moments of inertia were calculated using the density of each material. The lead blocks available in the laboratory were added to this model, to verify that the target mass, center of gravity and I_{zz} of Table 3 could be reached with the available ballast.

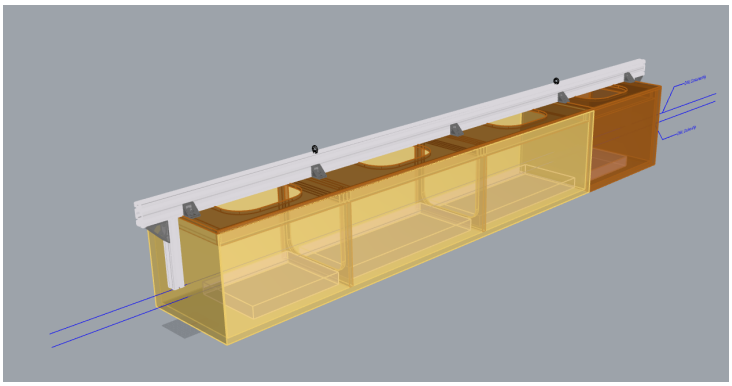

Figure 8: Rhino model of the box shaped vessel, showing the internal compartments and the backbone with mooring attachment points, used to calculate the target mass properties.

4.3.2 Dry Testing

Before ballasting, the Rhino calculation of the empty hull was verified by measurement. The empty model weighed 51.38 kg. Since the extension was made of a different material than the original box, its longitudinal center of gravity did not coincide with the geometric midpoint of the hull, and it was therefore measured rather than assumed. The yaw mass moment of inertia I_{zz} was measured with a swing test (Figure 9). Two temporary hooks were mounted on the centerline, symmetrically about the measured center of gravity, and the model was suspended from the crane beam by two steel cables of equal length and given a small angular displacement about the vertical axis. The period of the resulting torsional oscillation was determined from the duration of 50 oscillations, and I_{zz} was derived from this period. The test was carried out on the empty model, since at the target mass of approximately 180 kg the hooks and cables could have failed.

[2]Rhinoceros 3D, Robert McNeel & Associates, `https://www.rhino3d.com/`.



Figure 9: The unballasted model prepared for the dry test, showing the plywood extension and the temporary suspension hooks mounted symmetrically about the measured center of gravity.

The measured mass and I_{zz} differed from the Rhino calculation by 0.16 kg and 5.41×10^5 kg mm^2, respectively.

4.3.3 Ballasting

Table 5 gives the as-built properties of the model after ballasting. Since the mass and center of gravity of the box follow from its own geometry (Section 4.1), the comparison with the reference vessel is made through the radii of gyration, $k = \sqrt{I/m}$. The yaw radius of gyration of the model amounts to 0.247 L_{bp}, against 0.250 L_{bp} for the reference vessel, and the roll radius of gyration to 0.371 B, against 0.370 B. The inertia of the model therefore corresponds closely to that of the reference vessel in both degrees of freedom.

Table 5: As-built properties of the model after ballasting.

Parameter	Symbol	As built
Mass	m	178.73 kg
Longitudinal center of gravity	LCG	1301.4 mm
Transverse center of gravity	TCG	0 mm
Vertical center of gravity	VCG	133.7 mm
Roll inertia about CoG	I_{xx}	4.56 kg m^2
Pitch inertia about CoG	I_{yy}	79.76 kg m^2
Yaw inertia about CoG	I_{zz}	79.75 kg m^2

To verify the draft, the required waterline was marked on the hull before ballasting and compared with the actual waterline after the ballasted model was floated. Figure 11 shows that the two lines coincide along the hull. The comparison also revealed a slight bending of the hull under the weight of the ballast, with the middle of the model lying slightly deeper than its ends.



Figure 10: Lead ballast blocks positioned inside the hull, labeled with their individual masses.

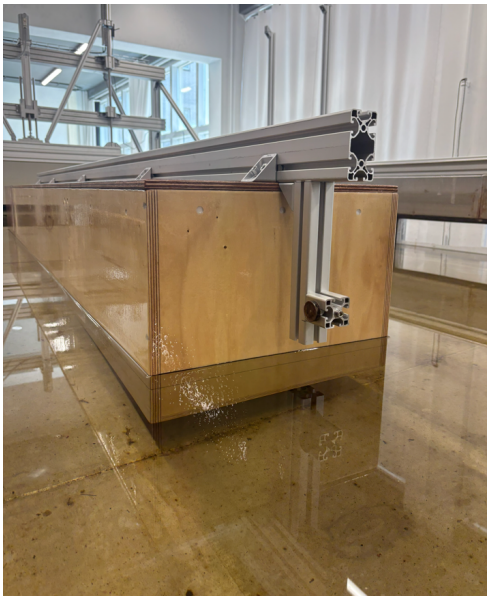

Figure 11: The marked required waterline aligning with the actual waterline after ballasting.

4.4 Mooring System

A decay test identifies the damping at the natural frequency of the system, which is set by the mass of the vessel and the stiffness of its mooring. The choice of mooring stiffness therefore directly determines the conditions under which the damping is identified. Since this thesis aims at damping coefficients that can be applied to vessels moored at a berth, the stiffness was derived from the mooring arrangement of a real container ship at a quay.

As discussed in Section 3.2, a floating vessel has no hydrostatic restoring force in sway or yaw, so the entire restoring force in the decay tests is provided by the mooring. The mooring system therefore had to reproduce, at model scale, a sway and yaw stiffness representative of a container ship moored at a quay wall.

4.4.1 Target Stiffness

The target stiffness was derived from the mooring arrangement of an existing container ship rather than chosen arbitrarily. The Polar Mexico, a 3,800 TEU post-Panamax container ship (L_{oa} = 230 m, L_{bp} = 220.8 m, B = 37.3 m), was selected from Significant Ships of 2017 [51]. Its beam is close to that of the reference vessel of Table 3 (37.4 m), although it is considerably shorter. Its general arrangement drawing, scaled to the length and beam of the reference vessel, was used to route the mooring lines from the ten winches of the vessel to the bollards along the quay (Figure 41 in Appendix A.4). The quay was also equipped with Trelleborg cone fenders with a height of 2 m, which do not enter the stiffness calculation.

Eight combinations of line material, minimum breaking load (MBL) and pretension were compared with an in-house mooring stiffness tool of Haskoning, using line data from OCIMF MEG4 [13]. The full comparison and the projection of the line stiffness are given in Appendix A.4. A polyester/polypropylene line with an MBL of 750 kN, pretensioned to 5 % of the MBL, was selected as representative. This gives a full scale stiffness of $C^{\text{full}}_{\text{moor},22}$ = 588 kN/m in sway and $C^{\text{full}}_{\text{moor},66}$ = 8800 MN m/rad in yaw. Scaled to model scale (λ = 87, with the scaling laws given in Appendix A.4), the target stiffness becomes

$$C^{\text{target}}_{\text{moor},22} = 77.7 \text{ N/m}, \qquad C^{\text{target}}_{\text{moor},66} = 153.6 \text{ N m/rad}. \tag{15}$$

4.4.2 Spring and Pulley Arrangement

The restoring force had to act horizontally, in the plane of the sway and yaw motion, on the attachment points of the backbone (Section 4.3). Attaching the springs at the height of the center of gravity of the vessel was considered first, since this would not introduce a roll moment at release. This height, however, lies below the waterline and was therefore not accessible. The attachment height was instead set at 244 mm above the keel, close to the deck level of the reference vessel (Table 3). A horizontal spring between the backbone and a fixed point would not have fit in the small gap between the vessel and the quay wall, which is itself one of the parameters varied in the tests (Section 4.1). Each spring was therefore mounted vertically and pretensioned at installation, with its lower end connected to a string that runs over a pulley. The pulley redirects the line of action over 90°, from vertical to horizontal, before the string reaches the backbone (Figure 12). Since the pulley sheave carries only the string tension, which equals the spring tension, and not the weight of the spring, the model or any other part of the setup, the

redirection does not couple the vertical suspension into the horizontal restoring force. It does, however, introduce a small amount of friction damping at each sheave. This pulley damping therefore had to be identified separately and subtracted from the total damping (Section 3.3).

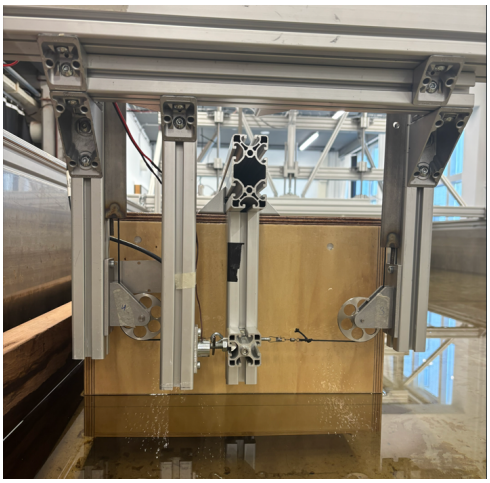

Figure 12: Pulleys at one mooring station, mounted on the aluminum frame above the flume. Each redirects the string from its spring (mounted further up the frame, not visible here) into a horizontal line of action toward the backbone.

The target sway stiffness was 77.7 N/m. The setup had to be built from springs that were already available in the laboratory, and the four springs used gave a combined stiffness of 71.6 N/m. The same four springs also provide the yaw stiffness, with two springs mounted fore and two aft, each at a lever arm of $x = 1.41$ m from the LCG of the vessel. Table 6 compares the realized stiffness with the targets, and the calibration of the individual springs is described in Appendix A.4.5. It is this realized stiffness, not the full scale target, that determines the natural frequency of Equation (10) and that is used in the analysis of the decay tests.

Table 6: As-built model scale mooring stiffness, from the four calibrated springs at their installed lever arm x and attachment height z, against the Froude-scaled target of Equation (42).

Parameter	Symbol	Target	Realized	Attained
Attachment height above keel	z	–	244 mm	–
Lever arm from LCG	x	–	1.41 m	–
Sway stiffness	$C_{\mathrm{moor},22}$ (N/m)	77.7	71.6	92 %
Yaw stiffness	$C_{\mathrm{moor},66}$ (N m/rad)	153.6	142.35	93 %

4.5 Pulley Calibration

Ideally, the fully assembled mooring, with all four springs and pulleys attached to the model, would have been tested in air, to isolate the damping of the pulleys from the other contributions (Section 3.3). Given the weight of the model, this was not practical. Each spring and pulley set, fore and aft, was therefore tested separately outside the flume, with a lead block in place of the model.

A rectangular lead block with a mass of $m = 21.4$ kg was suspended from a crane by a rope and positioned between the two pulleys of one station, with a laser distance sensor recording its horizontal displacement (Figure 13).



Figure 13: Dry test of one spring and pulley set, isolated for moored decay testing.

The block was first tested as a simple pendulum, swinging on the crane rope with the springs and pulleys disconnected. This baseline test served two purposes. It verified the identification method, and it quantified the stiffness and damping of the rope and the block alone, so that this contribution could be subtracted later. Repeat measurements were taken for this baseline case.

The first set of springs and pulleys was then connected to the block, which was centered and released into moored decay from an initial horizontal displacement of approximately 20 mm, with the laser recording the oscillation. The same procedure was repeated for the second set. The damping of the pulleys follows from these decay tests after subtraction of the pendulum damping, as described in Section 5.2.

4.6 Experimental Design and Layout

Once the facility, the scale and the geometry of the model had been fixed, the experimental setup was designed to allow the tests to be performed in a practical and repeatable manner. It was built from 40×40 mm and 80×80 mm aluminum profiles and designed in full in AutoCAD[3] beforehand, taking into account the equipment available in the laboratory. Figures 14 and 15 present the design for Case 12. As mentioned before, given the limited width of the flume and the small lateral gaps, a horizontal spring arrangement was not feasible (Section 4.4). The springs were therefore suspended from vertical spring holders on the aluminum frame and redirected to the horizontal by the pulleys. The holders, the pulleys and the wooden quay wall are shown in the cross section of Figure 15, which also defines the water depth, the draft and the under keel clearance of this case.

The drawings represent the initial design and omit some features of the final setup. The two laser sensors, for example, are not included. In the final setup, both were placed on the starboard side of the vessel above the pulleys, mounted on a plate that extends toward the model to keep it within their measuring range (Figure 16). Three electromagnets were mounted on the aluminum frame, so that initial displacements could be imposed in both sway and yaw without modifying the setup between tests. In the drawings, these electromagnets act on three plates attached to the backbone. Preliminary trials with

[3] AutoCAD, Autodesk, `https://www.autodesk.com/products/autocad`.



Figure 14: Top view of the test layout for Case 12, showing the backbone with the electromagnet mounting brackets at each end and the wooden quay wall. All dimensions are in cm.

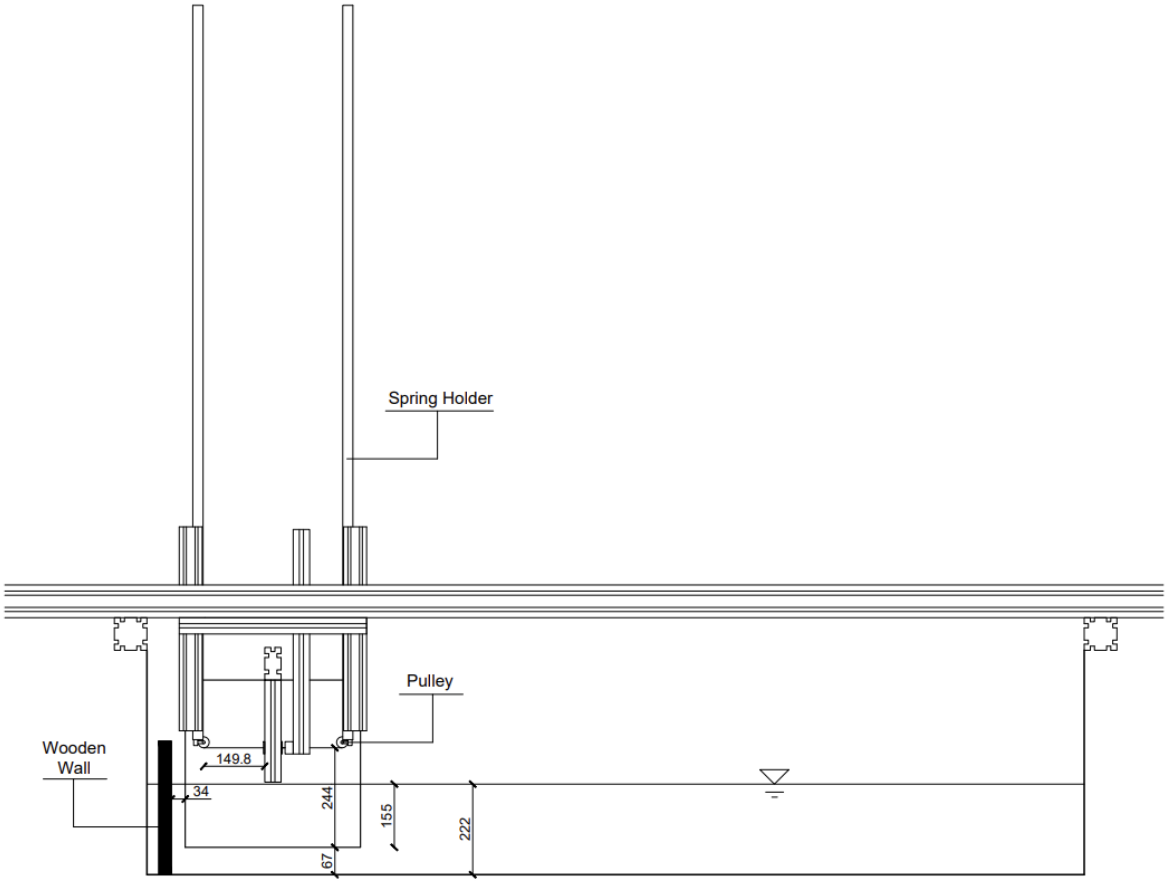

Figure 15: Side View of the test layout for Case 12, defining the water depth h, model draft T, and under keel clearance. All dimensions are in mm.

this arrangement revealed two limitations. First, one of the plates released the vessel later than the other, although the power to both electromagnets was cut simultaneously. Second, both ends of the model had to start from the same initial displacement within a millimeter, whereas the frame had to be repositioned for every change of the gap G, after which the plates could not be readjusted with sufficient accuracy. The plates were therefore replaced by bolts, which can be turned to set the displacement precisely while monitoring the live readings of the lasers (Figure 16b). Since only two bolts were available, one of them was relocated whenever the tests switched between sway and yaw.

The frame was designed to slide across the width of the flume on top of the 80×80 mm aluminum profiles, so that a single structure could be used for every lateral gap. For each case, an aluminum spacer was cut to the gap width at model scale (Figure 35). The zero position was first set against the wooden wall, after which the frame was moved away from the wall until the spacer fitted exactly in the gap, which fixed the frame at the intended gap (Figure 34).

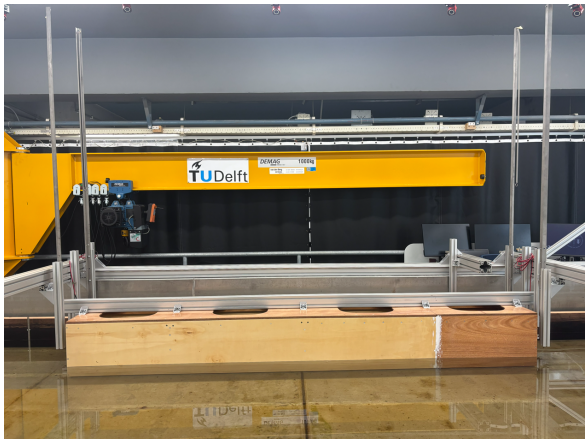

(a) Overview of the assembled setup in the flume, for a case with the model positioned close to the quay wall.



(b) Fore end of the setup as mounted on the model, with the spring, pulley, and electromagnet in place, for the baseline case with the model centered in the flume.

Figure 16: Photographs of the assembled test setup in the flume.

4.7 Instrumentation

The moored decay of the model was measured with a motion capture system and two laser distance sensors, and the model was released at the start of each test by electromagnets.

Global sway and yaw were measured with an OptiTrack[4] motion capture system, which tracks a set of markers on the deck of the model, placed where they are visible to most of the cameras. The motions are recorded at one of these markers, selected as the rigid body, which was placed at the center of the deck (Figure 45). The marker layout, the camera positions around the flume and the calibration results are given in Appendix A.5.

In addition, two laser distance sensors measured the sway of the backbone directly, one at each end of the model: a Panasonic HG-C1100 at the fore end and a Micro-Epsilon optoNCDT 1420-25 at the aft end. Each sensor measures the distance from a fixed point to the backbone, which gives an independent sway decay record at that end. Both sensors were calibrated beforehand to convert their output signal into a displacement in millimeters. The lasers recorded continuously during each test and served two

[4]OptiTrack, `https://docs.optitrack.com/v2.3/motive/rigid-body-tracking`

purposes. Before the release, their live readings were used to set the same initial displacement at both ends of the model, so that no coupling was introduced at the start of the decay. During the test, they provided an independent check of the motion recorded by OptiTrack.

The OptiTrack system and the two lasers were connected to the same data acquisition computer, which started logging all channels at the same instant and thus gave all instruments a common time base. OptiTrack sampled at 100 Hz and the lasers at 1,000 Hz.

Table 7 summarizes the main specifications of the instruments. The manufacturer datasheets and the calibration results are given in Appendix A.5.

Table 7: Summary of the instrumentation used to track the model and release it at the start of each moored decay test.

Instrument	Model	Measures	Range	Accuracy
Motion capture	OptiTrack	Global sway, yaw	–	0.244 mm
Laser, fore	Panasonic HG-C1100	Sway at backbone	35 mm	70 μm
Laser, aft	optoNCDT 1420	Sway at backbone	25 mm	–
Electromagnet (×3)	ITS-MS 2015	Release mechanism	20 N	–

4.8 Test Procedure

Before the measurement campaign, preliminary tests were carried out to verify that all components of the setup worked as intended. The campaign was organized to minimize the number of changes to the setup. Testing started at the smallest water depth and the smallest gap of 34 mm (Case 4), in sway. The procedure described below was followed for every case.

The model was first positioned at the gap of the case under test, by sliding the two frames, one at each end of the model, along the 80×80 mm profiles until the spacer cut to the required gap fitted exactly between a reference bracket and the sliding unit. The same spacer was used to verify the gap between the model and the wooden wall at both ends, after which the frames were locked in position.

After the waves caused by the repositioning had settled, a first measurement was taken with the model resting freely, which provided the reference resting position of the vessel in the laser signals. For the sway tests, only the two sway electromagnets were powered, and the third was disconnected. The model was moved toward the electromagnets until the bolts made contact with them, and was then held in place by the magnetic force. Using the resting position from the lasers as a reference, the bolts were adjusted until the initial displacement was equal at both ends and had the intended value, so that no coupling was introduced at release.

The water was then left to settle again. A zero measurement of 10 s was recorded with the model held at its initial displacement, to check whether waves were still acting on the vessel. If oscillations caused by remaining waves were still visible in the signals, the waiting time was extended and the zero measurement repeated. Otherwise, a measurement of at least 60 s was started, and the model was released by cutting the power to the electromagnets with a push button. To avoid disturbing the water surface, the people around the flume remained still during the measurements.

After each run, the model was reattached to the electromagnets and the procedure was repeated, since at least three runs were required for every case. The laser signals were checked after each run, and whenever the resting position of the vessel had shifted, an additional resting measurement was taken

before the next run. When a run showed anomalies, such as excessive noise or a large surge motion at the start of the decay, additional runs were performed to ensure the quality of the data.

Once at least three valid sway runs had been obtained, the same case was tested in yaw without moving the vessel. Only the connections were changed: the sway electromagnet at the fore end was disconnected and the yaw electromagnet connected, and the bolt was moved to the other side of the backbone extender to engage the yaw electromagnet. The yaw runs followed the same procedure as the sway runs.

After both degrees of freedom had been tested, the frames were moved to the next gap and the procedure was repeated. At the smallest water depth, the gaps were tested in the order 34, 46 and 69 mm, followed by the laterally unconfined case. Water was then added to the flume to reach the next depth. The depth was set with a stainless steel ruler bolted to the wooden wall, which provided a fixed measuring position, since the bottom of the flume is not level (Section 4.2) and the depth therefore varies along its length. Once the target depth had been reached, the water was left to settle before testing resumed. At the second depth, the order was reversed, starting with the laterally unconfined case and moving toward the wall through the 69, 46 and 34 mm gaps. At the third depth, testing again started at the 34 mm gap and moved toward the middle of the flume. Alternating the direction in this way avoided moving the frames back to their starting position at every new depth.

4.9 Raw Data

Figure 17 shows the signals as recorded for one sway run and one yaw run of Case 2 ($h = 172$ mm, $G = 69$ mm), runs 178 and 169, respectively. The two upper panels of each plot show the fore and aft laser signals, and the remaining panels the six degrees of freedom measured by OptiTrack at the center of the deck. The first part of each record shows the model held at its initial displacement, before the electromagnets are switched off.

In the sway run (Figure 17a), both lasers follow the same trend, as expected for a pure translation. The constant offset between their levels results from the two different sensor types. Besides the sway motion, a small surge response of the order of 1 mm is present. Its amplitude is small enough for its contribution to the restoring force to be neglected, and its frequency is higher than that of the sway motion, so that it can be removed by filtering. Shortly after the release, a roll oscillation with a maximum of about 0.2° is visible. It also appears in the sway and laser signals, but it again lies at a higher frequency than the sway motion and can be filtered out. This roll was expected, since the mooring lines and the electromagnets are attached above the vertical center of gravity of the model, so that the release introduces a small moment about the longitudinal axis. Heave and pitch remain very small. The release also triggers a small yaw response. It could not be removed completely despite repeated attempts, but its amplitude remains below 0.03°, and it is therefore neglected.

In the yaw run (Figure 17b), the fore and aft laser signals are mirrored, which is consistent with a rotation about the center of the model. A small surge response is again present. In contrast to the sway tests, its frequency is close to that of the yaw motion in all cases, so that it cannot be separated by filtering. Given its small amplitude, it is neglected. The sway response remains below 1 mm, and heave, pitch and roll also remain small, so they are not considered further.

These raw signals are not used directly for the damping identification. Their processing is described in Chapter 5.

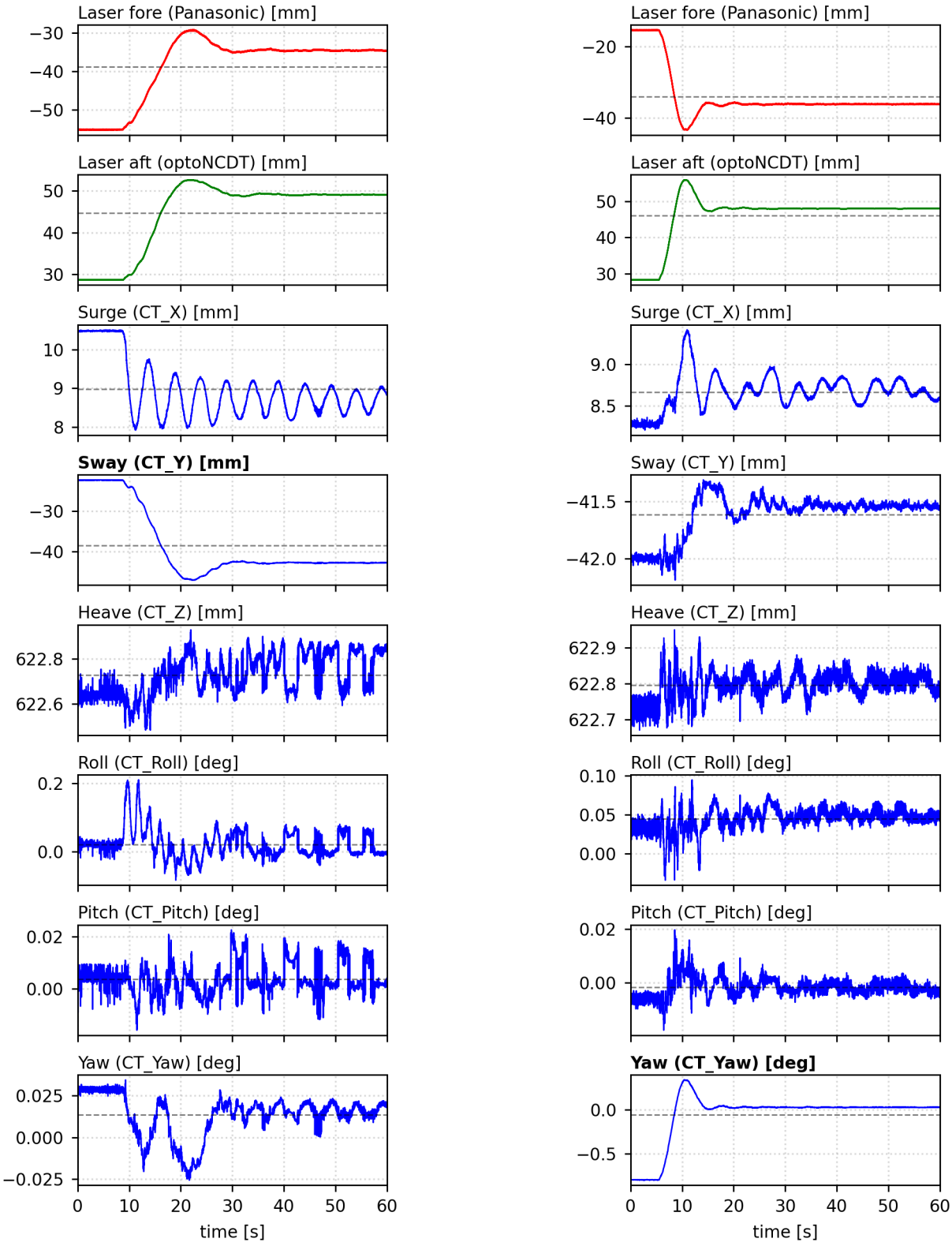

(a) Sway release (run 178).

(b) Yaw release (run 169).

Figure 17: Raw laser and OptiTrack signals for Case 2 ($h = 172$ mm, $G = 69$ mm). The two upper panels show the lasers and the remaining panels the OptiTrack signals at the center of the deck.

5

Data Processing and Viscous Damping Extraction

This chapter describes how the viscous damping of the moored vessel was extracted from the moored decay tests. A wet decay only gives the total damping of the moored model, which also contains the potential damping and the damping of the springs and pulleys (Section 3.3). The viscous damping therefore follows from

$$B_{kj}^{\text{viscous}} = B_{kj}^{\text{total}} - B_{kj}^{\text{potential}} - B_{kj}^{\text{pulley}}, \tag{16}$$

where B_{kj}^{viscous}, B_{kj}^{total}, $B_{kj}^{\text{potential}}$ and B_{kj}^{pulley} are the viscous, total, potential and pulley damping, and $kj = 22$ for sway and $kj = 66$ for yaw.

The three terms on the right hand side were obtained separately. The total damping was identified from the wet decay tests (Section 5.1), the pulley damping from dry tests of the springs and pulleys (Section 5.2) and the potential damping with the diffraction software DIFFRAC (Section 5.3). The added mass and the damping were then made dimensionless (Section 5.4). Additional plots and tables of this chapter are given in Appendix B.

5.1 Total Damping from Moored Decay Tests

Each moored decay run produces two data files, recorded by independent acquisition systems that start logging at the same instant (Section 4.9). The first contains the fore and aft laser distance sensors, sampled at 1 kHz, and the second the six degrees of freedom of the OptiTrack motion capture system, sampled at 100 Hz. Both cover at least 60 s, with lengths in millimeters and angles in degrees. The OptiTrack sway channel `CT_Y` is the primary signal of the sway tests and the yaw channel `CT_Yaw` that of the yaw tests. The lasers serve as an independent check on these channels, and the remaining OptiTrack channels were used only to diagnose cross coupling. Runs marked as failed in the test log were discarded. The remaining runs were processed in the same sequence for both degrees of freedom: release detection, trimming and zero centering, comparison of the camera with the laser reconstruction at the center of the model, and filtering.

5.1.1 Release Detection, Trimming and Zero Centering

Each run starts while the model is still held at its initial displacement by the electromagnets (Section 4.8). The recording was started first, and the model was released a few seconds later by cutting the power to the electromagnets, so that the decay begins part of the way into each record (Figure 17). The analysis starts at the release, with the model at rest at its initial displacement. The release point therefore had to be identified, and the part of the record before it was discarded.

The release is detected in the primary signal s of the test. While the model is held, this signal only fluctuates by the measurement noise around a constant level, the baseline, which is the mean of a stretch

of the record where the signal is still. The release is the first sample at which the signal departs from the baseline by more than a threshold and stays away from it for a window of consecutive samples. The window prevents a single noisy sample from being taken as the release, and comparing with the baseline instead of with the previous sample also finds the onset of motion when the release is gradual. The threshold follows the noise of the signal, so it differs between sway and yaw. The release sample is

$$k_{rel} = \min\left\{k \;:\; \left|s_j - \bar{s}_b\right| > \delta \text{ for } j = k, \ldots, k + n_w - 1\right\}, \tag{17}$$

where k_{rel} is the release sample, s_j is the primary signal at sample j, $\bar{s}_b$ is the baseline, δ is the threshold and n_w is the length of the window in samples.

The record is then cut at the release sample and the time is reset to zero, so that every record starts from the release with the model at rest. The laser record is cut at the same instant.

After trimming, the signals still carry the offset of the calibration, so their zero does not coincide with the equilibrium position of the model. This offset is removed by forcing the tail of the record, where the model has come to rest, to zero. The mean of the tail is subtracted from the whole record,

$$s_0(t_k) = s(t_k) - \frac{1}{N_t} \sum_{j=N-N_t+1}^{N} s(t_j), \tag{18}$$

where s_0 is the zero centered signal, s is the trimmed signal, t_k is the time of sample k, N is the number of samples of the record and N_t is the number of samples in the tail. After this step the displacements are measured from the equilibrium position of each run.

5.1.2 Sway and Yaw at the Center of the Model

The camera system reports the motion of one marker on the deck, which was selected as the rigid body and placed at the center of the deck (Figure 45). Its sway and yaw channels are therefore directly the motion at the center of the model. The lasers, in contrast, measure the lateral displacement of the backbone at two stations, one at the fore and one at the aft end of the model, at the same distance from its center. Treating the model as a straight line, the sway and yaw at the center follow from the two readings as

$$y_c = \frac{y_{fore} + y_{aft}}{2}, \qquad \psi = \arctan\left(\frac{y_{fore} - y_{aft}}{2L_{arm}}\right), \tag{19}$$

where y_c is the sway at the center, ψ is the yaw angle, y_{fore} and y_{aft} are the lateral displacements measured by the fore and aft laser and L_{arm} is the distance of each laser from the center of the model.

The laser reconstruction is an independent measurement of the same motion and was used to check the camera signals. The lasers are sampled at 1 kHz and the camera at 100 Hz, so the laser signal was first interpolated onto the time grid of the camera. The remaining time shift between the two acquisition systems was found with a cross correlation of the two signals and removed. The two signals were then compared through their difference,

$$d(t_k) = s_{cam}(t_k) - s_{las}(t_k + \tau), \tag{20}$$

where $d(t_k)$ is the difference at time t_k, s_{cam} is the camera signal, s_{las} is the laser reconstruction and τ is the time shift between them. A run was discarded if the absolute difference exceeded 1.0 mm in sway or

0.03° in yaw anywhere in the record. Figure 18 shows the comparison after trimming and zero centering. The camera signals are used alone from here on.

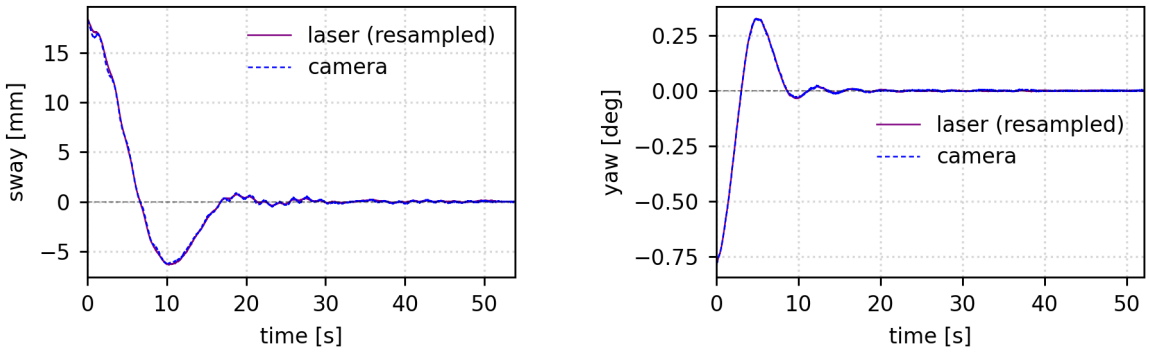

(a) Sway.

(b) Yaw.

Figure 18: Comparison of the camera signal with the laser reconstruction at the center of the model, for a sway run (a) and a yaw run (b) of Case 2, after trimming and zero centering.

5.1.3 Filtering

In the sway signal of Figure 18 a high frequency oscillation can be seen. It comes from the roll and surge motions of the model (Figure 17), which appear in the sway signal at higher frequencies than the sway itself. The frequency bands of the motions were identified with spectrograms: the sway lies at or below about 0.11 Hz, the surge above about 0.15 Hz and the roll at about 0.5 Hz. The high frequency content can therefore be removed with a low pass filter. A fourth order Butterworth filter with a cutoff frequency of 0.14 Hz was applied to all sway signals, above the sway band and below the surge band. Its magnitude response is

$$|H(f)| = \frac{1}{\sqrt{1 + (f/f_c)^{2n}}}, \tag{21}$$

where $|H|$ is the gain of the filter at the frequency f, f_c is the cutoff frequency and n is the order of the filter. The filter was applied forward and backward, which cancels the phase shift, so that the timing of the turning points of the signal is not changed. The cutoff was checked against the sway frequency of every run, so that no part of the sway motion is cut off, and a run that did not meet the requirement was discarded.

The yaw signal in Figure 18 does not show this high frequency content. In the raw data (Figure 17), the surge is mainly present in the yaw tests, and it lies close to the frequency range of the yaw motion. It therefore cannot be separated from the yaw by filtering. It is not removed, because its amplitude is small compared with the yaw motion, and a filter that would remove it would also cut part of the yaw motion. For yaw, only a low pass filter of the same type is applied, with a cutoff frequency well above the yaw frequency. Figure 19 shows the effect of the filters: the high frequency content of the sway signal is removed, while the filtered yaw signal is practically the same as the raw one.

Of the 45 sway and 43 yaw runs, 43 and 39 passed all of these checks. The filtered camera signal of these runs is the signal passed to the equation of motion fit (Section 5.1.4).

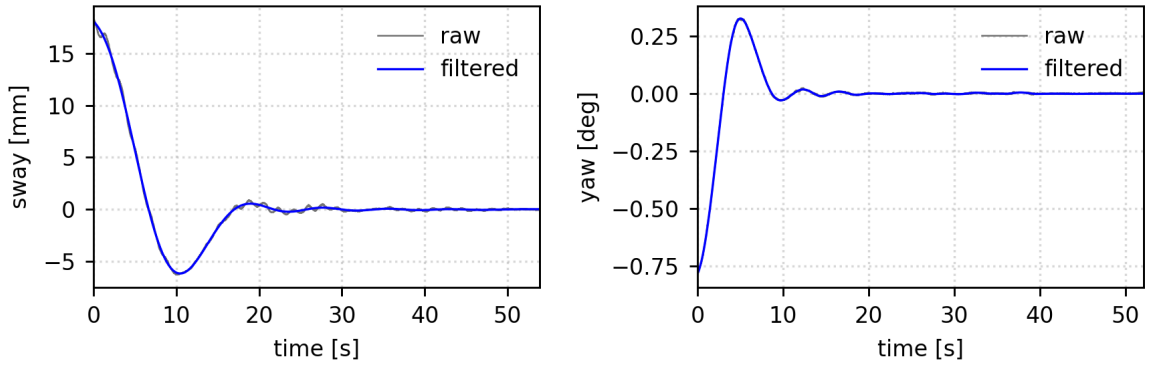

(a) Sway.

(b) Yaw.

Figure 19: Effect of the filters on the raw signal of a sway run (a) and a yaw run (b) of Case 2.

5.1.4 Equation of Motion Fit

The equation of motion of Chapter 3 (Equations 8 and 9) was fitted to the filtered decay record of every run to obtain the added mass and the damping coefficients. Sway and yaw were treated in the same way. The mooring stiffness C and the mass M of the model, or its moment of inertia for yaw, follow from independent calibration (Section 4.4) and were kept fixed. The added mass A and the damping coefficients B_1 and B_2 are the unknowns. The fit uses the camera signal, filtered as described in Section 5.1.3. The measurements are in millimeters and degrees and the equation is solved in meters and radians, so the conversion is made when the simulation is compared with the measurement.

The record starts at the release, where the model is at rest. The initial conditions are therefore measured and not fitted: the initial displacement is the first sample of the record and the initial velocity is zero.

For a set of parameters, the equation of motion is written as a first order system and integrated forward in time from the release with an explicit Runge Kutta scheme. The solution is evaluated at the time stamps of the OptiTrack system and compared with the measured displacement. The fit follows the same approach as De Boer and Buchner [2]: the parameters are found by minimizing the sum of the squared differences between the simulated and the measured displacement. The cost is not weighted, so the large first half-cycle contributes most to it. The cost has several local minima, because the added mass and the damping both shape the decay. It is therefore minimized with the derivative free Nelder Mead method from several starting points, and the solution with the lowest cost is kept. The number of starting points that reach this solution is used as a check on its uniqueness. The parameters are restricted to physical values: the inertia term $M + A$ must be positive and the damping coefficients must not be negative. The quality of a fit is expressed by the cost and by the root mean square error derived from it,

$$J = \sum_{k=1}^{N} \left(x_{meas}(t_k) - x_{sim}(t_k)\right)^2, \qquad \text{RMSE} = \sqrt{\frac{J}{N}}, \tag{22}$$

where J is the cost, x_{meas} and x_{sim} are the measured and the simulated displacement at the time t_k of sample k, N is the number of samples in the fit window and RMSE is the root mean square error of the fit.

The model was first fitted with a constant added mass over the full filtered record, with A, B_1 and B_2

all free. Figure 20 shows that this fit cannot follow the decay. The simulated half-cycles have a nearly constant period, so they drift out of phase with the measured half-cycles, and the quadratic damping term does not remove this drift. The drift is a difference in period, so the period of the decay is examined next.

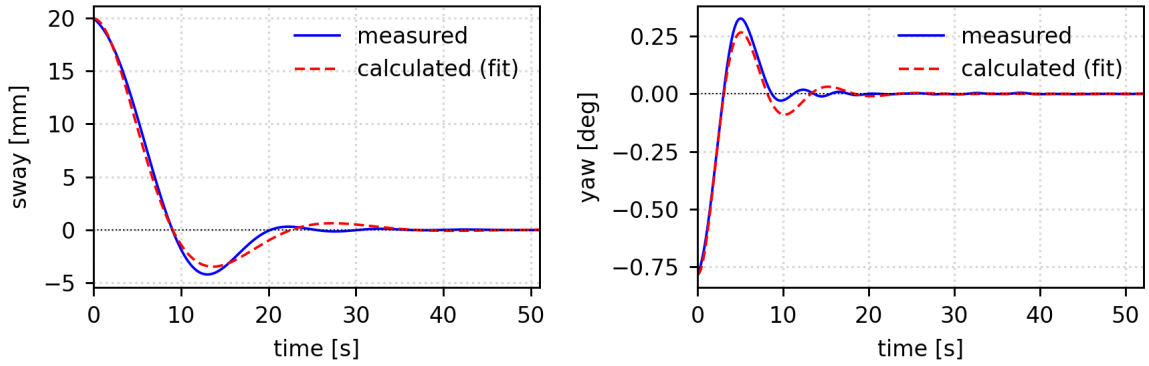

(a) Sway.

(b) Yaw.

Figure 20: Measured decay and fit of the equation of motion with a constant added mass and free damping coefficients B_1 and B_2, for a sway run (a) and a yaw run (b) of Case 12.

5.1.5 Period of the Decay

The drift between the simulation and the measurement in Figure 20 is a difference in period: the period of the measured decay is not constant. In the filtered records, the second half-cycle, as defined below, is shorter than the first by 15 to 30% in sway and by 5 to 17% in yaw, depending on the case (Table 8).

The period was measured per half-cycle, defined as the motion between two consecutive extrema of the filtered signal, either from a peak to the next trough or from a trough to the next peak. Two half-cycles form one oscillation. The first half-cycle starts at the release, where the model is at its initial displacement, and each following half-cycle starts where the previous one ends. Half-cycles give twice as many values per run as full oscillations, which allows the change of the period to be followed through the decay. The duration of a half-cycle is half the period of the oscillation, and is therefore referred to as the half period,

$$T_{1/2,i} = t_{e,i} - t_{e,i-1}, \qquad i = 1, 2, \ldots, \tag{23}$$

where $T_{1/2,i}$ is the duration of half-cycle i, $t_{e,i}$ is the time of the ith extremum and $t_{e,0} = 0$ is the release. The extrema are taken at the samples of the camera, so the durations have a resolution of 0.01 s. Figure 21 shows the first three half-cycles of a sway run and a yaw run of Case 2, with the duration of each indicated above it.

The decays contain only a few oscillations. The third half-cycle in Figure 21 has an amplitude of a few tenths of a millimeter in sway and a few hundredths of a degree in yaw, which is close to the noise of the signal, so only the first two half-cycles are considered. The first half-cycle is the less accurate of the two, because it starts at the release, where the model is still influenced by the release from the electromagnets. In a decay with many oscillations it would be excluded, but here this would leave a single half-cycle, and the change of the period could not be examined. It is therefore retained, and its limited accuracy is taken into account when interpreting the results. Table 8 gives the mean duration of the first two half-cycles over the runs of each case, for sway and for yaw, together with the number of runs and

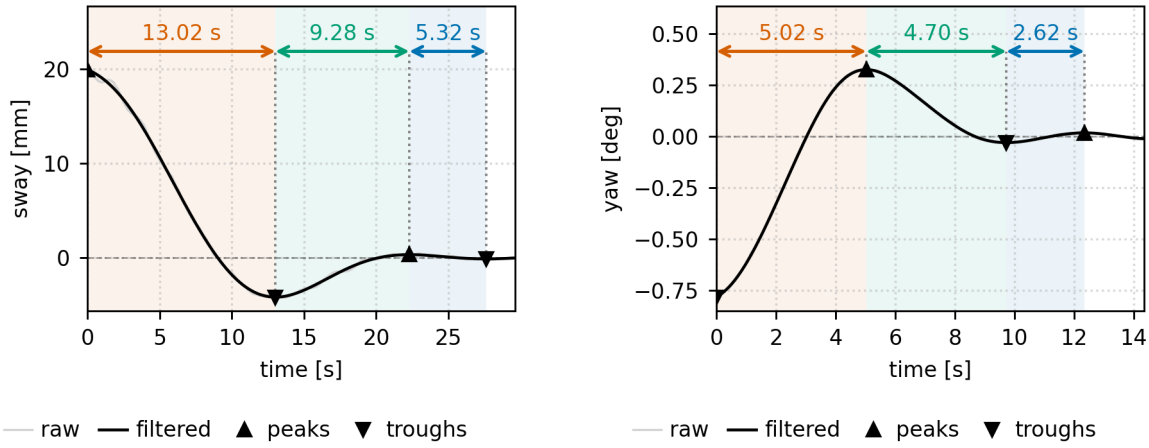

(a) Sway.

(b) Yaw.

Figure 21: Half-cycles of the filtered signal for a sway run (a) and a yaw run (b) of Case 2. The triangles mark the peaks and the troughs, and the shaded areas the first three half-cycles with their durations $T_{1/2}$.

the standard deviation over the runs as a measure of the repeatability of the case.

Table 8: Mean duration of the first two half-cycles, $T_{1/2,1}$ and $T_{1/2,2}$, over the runs of each case, for sway and yaw. The number of runs of the case is n and SD is the standard deviation over these runs. All durations are in seconds.

			Sway					Yaw				
				$T_{1/2,1}$		$T_{1/2,2}$			$T_{1/2,1}$		$T_{1/2,2}$	
Case	h [mm]	G [mm]	n	Mean	SD	Mean	SD	n	Mean	SD	Mean	SD
1	172	Unconfined	4	10.71	0.05	8.12	0.06	3	3.97	0.01	3.48	0.08
2	172	69	3	12.98	0.06	9.26	0.14	5	5.04	0.02	4.66	0.04
3	172	46	3	13.65	0.01	10.06	0.18	3	5.36	0.07	4.57	0.03
4	172	34	3	14.08	0.05	9.94	0.46	3	5.62	0.04	4.65	0.15
5	194	Unconfined	5	9.25	0.03	7.33	0.08	4	3.75	0.03	3.15	0.02
6	194	69	2	9.90	0.02	6.93	0.11	3	4.25	0.04	3.97	0.01
7	194	46	3	10.42	0.05	8.44	0.06	3	4.44	0.01	4.13	0.05
8	194	34	3	10.84	0.04	8.52	0.05	3	4.60	0.01	4.22	0.05
9	222	Unconfined	5	8.28	0.03	7.00	0.08	3	3.47	0.02	3.10	0.02
10	222	69	5	8.80	0.15	7.46	0.27	3	3.92	0.02	3.73	0.10
11	222	46	4	9.04	0.10	7.44	0.04	3	4.00	0.01	3.74	0.05
12	222	34	3	9.64	0.06	7.56	0.11	3	4.21	0.03	3.76	0.03

The standard deviation over the runs of a case describes the repeatability of the half periods. In sway it is 0.01 to 0.15 s for the first half-cycle and 0.04 to 0.46 s for the second, and in yaw it is 0.01 to 0.07 s and 0.01 to 0.15 s. In every case the difference between the first and the second half period is larger than the standard deviation of either, so the shortening of the period is not caused by a scatter between the runs. The cases have three to five runs, except sway Case 6, where one of three runs was discarded and the standard deviation rests on two values.

The mass of the model and the stiffness of the mooring are fixed, and the damping coefficients could

not account for the change of the period (Figure 20). The change is therefore attributed to the added mass, which must depend on the amplitude of the motion. This rests on the assumption of a constant mooring stiffness: an amplitude dependence of the restoring force would appear as part of the amplitude dependence of the identified added mass.

5.1.6 Amplitude Dependent Added Mass

The shortening of the period was attributed to an added mass that depends on the amplitude of the motion. The added mass was therefore determined for every half-cycle separately, for sway and for yaw, where it is the added moment of inertia. Each half-cycle (Section 5.1.5) is given one amplitude, the mean of the absolute displacements at its two turning points,

$$a_{m,i} = \tfrac{1}{2}\left(|x(t_{e,i-1})| + |x(t_{e,i})|\right), \tag{24}$$

where $a_{m,i}$ is the amplitude of half-cycle i and $x(t_{e,i})$ is the displacement at extremum i.

The half period, and with it the added mass, follows from the times of the turning points that bound each half-cycle, so these turning points must lie clearly above the noise of the signal. Two limits were therefore applied. The first, a noise floor, is used to detect the turning points. It was determined from the filtered signal at the end of each record, after the motion has died out, and set at 0.12 mm in sway and 0.01° in yaw, above every excursion of the noise found in any run, so that noise cannot be mistaken for a turning point. The second, an amplitude threshold, decides which half-cycles are used. It was set at about eight times the noise floor, at 1 mm in sway and 0.08° in yaw, so that the noise has only a small influence on the half period at the threshold. In every run the second half-cycle has an amplitude $a_{m,i}$ of at least 1.8 mm in sway and 0.11° in yaw, while the third has at most 0.6 mm and 0.05°. The threshold therefore lies in the gap between the two, and in practice it keeps exactly the first two half-cycles of every run, which are used to determine the added mass and the damping

The small amplitudes were also excluded because of the behavior of the springs and pulleys. In the dry tests (Section 5.2) their damping starts to rise gradually and their period starts to shorten below an amplitude of about 5 mm. Down to 2 mm these changes remain moderate, so the damping of the springs and pulleys was represented by one constant value down to this amplitude, and this value is the one subtracted from the total damping (Equation 16). Below 2 mm their behavior was not characterized. The damping that the fit returns is determined mainly by the large first half-cycle, because the cost is not weighted (Section 5.1.4). This is also the range of interest, since the damping force grows with the velocity and the viscous damping is therefore most important when the vessel oscillates with high velocities. Limiting the analysis to the first two half-cycles focuses on these large motions and avoids having to account for the springs and pulleys at the smallest amplitudes.

Two methods were used to determine the added mass and the damping, both with the cost function, optimizer and restrictions of Section 5.1.4.

Method 1: Added Mass from the Period of Each Half-Cycle

In the first method the added mass of every half-cycle follows from its measured half period. The half period gives a local angular frequency $\omega = \pi/T_{1/2}$, and the undamped equation of motion then gives

the added mass of the half-cycle,

$$A = \frac{C}{\omega^2} - M, \tag{25}$$

where C is the stiffness of the mooring and M is the mass of the model, the moment of inertia for yaw. No optimizer is involved, and every half-cycle gets its own added mass.

The damping was then fitted with the added mass of every half-cycle fixed at its value from Equation 25. In half-cycle i the equation of motion is

$$(M + A_i)\,\ddot{x} + B_1\dot{x} + B_2\,|\dot{x}|\,\dot{x} + Cx = 0, \tag{26}$$

where x is the displacement (sway or yaw), A_i is the added mass of half-cycle i, and B_1 and B_2 are the linear and the quadratic damping coefficients. Each half-cycle is integrated separately, starting from rest at its measured turning point, and the half-cycles are joined into one simulated record. One pair B_1, B_2 is fitted to the two half-cycles of a run together, with the cost function, optimizer and restrictions of Section 5.1.4.

Equation 25 treats the time between two turning points, which in a damped decay is the damped half period, as if it were undamped. Since damping lengthens the period, this overestimates the added mass, most of all in the most strongly damped cases (Section 6.1.1).

Method 2: Added Mass as a Function of the Half-Cycle Amplitude

In the second method the added mass is not calculated from the period but fitted, as a linear function of the amplitude of the half-cycle. It is constant within a half-cycle and changes from one half-cycle to the next with its amplitude $a_{m,i}$,

$$\left(M + A_0 + A_1\,a_{m,i}\right)\ddot{x} + B_1\dot{x} + B_2\,|\dot{x}|\,\dot{x} + Cx = 0 \qquad \text{in half-cycle } i, \tag{27}$$

where x is the displacement (sway or yaw), M is the mass of the model, A_0 and A_1 are the intercept and the slope of the added mass against the amplitude, $a_{m,i}$ is the amplitude of half-cycle i, B_1 and B_2 are the linear and the quadratic damping coefficients and C is the stiffness of the mooring. In contrast with Method 1, the decay is simulated as one continuous record from the release: at the end of a half-cycle the simulated displacement and velocity are carried over into the next. The four parameters A_0, A_1, B_1 and B_2 are fitted together. With two half-cycles per run the model has one added mass per half-cycle, like Method 1, but these are now found from the shape of the whole decay instead of from the period alone.

5.1.7 Quadratic Damping

With B_2 free in both methods, the quadratic damping converged to zero in every yaw run and in most sway cases. It was positive in only four sway cases: Cases 2, 3 and 4, the confined cases at the smallest under keel clearance, and Case 6, the case with the largest lateral gap at the intermediate under keel clearance. It could not be identified reliably from the decays.

Where B_2 is positive, it differs strongly between the runs of the same case, while B_1 varies much less in relative terms. The physical reason is that quadratic damping differs from linear damping only through its dependence on the amplitude: a large half-cycle is damped relatively more than a small one.

Resolving this dependence requires a decay that covers a wide range of amplitudes and velocities. These decays contain only two half-cycles, in which the amplitude and the velocity change by a limited factor, and the velocities are very small, so the square of the velocity is much smaller than the velocity itself and the quadratic term contributes only a minor part of the damping force. A large change in B_2 therefore changes the decay only slightly, and small differences between runs lead to large differences in B_2.

Table 9 gives B_2 and B_1 of every run of the four cases with a positive B_2, fitted with B_2 free and with $B_2 = 0$. B_2 differs by more than a factor of 3 between the runs of Case 4, from 9 800 to 32 300 N s^2/m^2, and B_1 with B_2 free differs accordingly. With B_2 free, the fit also does not always end at the same B_1 and B_2 when it is started from different values. In Method 1 it does: all starting points end at the same values in every run. In Method 2 only 72 of the 132 starting points (55 %) do with B_2 free, against 164 of 176 (93 %) with $B_2 = 0$ in the same runs. The other starting points stop at $B_2 = 0$ or at other values (Section B.4.1).

Table 9: Sway: B_2 [N s^2/m^2] and B_1 [N s/m] with B_2 free, and B_1 [N s/m] with $B_2 = 0$, for every run of the cases with a positive B_2, in Method 1 and Method 2. ΔRMSE [mm] is the increase of the RMSE when B_2 is set to zero.

		Method 1				Method 2			
		B_2 free		$B_2 = 0$		B_2 free		$B_2 = 0$	
Case	Run	B_2	B_1	B_1	ΔRMSE	B_2	B_1	B_1	ΔRMSE
2	178	9 500	220.7	243.1	0.010	9 800	223.6	246.6	0.008
	180	7 900	220.0	238.8	0.008	8 400	223.8	243.7	0.007
	182	8 700	224.5	245.0	0.008	8 200	231.5	250.9	0.006
3	185	3 900	241.4	251.1	0.002	3 000	250.4	257.8	0.001
	187	4 600	241.7	253.1	0.003	4 300	248.3	259.0	0.002
	189	9 400	226.3	249.8	0.013	9 700	231.9	255.9	0.010
4	157	32 300	222.7	294.4	0.032	34 400	217.2	294.2	0.031
	201	9 800	259.4	281.5	0.005	10 300	260.0	283.3	0.005
	203	9 900	255.2	277.9	0.006	10 600	255.0	279.2	0.006
6	250	14 700	146.8	186.5	0.039	15 600	148.3	190.3	0.031
	252	10 800	154.8	184.0	0.024	11 500	156.9	187.8	0.019

Setting B_2 to zero changes the fit very little. The median increase of the RMSE over the 11 runs is 0.008 mm in Method 1 and 0.007 mm in Method 2, smaller than the noise of the filtered signal, and the largest increase is 0.039 and 0.031 mm. Figure 22 shows both methods for run 157 of Case 4, the run with the largest quadratic damping of the case in which B_1 changes the most. With $B_2 = 0$, B_1 increases from 222.7 to 294.4 N s/m in Method 1 and from 217.2 to 294.2 N s/m in Method 2, and the RMSE increases by 0.03 mm in both methods. The fitted decays differ by at most 0.34 mm. The other cases are shown in Section B.4.

The quadratic damping was thus set to zero in both methods, for sway and yaw. B_1 then contains all damping of the decay and can be regarded as an equivalent linear damping. This does not mean that the quadratic damping is absent, but that it cannot be separated from the linear damping with the few oscillations of these decays. Setting it to zero also makes the decomposition of Equation 16 consistent, since the potential damping and the damping of the pulleys are linear as well. With $B_2 = 0$ the fit also converges: in Method 1 all starting points of all runs end at the same B_1, in sway and in yaw (Section B.5).

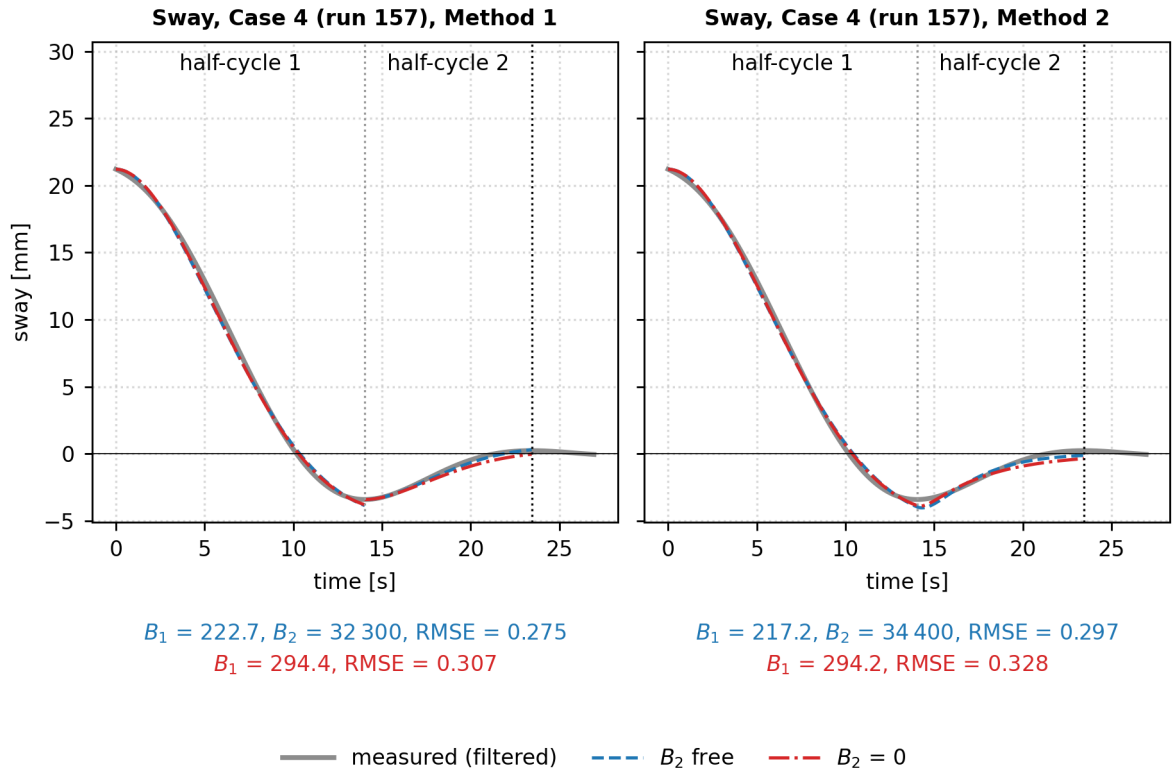

Figure 22: Sway decay of run 157 of Case 4, fitted with B_2 free and with $B_2 = 0$ in Method 1 (left) and Method 2 (right). Values: B_1 [N s/m], B_2 [N s^2/m^2], RMSE [mm].

5.2 Pulley Damping from the Dry Tests

The springs and pulleys of the mooring dissipate energy that cannot be separated from the hydrodynamic damping in a wet decay. Their damping was therefore measured in dry decay tests (Section 4.5), which were processed like the wet records (Section 5.1), except that they have a single laser channel and were not filtered.

In the wet tests the springs and pulleys move with the vessel, so the amplitudes at which they dissipate energy are those of the half-cycles used to determine the total damping (Section 5.1.6). These half-cycles start from a release amplitude of 16 to 22 mm in sway and of 16 to 20 mm at the mooring lines in yaw, and the second half-cycle starts at no less than 3.4 mm in sway and 5.4 mm in yaw. The energy of a decay scales with the square of the amplitude, so more than 98 % of the initial energy is dissipated before the amplitude has fallen to 2 mm. The behavior of the springs and pulleys at smaller amplitudes therefore has little influence on the damping identified from the wet decays, and their damping is determined from the release down to an amplitude of 2 mm. The dry tests were released from about 20 mm and cover this range.

In the dry tests the lead block hangs on a rope, which acts as a pendulum with a damping of its own. The vessel has no such rope, so this contribution has to be removed. The bare pendulum was therefore tested first, without springs and pulleys, and its damping follows from the logarithmic decrement of consecutive crests and troughs (Appendix B.6). This gives $B_{pendulum} = 0.087$ N s/m, which is almost zero compared with the damping of the springs and pulleys.

With the springs and pulleys attached, the period of a cycle is constant at large amplitudes: above an

amplitude of 5 to 8 mm, depending on the run, it stays within about 3 % of 2.13 to 2.15 s. Below this amplitude it shortens, by 3 to 9 % at 4 mm and by 11 to 18 % at 2 mm (Figure 23). The springs and pulleys therefore become stiffer at small amplitudes. The damping coefficient changes in the same way: it is approximately constant above about 5 mm and rises gradually below it. Down to 2 mm this rise is moderate, since ending the fit at 5 mm instead of 2 mm changes the fitted damping coefficient by only about 8 %. The damping coefficient of the springs and pulleys was therefore taken as independent of the amplitude over the whole range, so that a single value describes it. The total damping of the wet tests is treated in the same way (Section 5.1.7), so the two can be subtracted directly.

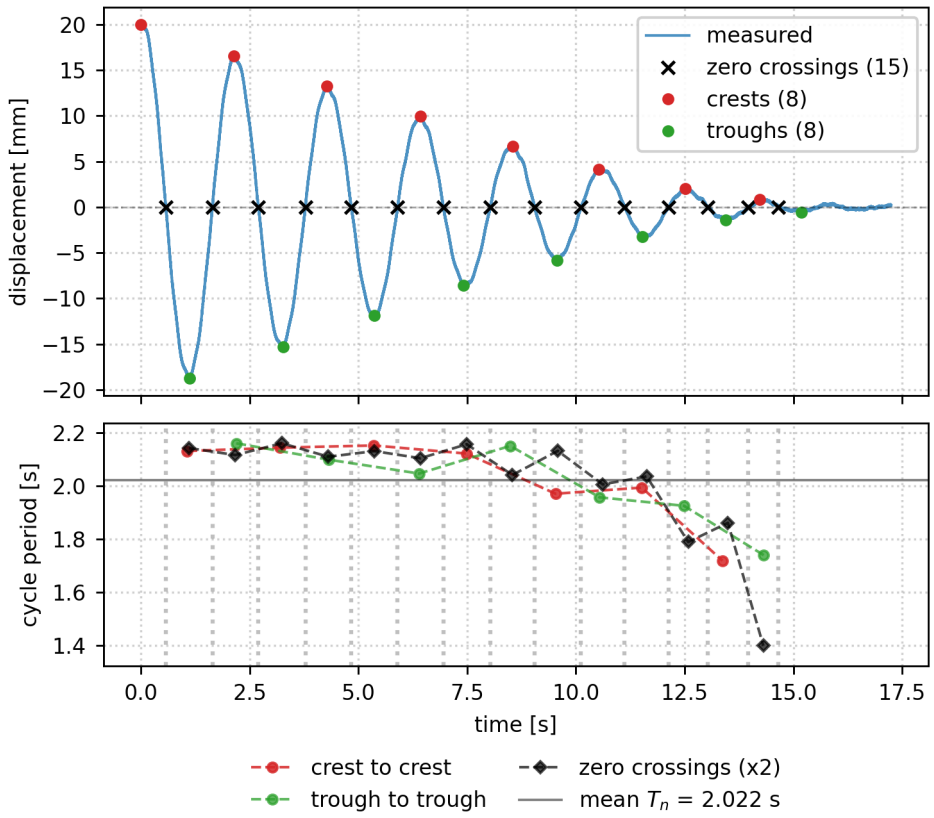

Figure 23: Dry test of the aft springs and pulleys for one run: displacement (top) and period of every cycle (bottom).

The damping coefficient is identified by fitting the equation of motion of the mass to the measured decay of each run (Figure 24),

$$m\ddot{x} + B_1\dot{x} + B_2\,|\dot{x}|\,\dot{x} + Cx = 0, \tag{28}$$

where x is the displacement of the mass, m is its mass, B_1 and B_2 are the linear and the quadratic damping coefficients and C is the stiffness, which is kept as a free parameter in the fit. The initial conditions are the measured release displacement and zero velocity. The equation is integrated numerically, and the coefficients are determined as the values that minimize the RMSE between the computed and the measured displacement (Equation 22). The fit extends from the release to the point at which the amplitude of the turning points has decreased to 2 mm. The quadratic coefficient B_2 converged to zero in every run, so the damping of the springs and pulleys is linear and is described by B_1 alone, as assumed in the decomposition of the viscous damping.

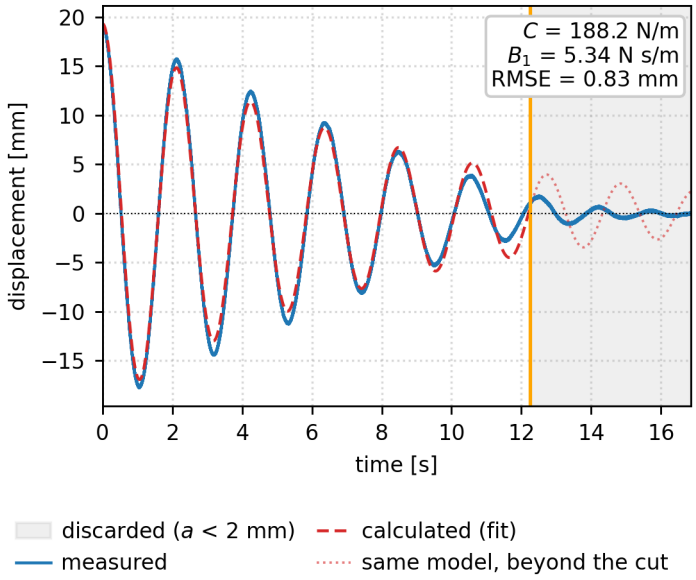

Figure 24: Measured displacement and fit of Equation 28 for one run of the aft set. The fit ends where the amplitude has fallen to 2 mm (vertical line).

The fit was performed separately for the aft and for the fore set, which each hold two of the four springs. Both fitted dampings contain the rope, so the damping of the bare pendulum is subtracted from each, even though it is small, and the two sets are then added to give the four springs and their pulleys,

$$B_{22}^{\text{pulley}} = \left(B_{aft} - B_{pendulum}\right) + \left(B_{fore} - B_{pendulum}\right), \tag{29}$$

where B_{22}^{pulley} is the damping of the springs and pulleys in sway, B_{aft} and B_{fore} are the linear damping coefficients B_1 of the aft and the fore set and $B_{pendulum}$ is the damping of the bare pendulum. This gives $\boldsymbol{B_{22}^{\text{pulley}} = 9.1 \pm 0.5\ \text{N s/m}}$, where the spread is one standard deviation between the runs.

For yaw, both sets act at the lever arm $L_{arm} = 1.41$ m from the center of the model, so their damping forces give a damping moment,

$$\boldsymbol{B_{66}^{\text{pulley}} = B_{22}^{\text{pulley}}\, L_{arm}^2 = 18.2\ \text{N m s/rad}}, \tag{30}$$

where B_{66}^{pulley} is the damping of the springs and pulleys in yaw and L_{arm} is the distance of the sets from the center of the model.

The uncertainty of the damping coefficient has two sources: the spread between the runs, about 5 %, and the dependence on the amplitude range, about 8 %. Together they amount to the order of 10 %. The effect on the viscous damping depends on the share of the springs and pulleys in the total linear damping, which is 3 to 9 % in sway and 10 to 25 % in yaw, depending on the case (Chapter 6). An error of 10 % in the damping of the springs and pulleys therefore changes the viscous damping by at most about 1 % in sway and 3 % in yaw, so a single value is sufficient for the decomposition.

The dry tests were done at about 0.5 Hz, which is 3 to 12 times higher than the frequency at which the vessel responds, 0.04 to 0.07 Hz in sway and 0.09 to 0.16 Hz in yaw, and with the spring tension of the test. The transfer to the vessel therefore assumes that neither the frequency nor the tension changes the damping.

5.3 Potential Damping from DIFFRAC

The potential damping is the part of the damping that comes from the waves radiated by the oscillating vessel, and it has to be known to separate it from the viscous damping (Equation 11). It was computed with the diffraction software DIFFRAC, which solves the frequency domain diffraction and radiation problem of linear potential flow theory on a panel mesh of the wetted hull. For a range of angular frequencies ω it returns the added mass $A_{kj}(\omega)$ and the potential damping $B_{kj}(\omega)$ of the frequency domain equation of motion (Equation 5), where $kj = 22$ for sway and $kj = 66$ for yaw. MARIN, the developer of DIFFRAC, was consulted on the use of the software at model scale. Since the calculation is linear, it makes no significant difference whether it is made at model or at full scale, so the calculations were made at model scale. According to MARIN, DIFFRAC has been validated down to an under keel clearance of about 4 m at full scale. The smallest lateral gap of 3 m is not expected to be problematic, but the smallest under keel clearance of 1.5 m lies outside this validated range.

The box shaped hull was described by flat panels on the bottom, the two sides and the two ends below the waterline, with the dimensions, the mass, the inertia and the water depth of the tested cases (Table 4) and the density of the fresh water of the flume. For the berth cases the quay option of DIFFRAC places a rigid vertical wall over the full water depth at a distance from the centerline of half the beam plus the lateral gap. For the laterally unconfined cases the model lies between the two side walls of the flume, which were described by their own fixed panel meshes over the full water depth and are ten times as long as the model, so that their ends are far from the model (Figure 25). In the narrow gap between the hull and the quay, linear potential flow predicts undamped standing waves of the free surface, which would produce resonant peaks in the coefficients at frequencies where no such resonance exists in reality. To prevent this, a damping lid with a dimensionless damping coefficient of 0.03 was placed on the free surface in the gap. No lid is used for the unconfined cases, where the gap to the flume walls is large. The mesh of the hull was refined by increasing the number of panels along the length, across the half beam and over the draft with the same factor, from 356 to 12 816 hull panels. The convergence was assessed for the smallest gap, which places the highest demand on the mesh. The added mass converged with refinement, while the potential damping remained more sensitive to the mesh. It is, however, very small compared with the pulley damping (Section 5.2), so its remaining mesh dependence does not affect the viscous damping. The level at which the added mass had converged was used for all calculations. The mesh levels, the dimensions of the damping lid and the convergence study are given in Appendix B.7.

The coefficients were computed at equally spaced frequencies between $\pi/T_{1/2,max}$ and $\pi/T_{1/2,min}$, with $T_{1/2,max}$ and $T_{1/2,min}$ the longest and the shortest half-cycle of the case in Table 8, separately for sway and for yaw. The added mass and the potential damping averaged over this frequency range are presented for each case in Table 10. The comparison of the added mass with the values from the experiments is given in Section 6.1.1.

Over the frequency range of a case, the added mass from DIFFRAC changes by less than 3 %, so one mean value per case is given. The potential damping varies more with frequency, but it is negligible compared with the measured damping, below 0.3 % of B_1 in all cases.

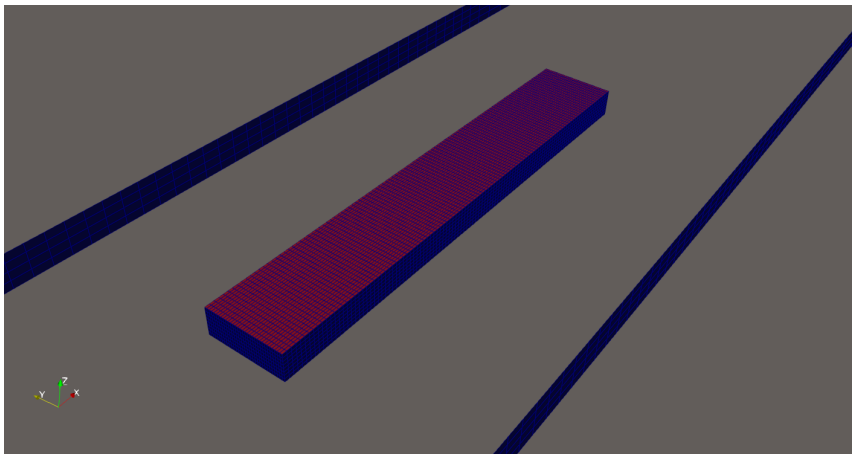

Figure 25: Panel mesh of the hull and the two flume walls of an unconfined case, visualized in ParaView.

Table 10: Added mass and potential damping from DIFFRAC at model scale, as the mean over the frequency range of each case.

Case	h [mm]	G [mm]	A_{22} [kg]	B_{22} [N s/m]	A_{66} [kg m^2]	B_{66} [N m s/rad]
1	172	Unconfined	813	0.0031	213.1	0.0013
2	172	69	1231	0.0260	392.0	0.2500
3	172	46	1307	0.0245	443.1	0.2405
4	172	34	1368	0.0400	480.0	0.2000
5	194	Unconfined	527	0.0015	167.8	0.0014
6	194	69	682	0.0365	260.8	0.1470
7	194	46	714	0.0170	285.7	0.1220
8	194	34	745	0.0160	306.5	0.1040
9	222	Unconfined	385	0.0052	136.5	0.0048
10	222	69	470	0.0165	197.6	0.0775
11	222	46	498	0.0150	216.4	0.0690
12	222	34	526	0.0145	233.5	0.0500

5.4 Normalization

The added mass and the damping were made dimensionless, so that they can be compared between the cases and the two degrees of freedom independently of the size of the model. A dimensionless coefficient is the measured quantity divided by a reference quantity with the same units. The reference quantities must be the same for every case, so that a difference in a coefficient reflects a difference in the added mass or the damping and not in the reference, and they must be consistent with Froude scaling, which governs the inertia and the gravity of the problem. They are built from the displaced mass $\rho\nabla$, the length L of the model and the acceleration of gravity g. Because the model floats, its displaced mass equals its mass, $\rho\nabla = M = 178.73$ kg. The coefficients are

$$a_{22} = \frac{A_{22}}{\rho\nabla}, \qquad b_{22} = \frac{B_{22}}{\rho\nabla\sqrt{g/L}}, \qquad a_{66} = \frac{A_{66}}{\rho\nabla L^2}, \qquad b_{66} = \frac{B_{66}}{\rho\nabla L^2\sqrt{g/L}}, \tag{31}$$

where a_{22} and a_{66} are the dimensionless added mass in sway and the dimensionless added moment of inertia in yaw, b_{22} and b_{66} are the dimensionless damping in sway and yaw, and $\sqrt{g/L} = 1.906\ \mathrm{s}^{-1}$ is the Froude reference frequency. The damping has the units of mass per unit time, so it is referred to the displaced mass and the Froude reference frequency: $\rho\nabla\sqrt{g/L} = 340.7$ kg/s in sway and $\rho\nabla L^2\sqrt{g/L} = 2484\ \mathrm{kg\,m^2/s}$ in yaw.

6

Results

6.1 Comparison of the two methods: added mass and damping

Chapter 5 described two methods to determine the added mass from a moored decay test. Method 1 derives the added mass from the half period (Section 5.1.6). Method 2 fits the added mass as a linear function of the half-cycle amplitude, together with the damping (Section 5.1.6). Both methods were applied to every run, with the quadratic damping coefficient set to zero (Section 5.1.7). This section compares the added mass and the damping obtained with the two methods and determines which results are used in the remainder of this chapter. Sway case 6 is excluded from all results of this chapter and is reviewed at its end (Section 6.4). Yaw case 6 shows no such deviation and is retained.

6.1.1 Added Mass

Table 11 (sway) and Table 12 (yaw) list for each case the durations $T_{1/2}$ of the first two half-cycles, the potential added mass from DIFFRAC at these periods (Table 10), the added mass obtained with both methods and its ratio to the potential added mass.

For the first half-cycle, both methods give similar results. In sway, the added mass amounts to 0.81 to 0.94 times the potential added mass for Method 1 and 0.74 to 0.95 times for Method 2. In yaw, the corresponding ranges are 0.69 to 0.79 and 0.55 to 0.74. For the second half-cycle, the two methods diverge. Method 1 remains within a narrow range of 0.36 to 0.48 in sway and 0.37 to 0.61 in yaw, whereas Method 2 ranges from 0.03 to 0.88 in sway and from 0.45 to 1.98 in yaw. In most yaw cases, Method 2 even exceeds the potential added inertia.

Table 11: Added mass per half-cycle: Method 1, Method 2 and DIFFRAC (case means).

Sway												
	$T_{1/2}$ [s]		A_{pot} [kg]		A_{M1} [kg]		A_{M2} [kg]		A_{M1}/A_{pot}		A_{M2}/A_{pot}	
Case	1	2	1	2	1	2	1	2	1	2	1	2
1	10.71	8.12	802	824	653	299	642	214	0.81	0.36	0.80	0.26
2	12.98	9.26	1227	1235	1044	443	1015	140	0.85	0.36	0.83	0.11
3	13.65	10.06	1304	1310	1174	556	1125	226	0.90	0.42	0.86	0.17
4	14.08	9.94	1367	1368	1259	539	1287	42	0.92	0.39	0.94	0.03
5	9.25	7.33	522	533	442	211	417	279	0.85	0.40	0.80	0.52
6	–	–	–	–	–	–	–	–	–	–	–	–
7	10.42	8.44	713	715	609	338	599	308	0.85	0.47	0.84	0.43
8	10.84	8.52	744	746	674	347	696	225	0.91	0.47	0.94	0.30
9	8.28	7.00	383	387	319	176	287	331	0.83	0.46	0.75	0.85
10	8.80	7.46	470	471	383	226	350	413	0.82	0.48	0.74	0.88
11	9.04	7.44	498	499	414	223	391	306	0.83	0.45	0.79	0.61
12	9.64	7.56	526	527	495	236	502	186	0.94	0.45	0.95	0.35

Figures 26 and 27 present the added mass of both methods for all cases, grouped by water depth, with

Table 12: Added inertia per half-cycle: Method 1, Method 2 and DIFFRAC (case means).

	Yaw											
	$T_{1/2}$ [s]		A_{pot} [kg m^2]		A_{M1} [kg m^2]		A_{M2} [kg m^2]		A_{M1}/A_{pot}		A_{M2}/A_{pot}	
Case	1	2	1	2	1	2	1	2	1	2	1	2
1	3.97	3.48	211	215	148	95	131	206	0.70	0.44	0.62	0.96
2	5.04	4.66	390	394	287	233	254	469	0.73	0.59	0.65	1.19
3	5.36	4.57	440	446	335	221	315	285	0.76	0.50	0.72	0.64
4	5.62	4.65	475	485	376	232	353	218	0.79	0.48	0.74	0.45
5	3.75	3.15	166	170	123	63	105	152	0.74	0.37	0.63	0.89
6	4.25	3.97	261	261	181	148	162	317	0.69	0.57	0.62	1.21
7	4.44	4.13	285	286	205	166	182	337	0.72	0.58	0.64	1.18
8	4.60	4.22	306	307	225	177	204	327	0.74	0.58	0.67	1.06
9	3.47	3.10	136	137	94	59	75	214	0.69	0.43	0.55	1.56
10	3.92	3.73	197	198	142	121	119	392	0.72	0.61	0.60	1.98
11	4.00	3.74	216	217	151	122	129	376	0.70	0.56	0.60	1.73
12	4.21	3.76	233	234	176	125	158	247	0.75	0.53	0.68	1.06

the gap decreasing from left to right. For the first half-cycle, both methods show the same dependence on confinement: the added mass increases as the gap and the UKC decrease. Method 1 shows the same dependence for the second half-cycle, albeit weaker. The added mass of the second half-cycle from Method 2, in contrast, shows no consistent dependence on either the gap or the UKC. In sway at $h = 222$ mm, for instance, it decreases from 413 kg at $G = 69$ mm to 186 kg at $G = 34$ mm, opposite to the expected trend. Relative to the first half-cycle, it is smaller in some cases and larger in others.

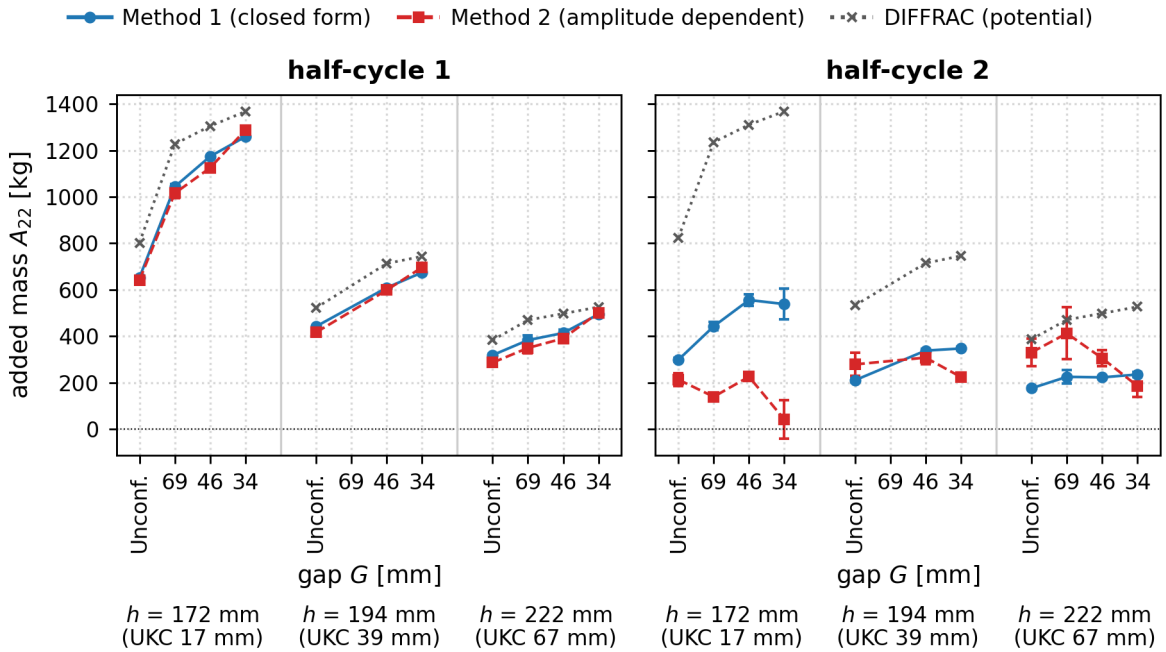

Figure 26: Added mass per half-cycle against confinement, sway (case mean ± sd).

Method 2 is not consistent even between repeat runs of the same case. Table 13 gives two examples in which repeat runs disagree on whether the second half-cycle has a smaller or a larger added mass than the first. In sway case 10 this depends on the release amplitude, whereas in yaw case 3 the result changes

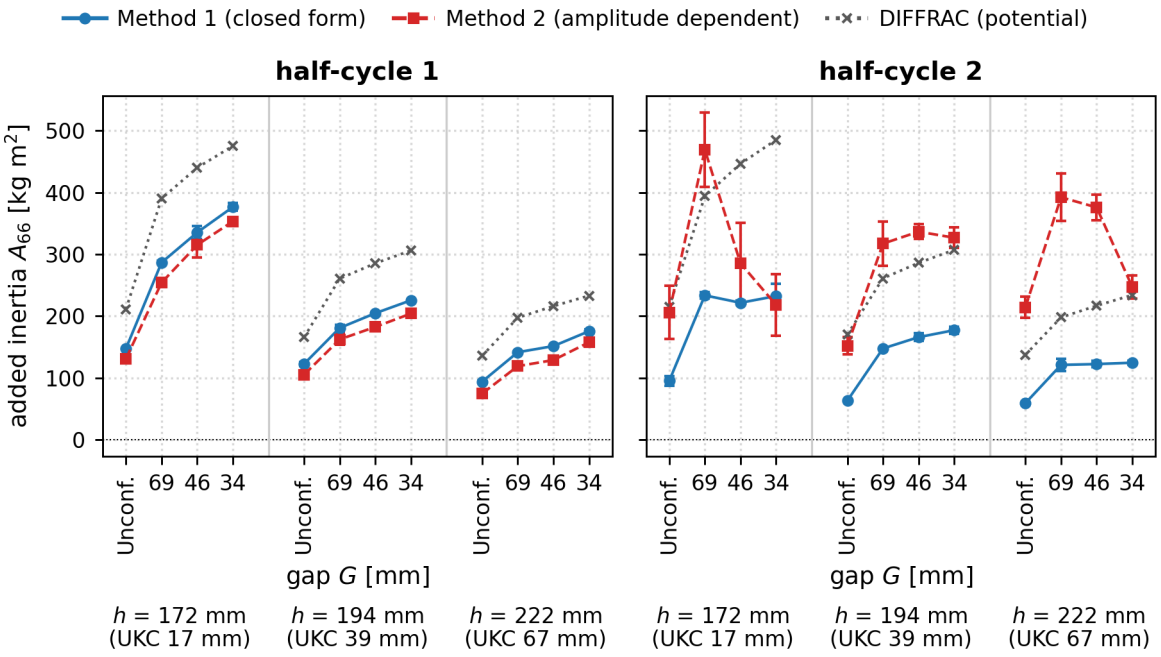

Figure 27: Added inertia per half-cycle against confinement, yaw (case mean ± sd).

although the release amplitude is the same in all runs.

Table 13: Repeat runs in which Method 2's change from half-cycle 1 to half-cycle 2 changes sign.

Case	Run	$a_{m,1}$	$A_{M2,1}$	$A_{M2,2}$	sign($A_{M2,2} - A_{M2,1}$)
Sway 10	348	10.71 mm	325.0	303.8	−
	345	10.89 mm	372.9	280.2	−
	341	12.10 mm	328.5	501.0	+
	337	12.25 mm	376.4	470.1	+
	343	12.30 mm	345.9	508.6	+
Yaw 3	193	0.517°	337.4	212.5	−
	195	0.519°	310.8	303.2	−
	197	0.520°	296.8	340.1	+

This behavior follows from the formulation of Method 2. Both half-cycles share a single linear damping coefficient, and the state at the end of the first half-cycle forms the initial condition of the second. The added mass of the second half-cycle is then the only remaining free parameter to absorb the part of the measured decay that the model cannot reproduce. Its value therefore reflects the fitting compromise rather than the hydrodynamic added mass.

The added mass of Method 1 is not exact either. The closed-form expression relates the added mass to the undamped natural frequency of the system, whereas the measured half period corresponds to the damped oscillation. Since damping lengthens the period, treating the measured half period as undamped overestimates the added mass. This error increases with the damping ratio and is therefore largest for the most confined cases (Section 5.1.6). The added mass of the second half-cycle is not used further. Method 2 gives no consistent value for it, and Method 1 gives values far below the potential added mass

that the present data cannot explain.

6.1.2 Total Damping and Fit Quality

Table 14 lists for each case the total damping B_1 obtained with the two methods, together with the cost J and the RMSE of the fits (Equation 22), as means over the repeat runs. The cost is the total error of the fit and grows with the length of the fit window. The RMSE is the typical error per sample, in millimeters or degrees, and can therefore be compared between cases.

Table 14: Total damping B_1, cost J and RMSE of the fits of Method 1 (M1) and Method 2 (M2), as means over the repeat runs of each case.

	Sway						**Yaw**					
	B_1 [N s/m]		J [mm^2]		RMSE [mm]		B_1 [N m s/rad]		J [deg^2]		RMSE [deg]	
Case	M1	M2	M1	M2	M1	M2	M1	M2	M1	M2	M1	M2
1	166.1	168.2	78.8	70.6	0.203	0.193	98.6	96.0	0.78	0.20	0.032	0.016
2	242.3	247.1	71.2	98.7	0.179	0.211	132.3	130.4	1.43	0.31	0.038	0.018
3	251.3	257.6	83.7	111.5	0.188	0.217	158.4	160.5	0.42	0.16	0.020	0.013
4	284.6	285.6	166.2	191.1	0.262	0.281	177.7	182.8	0.22	0.14	0.014	0.011
5	131.2	132.9	318.8	160.1	0.434	0.310	93.0	92.7	0.59	0.18	0.029	0.016
6	–	–	–	–	–	–	101.6	96.4	1.34	0.27	0.040	0.018
7	155.9	157.7	213.6	156.0	0.336	0.287	109.3	105.8	1.15	0.25	0.037	0.017
8	171.9	171.5	173.0	135.4	0.299	0.264	117.2	115.0	0.96	0.23	0.033	0.016
9	100.8	100.3	666.6	225.7	0.652	0.383	73.3	69.0	1.33	0.28	0.045	0.021
10	113.9	113.2	734.1	244.4	0.650	0.382	76.6	65.4	3.19	0.44	0.064	0.024
11	126.0	127.1	376.5	195.9	0.476	0.345	84.6	75.3	2.34	0.37	0.055	0.022
12	148.8	148.9	187.2	136.9	0.323	0.279	102.5	100.4	0.88	0.25	0.033	0.018

The linear damping coefficients B_1 obtained with the two methods are close. They differ by at most 3 % in sway and 15 % in yaw. In yaw, the largest differences occur in cases 10 and 11 (h = 222 mm), where Method 2 also yields the largest added mass of the second half-cycle relative to the potential value. In these cases, part of the fitting compromise described in Section 6.1.1 is absorbed by B_1.

Method 2 reproduces the measured decay more closely than Method 1, with a lower cost and RMSE in eight of the eleven sway cases and in all yaw cases. The RMSE of Method 1 is 0.18 to 0.65 mm in sway and 0.014 to 0.064° in yaw, and that of Method 2 is 0.19 to 0.38 mm and 0.011 to 0.024°. The difference is among the largest in sway case 9 and yaw case 10, which are shown in Figure 28. In these cases the cost of Method 1 is about three times (667 against 226 mm^2) and seven times (3.19 against 0.44 deg^2) that of Method 2. The second half-cycle decays more strongly than the model with a single linear damping coefficient can describe. Method 2 absorbs this with a larger added mass of the second half-cycle, and this has little effect on B_1. Method 1 cannot do this, because its added mass follows from the measured half period, so the difference remains in its cost. Neither method therefore describes the second half-cycle completely.

For these reasons, only Method 1 was used to derive the viscous damping. The total damping differs little between the two methods, so the choice has a limited influence on it. Both methods are uncertain in the added mass, especially in the second half-cycle, but Method 1 is the more consistent of the two. Its added mass is fixed by the measured half periods, whereas in Method 2 the added mass of the second half-cycle varies between repeat runs and trades off against B_1. The measured decays and the fits of

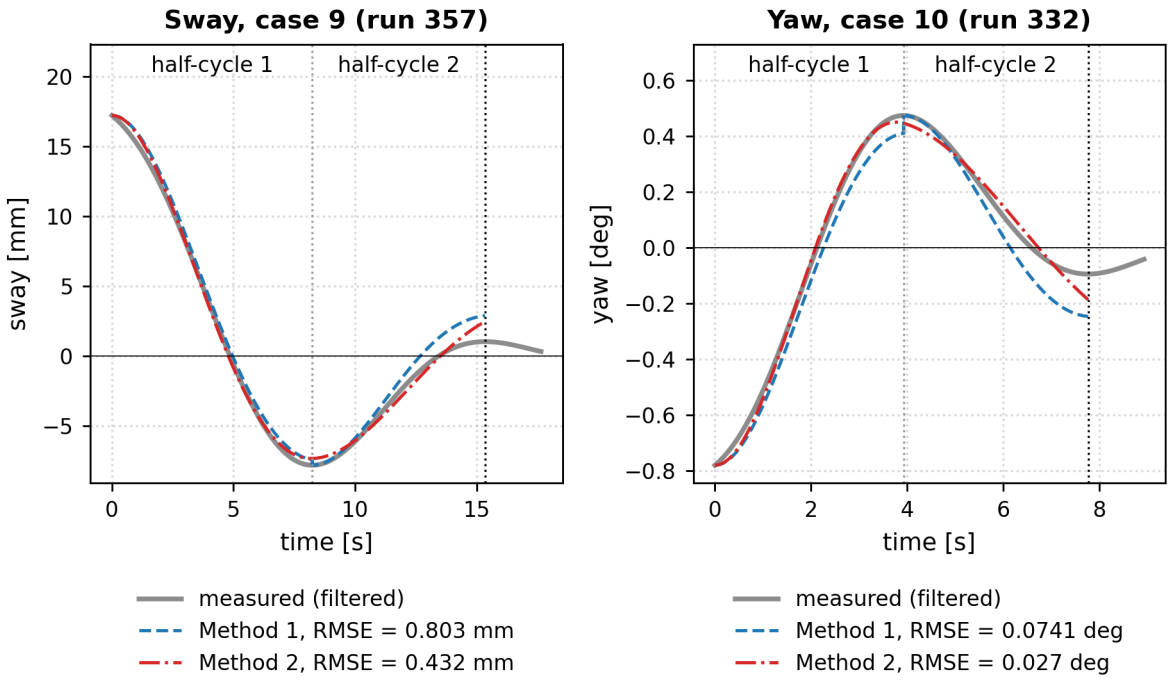

Figure 28: Measured decay and the fits of both methods: sway case 9 (run 357) and yaw case 10 (run 332). Method 1 restarts each half-cycles at the measured turning point.

Method 1 for all cases, averaged over the repeat runs, are shown in Appendix C.1 together with the RMSE of the fits. The viscous damping of Method 1 is presented in Section 6.2.

6.2 Viscous Damping

The damping presented in this section is obtained with Method 1, with the quadratic damping coefficient set to zero (Section 5.1.7). The linear damping coefficient $B_{1,kj}$ therefore represents the total damping of the moored model, denoted $B^{\text{total}}_{1,kj}$ in the following. It is decomposed into a potential, a pulley and a viscous part according to Equation 16. The potential damping from DIFFRAC (Table 10) is at most 0.04 N s/m in sway and 0.25 N m s/rad in yaw, and is therefore negligible at the low frequencies of the decay tests. The pulley damping is the same for all cases, 9.1 N s/m in sway and 18.2 N m s/rad in yaw (Section 5.2).

Table 15 lists for each case the mean total damping $B^{\text{total}}_{1,kj}$, its standard deviation between the repeat runs, the viscous damping $B^{\text{viscous}}_{1,kj}$ and the viscous part of the total damping.

The viscous damping clearly dominates the total damping. It accounts for 91 to 97 % of the total in sway and for 75 to 90 % in yaw. The lower share in yaw is mainly due to the pulley damping, which forms a larger part of the total damping in yaw (10 to 25 %) than in sway (3 to 9 %).

The repeat runs agree well. The standard deviation between the runs of a case is at most 8.6 N s/m in sway and 8.7 N m s/rad in yaw, which is below 7 % of the mean in every case. The uncertainty of the pulley damping is smaller than this scatter and the same for all cases, so it does not affect the comparison between cases.

The viscous damping depends strongly on the confinement, in both degrees of freedom. The effect of the UKC is already visible in the unconfined cases, without the quay wall. As the UKC decreases

Table 15: Viscous damping per case (Method 1), obtained from the total damping of Table 14 by subtracting the potential and the pulley damping. sd: standard deviation of the total damping between repeat runs.

	Sway			**Yaw**		
Case	$B^{\text{viscous}}_{1,22}$ [N s/m]	sd	$B^{\text{viscous}}/B^{\text{total}}$ [%]	$B^{\text{viscous}}_{1,66}$ [N m s/rad]	sd	$B^{\text{viscous}}/B^{\text{total}}$ [%]
1	157.0	4.2	95	80.3	5.2	82
2	233.2	3.1	96	113.8	3.3	86
3	242.2	1.7	96	139.9	8.7	88
4	275.4	8.6	97	159.3	7.0	90
5	122.1	4.0	93	74.8	2.0	80
6	–	–	–	83.2	1.7	82
7	146.8	2.6	94	90.9	2.2	83
8	162.8	2.4	95	98.8	2.3	84
9	91.7	3.8	91	55.0	1.5	75
10	104.8	6.7	92	58.3	5.0	76
11	116.9	5.2	93	66.3	1.1	78
12	139.6	4.5	94	84.2	3.1	82

from 67 to 39 and 17 mm, the viscous damping increases from 91.7 to 122.1 and 157.0 N s/m in sway and from 55.0 to 74.8 and 80.3 N m s/rad in yaw. The reduced keel clearance alone thus has a significant effect on the viscous damping. The same trend is found when the quay wall is present. At the smallest gap, the viscous damping increases from 139.6 to 162.8 and 275.4 N s/m in sway and from 84.2 to 98.8 and 159.3 N m s/rad in yaw as the UKC decreases.

The gap has a similar effect. At each water depth, the viscous damping increases as the gap decreases. At $h = 172$ mm it increases from 157.0 N s/m in the unconfined case to 275.4 N s/m at $G = 34$ mm in sway, and from 80.3 to 159.3 N m s/rad in yaw. In sway, most of this increase already occurs when the quay wall is placed at the largest gap of 69 mm (233.2 N s/m). The effect of the gap is smaller at a larger UKC. At $h = 222$ mm, the same reduction of the gap increases the viscous damping only from 91.7 to 139.6 N s/m in sway and from 55.0 to 84.2 N m s/rad in yaw. The highest damping therefore occurs when the model is confined in both directions, with a small UKC as well as a small gap. This dependence on confinement is analyzed in dimensionless form in Section 6.3.

6.3 Normalized added mass and damping

To allow a comparison between the cases, the two degrees of freedom and other studies, the added mass and the viscous damping were made dimensionless according to Equation 31 (Section 5.4). The added mass is that of the first half-cycle from Method 1 and the viscous damping is that of Section 6.2. The confinement is expressed by the ratio of the draft to the water depth, T/h, and the ratio of the gap to the beam, G/B. Table 16 lists the coefficients of all cases, and Figures 29 and 30 show them against G/B and T/h. Sway case 6 ($T/h = 0.80$, $G/B = 0.160$) is not included, so in the sway panels against the water depth the line for $G/B = 0.160$ connects $T/h = 0.70$ and 0.90 directly and has no value at $T/h = 0.80$. The comparison with other studies follows in Chapter 7.

Table 16: Normalized added mass of the first half-cycle and normalized viscous damping per case.

			Sway		Yaw	
Case	T/h	G/B	a_{22}	b_{22}^{viscous}	a_{66}	b_{66}^{viscous}
1	0.90	–	3.65	0.461	0.113	0.0323
2	0.90	0.160	5.84	0.684	0.220	0.0458
3	0.90	0.107	6.57	0.711	0.257	0.0563
4	0.90	0.079	7.04	0.809	0.289	0.0641
5	0.80	–	2.47	0.358	0.094	0.0301
6	0.80	0.160	–	–	0.139	0.0335
7	0.80	0.107	3.41	0.431	0.157	0.0366
8	0.80	0.079	3.77	0.478	0.173	0.0398
9	0.70	–	1.78	0.269	0.072	0.0222
10	0.70	0.160	2.15	0.308	0.109	0.0235
11	0.70	0.107	2.32	0.343	0.116	0.0267
12	0.70	0.079	2.77	0.410	0.135	0.0339

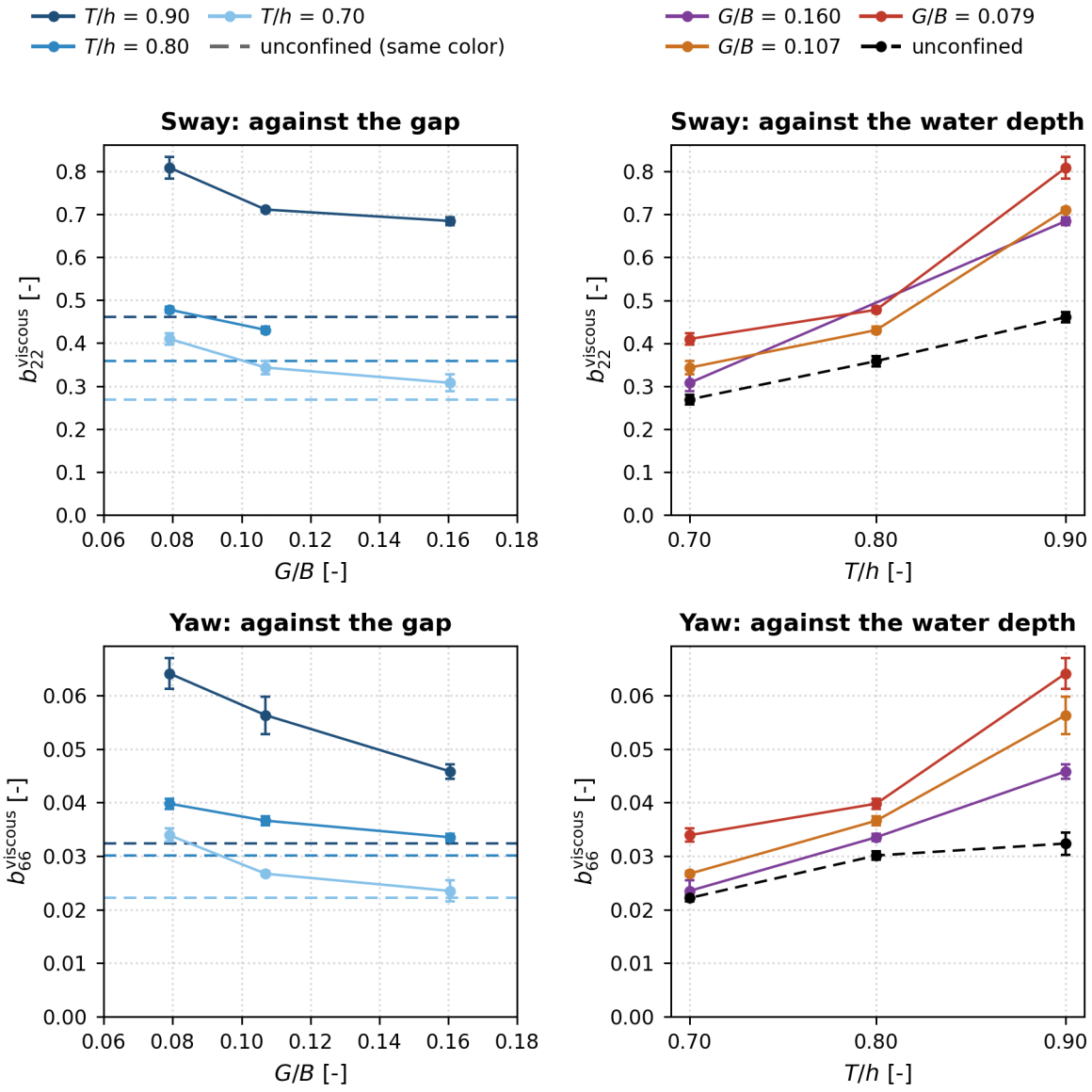

Figure 29: Normalized viscous damping against the gap (left) and the water depth (right), sway (top) and yaw (bottom). Dashed lines: unconfined cases.

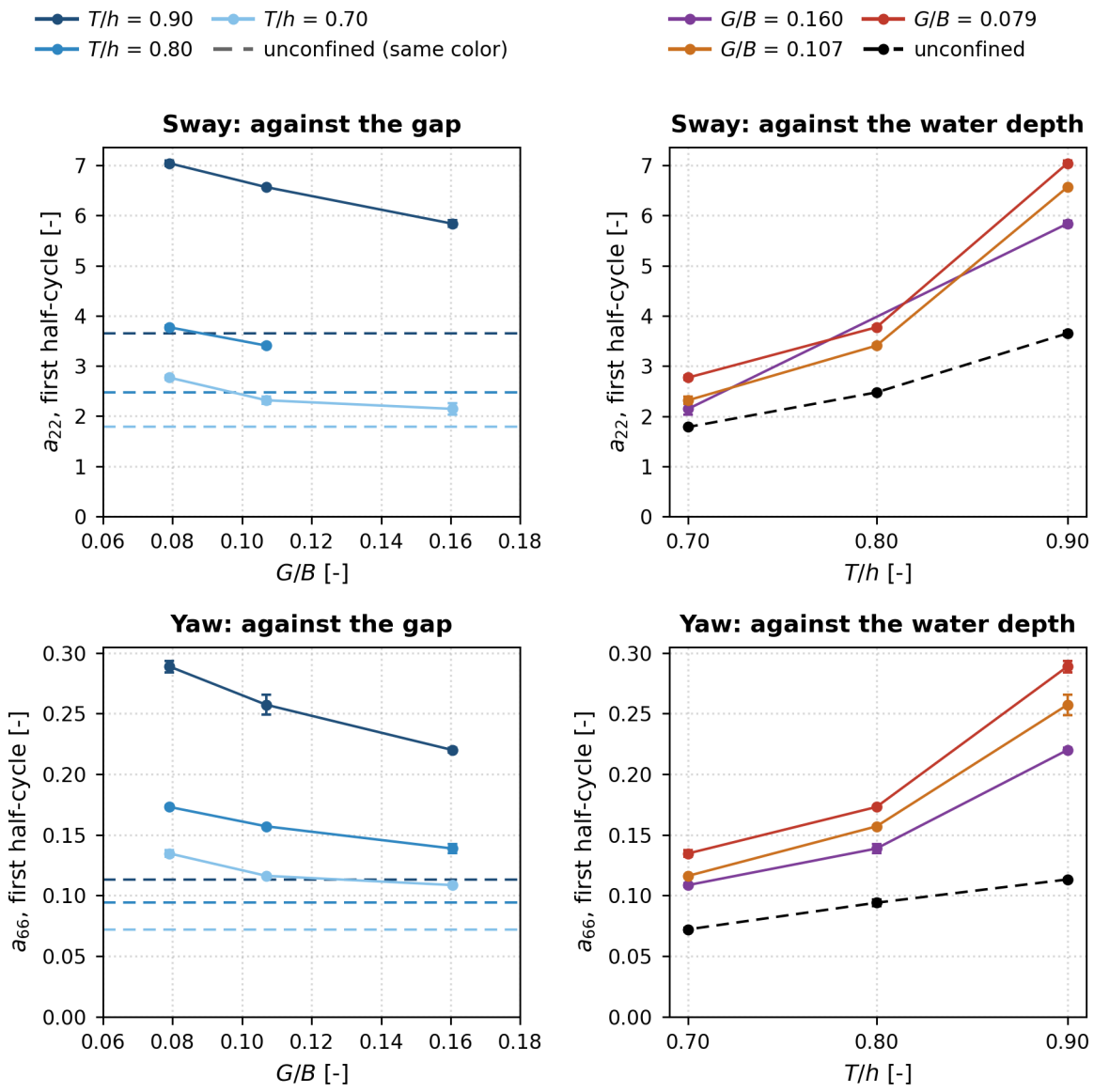

Figure 30: Normalized added mass of the first half-cycle against the gap (left) and the water depth (right), sway (top) and yaw (bottom). Dashed lines: unconfined cases.

6.4 Sway Case 6

Sway case 6 (h = 194 mm, G = 69 mm) deviates from all other cases and is therefore excluded from the results of this chapter and from the discussion. Its second half period (6.93 s) is shorter than that of the unconfined case at the same water depth (7.33 s), whereas confinement lengthens the half period in all other cases (Table 8). As a result, the added mass of the second half-cycle is biased in both methods: Method 1 gives 170 kg, below the unconfined value of 211 kg, and Method 2 gives approximately zero. The total damping of 185.2 N s/m exceeds that of cases 7 and 8 (155.9 and 171.9 N s/m), although these have a smaller gap. It is also the only case at this water depth in which the quadratic damping was positive with B_2 free (Section 5.1.7).

The repeat runs agree, so the deviation is not random, but a systematic error during these runs would affect all of them alike. A local difference in the bottom of the flume is unlikely, because the other cases with the same gap are normal and the yaw tests at the same water depth and gap, carried out

directly afterwards, show no such deviation. The cause could not be identified with the available data, and repeating this case is recommended.

7

Discussion

7.1 Effect of confinement on the viscous damping

The viscous damping increased with both a smaller UKC and a smaller gap (Sections 6.2 and 6.3). A plausible explanation lies in the flow around the hull. When the model moves sideways, the displaced water has to pass under the keel and, near the quay wall, through the gap. A smaller UKC or gap forces this flow through a narrower passage, which increases its velocity and the flow separation at the bilges, the mechanism also described by Buchner and de Boer [2].

The effect of the UKC was already large without the quay wall. Damping values obtained in deep or unconfined water therefore underestimate the damping of a vessel at a quay with a small UKC, and the confinement should be taken into account when predicting its low-frequency motions.

7.2 Comparison with Literature

De Boer and Buchner [2] measured the equivalent linear damping of an LNG carrier (L = 274 m, B = 44.2 m, T = 11.0 m) moored alongside a gravity based structure, at T/h = 0.73 and 0.44 and G/B = 0.068 to 0.204. Relative to the beam, their gaps cover the range of this study (G/B = 0.079 to 0.160), whereas only their shallower water depth lies within the range of this study (T/h = 0.70 to 0.90). Two units in their tables were corrected first, since they do not match the dimensions of the ship and the mooring. The damping is given in N instead of kN, and the yaw stiffness, inertia and damping are given per degree instead of per radian. With these corrections, their values were normalized in the same way as in this study, with a displacement of 99 548 t [52], and used for the comparison. They are taken as viscous damping, since the potential damping is negligible at these frequencies and no damping of their mooring is reported.

Figure 31 shows that, at a comparable water depth, the damping of this study is two to four times larger in sway and seven to twelve times larger in yaw. Both studies find more damping in shallower water, but De Boer and Buchner find no consistent effect of the gap.

These values cannot be compared directly. Both studies applied Froude scaling, but at different scales, 1:87 here and 1:50 for De Boer and Buchner, so the Reynolds numbers of the two models differ. That of De Boer and Buchner could not be determined, since their paper does not report the velocities or the amplitudes of the sway and yaw decays. The Reynolds number governs the boundary layer and the flow separation, which cause the viscous damping, so the damping is expected to depend on it.

Other differences add to this and cannot be separated from it. The hull shape differs: a box with sharp edges, which promote flow separation, against a ship with rounded bilges and fine ends. The decays of De Boer and Buchner are lightly damped, at 4.1 to 7.4 % of the critical damping in sway and 2.2 to 4.5 % in yaw, against 24 to 43 % and 16 to 31 % for the viscous damping of this study, calculated with the added mass of the first half-cycle. Their dimensionless frequency is considerably higher, so that many oscillations were available, whereas only two half-cycles could be used here. Their structure is of finite

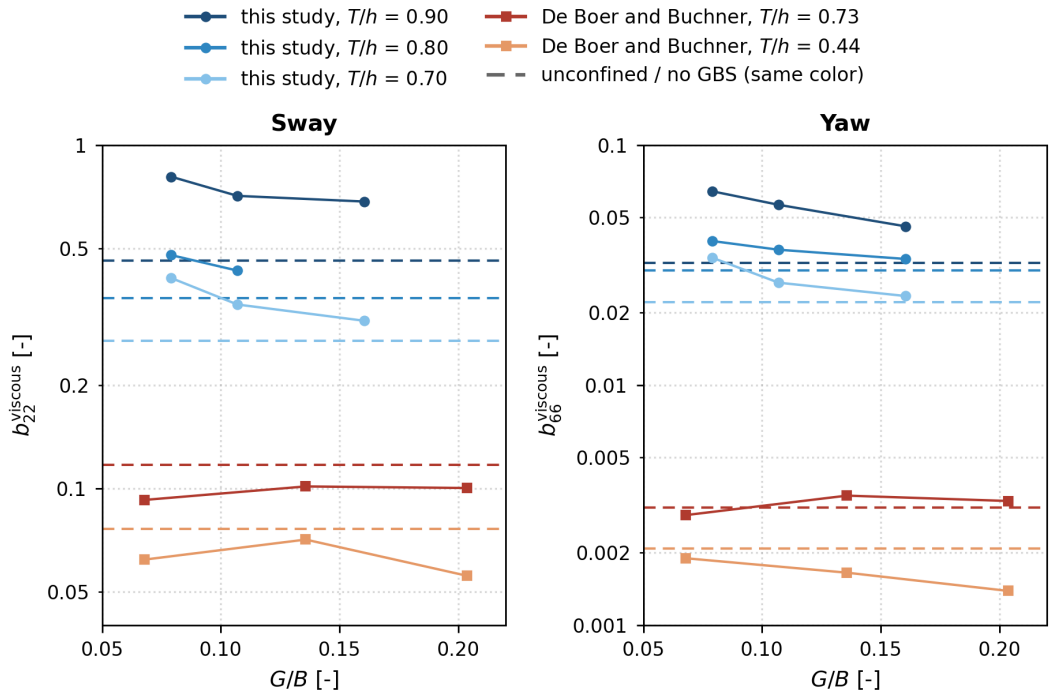

Figure 31: Normalized viscous damping against the gap: this study and De Boer and Buchner [2]. Dashed lines: unconfined cases and tests without the structure. Logarithmic vertical axis.

length, so water can flow around its ends, which probably weakens the effect of the gap, and part of their tests was carried out in a different basin.

The comparison therefore shows that damping coefficients cannot be transferred directly from one vessel and test configuration to another. The same question arises for the transfer of this study to full scale. If two model tests at different scales cannot be compared, the damping measured here cannot simply be scaled up either, since the Reynolds number at full scale is much higher. The scale effects that limit this transfer are discussed next.

7.3 Scale effects and transfer to full scale

The tests were scaled according to Froude, which does not preserve the Reynolds number. At a scale of 1:87, the Reynolds number of the model is about 700 times smaller than at full scale. The boundary layer along the hull is therefore relatively thicker in the model, and the skin friction is overestimated.

In ship resistance tests, the ITTC corrects for this scale effect [50]. The skin friction of the model is calculated with the ITTC-1957 friction line, which gives the friction of a flat plate as a function of the Reynolds number. This friction is subtracted from the measured resistance, the remainder is scaled according to Froude, and the skin friction at the Reynolds number of the ship is added again. The method was developed for a model towed at a constant speed through open, deep water, where the water passes the hull at the speed of the model and the boundary layer is turbulent. The conditions of this study are different. The model oscillated at a low velocity, so that the boundary layer was laminar and changed direction every half period. In addition, the displaced water was forced under the keel and through the gap to the quay wall. The velocity of this flow determines the skin friction, but it was not measured, and it is expected to be much higher than the velocity of the model, most of all at the smallest UKC. At

this UKC, the boundary layers of the hull and of the flume bottom also fill most of the space under the keel. Finally, the decay tests give a single damping value per case, which contains the skin friction and the damping caused by flow separation together. The skin friction could therefore not be calculated or separated, and the correction of the ITTC could not be applied.

The flow separates at the sharp bilges of the box, at the same location at model and at full scale. As in the original method of Froude [38], the damping caused by the separation is therefore assumed to follow Froude scaling. Under this assumption, only the skin friction is overestimated, and the viscous damping of this study is an upper limit for full scale. The difference is expected to be largest at the smallest UKC.

7.4 Added Mass

The added mass of the first half-cycle of Method 1 is lower than the potential added mass from DIFFRAC in every case, 0.81 to 0.94 times in sway and 0.69 to 0.79 times in yaw (Section 6.1.1). This also holds for the unconfined cases and for the series with the largest UKC, which lies within the range for which DIFFRAC has been validated (Section 5.3). The added mass of the experiments is not exact, however. It follows from the undamped expression of Equation 25 with a constant mooring stiffness. Damping lengthens the half period, so the expression overestimates the added mass and the actual difference with DIFFRAC is larger. The added mass of this study should therefore be seen as an indication, and the difference needs further investigation.

The added mass of the second half-cycle is lower still, 0.36 to 0.48 times the DIFFRAC value in sway and 0.37 to 0.61 in yaw, so the added mass depends on the amplitude. The half period also shortens during the decay (Section 5.1.5), so the decay covers a range of frequencies instead of a single one. This suggests the Cummins equation (Equation 6), which describes the memory of the radiated waves with a retardation function. It is not expected to change the results here. Over the frequency range of the decays, DIFFRAC gives an added mass that changes by less than 3 % and a potential damping below 0.3 % of B_1 (Section 5.3), so the memory effect is practically absent. The damping that dominates the decays is mainly viscous and cannot be part of the memory function. A fit of the Cummins equation was not made in this study, and it is suggested for future work to confirm this (Section 8.2).

DIFFRAC calculates the added mass for a quay wall at a fixed distance, whereas the gap changes as the model moves. In sway the release amplitude of 16 to 22 mm is 23 to 65 % of the gaps of 69 to 34 mm, and the second half-cycle still starts from 3.4 to 7.8 mm. In yaw one end of the model moves toward the quay while the other moves away. The gap becomes smaller on one side of the equilibrium position and larger on the other, and the potential added mass increases as the gap decreases (Table 10). The added mass of the model is therefore not constant during a half-cycle, and it can differ between half-cycles with different amplitudes. The same holds for sloshing in the gap and its piston mode, which also depend on the gap. None of these can be the cause of the lower added mass of the second half-cycle, however, since it is also found in the unconfined cases (0.36 to 0.46 in sway and 0.37 to 0.44 in yaw), which have no quay wall nearby. A smaller contribution to the differences between the confined cases cannot be excluded, but it cannot be separated from the other effects with the present data.

The springs and pulleys of the mooring can contribute. In the dry tests their period shortened below an amplitude of about 5 mm, by 3 to 9 % at 4 mm and 11 to 18 % at 2 mm (Section 5.2), as if they became stiffer. In sway the second half-cycle has a mean amplitude of 1.8 to 4.4 mm, against 10.5 to 13.4 mm for the first, and a stiffer mooring is read as a lower added mass. The shortening in the dry tests is smaller

than in the wet tests, so this explains only a part of it.

Viscous effects are another explanation, since the potential flow of DIFFRAC does not describe the boundary layers or the flow separation at the bilges. Studies of other bodies and motions indicate that such effects can make the added mass depend on the amplitude. In the free heave decay of a cylinder, Chen et al. [53] found an added mass a few percent above the potential value, slightly more in the first cycle than in later ones, and forced oscillation tests of heave plates, pontoons and floating wind turbine platforms show an added mass that increases with the amplitude [54]. These results concern other motions and bodies and are used here only to show that an amplitude dependence of viscous origin is possible. They do not explain the level found here, since in those studies the added mass is above the potential value, whereas here both half-cycles are below it.

De Boer and Buchner [2] also needed an additional mass and damping next to the diffraction results to reproduce their model tests, defined as the difference between the decay tests and the diffraction calculation. The paper does not report the values of this mass. In this study the difference is negative, and the present data cannot show how much of it is physical and how much is caused by the method. Forced oscillation tests at several amplitudes and frequencies, and measurements of the spring forces, the water level in the gap and the flow velocities, could separate these effects (Section 8.2). The main result of this study is therefore the damping rather than the added mass.

7.5 Limitations of the damping analysis

The decays were heavily damped, so that only two half-cycles could be used. As a result, the linear and the quadratic damping could not be separated, and the equivalent linear damping applies only to the amplitude range of these two half-cycles. At full scale, this range corresponds to sway motions of about 0.2 to 1.9 m and yaw motions of about 0.1 to 0.8°, which covers the motions of a vessel moored at a berth. A single damping coefficient also does not reproduce the second half-cycle equally well in all cases. In yaw, the second half-cycle decays more strongly than the fit (Appendix C.1), which indicates a relatively stronger damping at small amplitudes.

The smallest UKC was 17 mm. At this UKC, an error of a few millimeters in the water depth or the draft forms a considerable part of the UKC. The flume bottom was also not perfectly level, so the local UKC under the model may have differed from the nominal value. Since the damping increased strongly at small UKC, the cases at the smallest UKC are the most sensitive to these errors.

The pulley damping was measured in dry tests at a higher frequency than the decays and assumed constant. Its uncertainty affects yaw most, where it forms a larger part of the total damping. The behavior of the springs and pulleys at small amplitudes (Section 7.4) also affects the second half-cycle most and may contribute to its stronger decay in yaw.

8

Conclusions and Future Work

8.1 Conclusions

This thesis investigated the viscous damping of a vessel moored close to a quay wall, with moored decay tests in sway and yaw on a box-shaped model at a scale of 1:87. The tests covered three water depths and three gaps to the quay wall, together with an unconfined reference. The research questions are answered below.

How does the added mass change with lateral and vertical confinement? The added mass increases as the gap and the UKC decrease, in sway as well as in yaw, which follows the trend of the potential added mass from DIFFRAC. Its values are lower than the DIFFRAC values, 0.81 to 0.94 times in sway and 0.69 to 0.79 times in yaw in the first half-cycle, and the closed-form expression overestimates them, so the difference is larger still. The added mass also depends on the amplitude, since that of the second half-cycle is lower than that of the first in every case. The cause could not be determined, and the added mass of this study should be seen as an indication.

How does the viscous damping change with lateral and vertical confinement? The viscous damping increased with both a smaller UKC and a smaller gap. In normalized form, it increased in sway from 0.27 for the unconfined case at $T/h = 0.70$ to 0.81 at $T/h = 0.90$ and $G/B = 0.079$, and in yaw from 0.022 to 0.064. The effect of the UKC was already large without the quay wall. The viscous damping formed most of the total damping, 91 to 97 % in sway and 75 to 90 % in yaw.

How accurately can added mass and viscous damping be extracted from moored decay model tests? The damping can be extracted more accurately than the added mass. Within the tested amplitude range, it is repeatable, since the standard deviation of the total damping over the repeat runs was 1.7 to 8.6 N s/m in sway and 1.1 to 8.7 N m s/rad in yaw. It also depends little on the method, since the two methods gave a linear damping that differed by at most 3 % in sway and 15 % in yaw, and the fits of Method 1 reproduce the measured decays with a root mean square error of 0.18 to 0.65 mm in sway and 0.014 to 0.064° in yaw. This accuracy has limits, however. The heavy damping left only two half-cycles per decay, so the linear and the quadratic damping could not be separated and the result is an equivalent linear damping. The pulley damping adds an uncertainty, mainly in yaw. One sway case, at $h = 194$ mm and $G = 69$ mm, deviated from the trend of the other cases for a reason that could not be identified. Its repeat runs agreed with each other, so the deviation is not random, but it is unclear whether it is physical or caused by the test setup. The case was therefore excluded from the results (Section 6.4). The added mass is less accurate than the damping, since it follows from the measured half periods with an undamped expression, and neither method gives a reliable value for the second half-cycle.

How does the magnitude of the identified viscous damping compare to the damping typically assumed in current Dynamic Mooring Analysis practice? This can only be answered in part, since the magnitude at full scale remains to be determined. In dynamic mooring analyses, the viscous damping in sway and yaw is often neglected. At model scale, the viscous damping of this study corresponds to 24 to 43 % of

the critical damping in sway and 16 to 31 % in yaw, and these values are an upper limit for full scale. The tests also show that the viscous damping increases as the gap and the UKC decrease, so it depends on the confinement. If the damping at full scale is also larger than assumed, neglecting it is conservative. The values of this study should therefore first be translated to full scale.

Do the results of De Boer and Buchner align with the results of this study? Only the trends can be compared. Both studies find more damping in shallower water, but De Boer and Buchner find no consistent effect of the gap, whereas in this study the damping increased as the gap decreased. The magnitudes cannot be compared, since the two studies were carried out at different scales and therefore at different Reynolds numbers, on which the viscous damping depends. The hull form, the frequency of the decays and the length of the structure differ as well. Damping coefficients can therefore not be transferred directly from one vessel and test configuration to another.

With respect to the main objective, the viscous damping of a vessel moored close to a quay wall increases considerably as both the UKC and the gap decrease. With respect to the secondary objective, the viscous damping is significant at model scale. At the low natural frequencies of the tests, it forms most of the total damping, whereas in dynamic mooring analysis it is commonly assumed to be small or neglected. Whether this also holds at full scale, and how large the damping is there, remains to be determined.

8.2 Future Work

This study identified the viscous damping of a moored vessel at a quay from moored decay tests and showed that it increases with both a smaller gap and a smaller UKC. Two limitations frame the work that remains. The moored decay method leaves only two half-cycles of a heavily damped decay, and the added mass derived from them depends on the amplitude for reasons that could not be determined (Section 7.4). In addition, the results apply to model scale, and the scale effect on the viscous damping could not be corrected (Section 7.3). Future work follows these two lines, from the identification of the coefficients to their transfer to full scale.

The most direct improvement uses the existing setup. The damping and the stiffness of the springs and pulleys were measured in dry tests at a higher frequency than that of the decays (Section 5.2). Dry forced oscillation tests at the frequencies and amplitudes of the decays would identify them under the conditions that matter, including the stiffening at small amplitudes, and would improve the present results directly. The decays themselves contain a range of frequencies, so a fit of the Cummins equation to the existing data would confirm whether the memory of the radiated waves can indeed be neglected. Further decay tests would extend the results. Releasing the model from different amplitudes would show how the added mass of the first half-cycle depends on the amplitude. The present tests cannot show this, because the small amplitudes only occur after one half-cycle and cannot be separated from the effect of the earlier motion. Sway case 6 should be repeated, to establish whether its deviation is of physical origin or caused by the test setup, and the cruise ship of the original scope (Appendix D), which the same box represents at a scale of 75, would extend the results to a second type of vessel.

The decay tests would also be more informative with additional measurements. Measurements of the flow velocities in the gap and under the keel, of the water elevation in the gap and of the spring forces would show whether the flow separation, the sloshing or the piston mode of the gap, or the mooring contribute to the amplitude dependence of the added mass. The flow velocities would moreover give the

skin friction, which could not be separated from the damping caused by flow separation in this study (Section 7.3).

Forced oscillation tests can overcome the main limitation of the moored decay tests, the few oscillations that remain before the motion has died out. With the range of natural periods known from the decay tests, the model can be driven at these periods and at chosen amplitudes for as many cycles as needed, so that the added mass and the viscous damping are identified more accurately. The accuracy increases for three reasons. The force is measured directly, so the added mass and the damping do not have to be derived from the half periods of a heavily damped decay. The amplitude and the frequency are set independently, so the dependence of the coefficients on them can be determined and the quadratic damping can be separated from the linear damping. In addition, no mooring is needed, so the uncertainty of the pulleys does not occur. Since a single degree of freedom is imposed, realistic hull forms, such as those of container ships and cruise ships, can be tested as well, without the decoupling of sway and yaw that the symmetry of the box provided (Section 4.1.2).

The scale effect on the viscous damping remains the main limitation of this study (Section 7.3). Besides the flow measurements, two approaches can address it, and both are demanding. Computational fluid dynamics (CFD) could be applied at the Reynolds number of the full-scale vessel, and the measurements of this study could serve as validation data, but the flow separation at the sharp edges in a narrow gap is difficult to model and the calculations are expensive. Tests of the same configuration at a different scale would show directly how the damping changes with the Reynolds number, but they require a new model and test setup and are expensive as well.

Finally, once the viscous damping has been determined at full scale, its dependence on the UKC and the gap could be incorporated into dynamic mooring analyses. This would allow its effect on the motions of a vessel at the berth and on the mooring line forces to be quantified, and the effect of confinement to be accounted for in the design of moorings.

AI Statement

During the preparation of this thesis, the author used Claude (`https://claude.ai`) in order to refine the language and to assist with programming and debugging. After using this tool, the author reviewed and edited the content as needed and takes full responsibility for the content of this thesis.

References

[1] International Institute of Marine Surveying. Ship news. https://www.iims.org.uk/tag/ship-news/page/30/. Accessed: 2026-02-27.

[2] Gerrit De Boer and Bas Buchner. Viscous damping of vessels moored in close proximity of another object. In *Proceedings of the International Offshore and Polar Engineering Conference (ISOPE)*, Seoul, South Korea, 2005. Presented at ISOPE 2005.

[3] PIANC MarCom WG 235. Ship dimensions and data for design of marine infrastructure, 2022. URL https://www.pianc.org/publication/ship-dimensions-and-data-for-design-of-marine-infrastructure/.

[4] UNCTAD. *Review of Maritime Transport 2025: Staying the Course in Turbulent Waters*. United Nations, 2025. ISBN 978-92-1-154528-9. URL https://unctad.org/publication/review-maritime-transport-2025. UNCTAD/RMT/2025.

[5] Martin Stopford. *Maritime Economics*. Routledge, 3 edition, 2009. ISBN 978-0-415-27558-3. doi: 10.4324/9780203891742. URL https://doi.org/10.4324/9780203891742.

[6] Nam-Kyu Park and Sang-Beom Suh. Tendency toward mega-ships and policy measures for strengthening port competitiveness. *Journal of Marine Science and Engineering*, 7(6):186, 2019. doi: 10.3390/jmse7060186. URL https://doi.org/10.3390/jmse7060186.

[7] Enrico Musso and Anna Sciomachen. Impact of megaships on the performance of port container terminals. *Maritime Economics & Logistics*, 22(3):432–445, 2020. doi: 10.1057/s41278-019-00120-y.

[8] PIANC MarCom WG 152. Guidelines for cruise terminals, 2016.

[9] Jean-Paul Rodrigue. *The Geography of Transport Systems*. Routledge, 6 edition, 2024. ISBN 9781003343196. doi: 10.4324/9781003343196. URL https://doi.org/10.4324/9781003343196.

[10] Apostolos Papanikolau, Rainer Hamann, Byung Suk Lee, Christian Mains, Odd Olufsen, Erik Tvedt, Dracos Vassalos, and George Zaraphonitis. Goalds: Goal based damage stability of passenger ships. In *SNAME Maritime Convention*. The Society of Naval Architects and Marine Engineers, 2013. doi: 10.5957/SMC-2013-T04. URL https://doi.org/10.5957/SMC-2013-T04. Paper No. SNAME-SMC-2013-T04.

[11] PIANC MarCom Working Group 211. Pianc fender guidelines 2024: Guidelines for the design, manufacturing and testing of fender systems. Technical Report Report No. 211, PIANC, The World Association for Waterborne Transport Infrastructure, Brussels, Belgium, March 2024.

[12] César Ducruet, Hidekazu Itoh, and Olaf Merk. Time efficiency at world container ports. Technical Report Discussion Paper 2014-08, International Transport Forum and Organisation for Economic Co-operation and Development, 2014.

[13] Oil Companies International Marine Forum (OCIMF). Mooring equipment guidelines (meg4), 4th edition. Technical report, OCIMF, London, United Kingdom, 2018. Published June 2018.

[14] Daniel Seong Hyeok Moon and Jong-Kyun Woo. The impact of port operations on efficient ship operation from both economic and environmental perspectives. *Maritime Policy & Management*, 41(5):444–461, 2014. doi: 10.1080/03088839.2014.931607.

[15] PIANC MarCom Working Group 186. Mooring of Large Ships at Quay Walls. MarCom Working Group Report 186, PIANC, The World Association for Waterborne Transport Infrastructure, Brussels, Belgium, January 2025.

[16] PIANC MarCom Working Group 212. Criteria for Acceptable Movement of Ships at Berths. MarCom Working Group Report 212, PIANC, The World Association for Waterborne Transport Infrastructure, Brussels, Belgium, June 2023.

[17] Coen Eggermont and Alex Van Deyzen. To improve the orientation of a jetty exposed to swell and current to minimise operational downtime. In *Proceedings of the ASME 2023 42nd International Conference on Ocean, Offshore and Arctic Engineering (OMAE2023)*, number OMAE2023-101382, Melbourne, Australia, June 2023.

[18] A.F.J. Van Deyzen, L. Nguyen, and J. Van De Sande. The difference between a static and dynamic mooring analysis for large container ships in wind. In *35th PIANC World Congress*, Cape Town, South Africa, April 2024.

[19] J. N. Newman. Second-order, slowly-varying forces on vessels in irregular waves. In *Proceedings of the International Symposium on the Dynamics of Marine Vehicles and Structures in Waves*, 1974.

[20] O. M. Faltinsen and F. C. Michelsen. Motions of large structures in waves at zero froude numbers. Technical Report Publication No. 90, Det Norske Veritas, Oslo, Norway, September 1975.

[21] J. A. Pinkster. Mean and low frequency wave drifting forces on floating structures. *Ocean Engineering*, 6(6):593–615, 1979. doi: 10.1016/0029-8018(79)90010-6.

[22] J. E. W. Wichers and M. F. van Sluijs. The influence of waves on the low-frequency hydrodynamic coefficients of moored vessels. In *Proceedings of the Offshore Technology Conference*, Houston, Texas, April 1979. Offshore Technology Conference. doi: 10.4043/3625-MS. URL `https://doi.org/10.4043/3625-MS`.

[23] J. E. W. Wichers and R. H. M. Huijsmans. On the low-frequency hydrodynamic damping forces acting on offshore moored vessels. In *Offshore Technology Conference*, OTC 4813, Houston, Texas, May 1984.

[24] Aad J. Hermans. Low-frequency second-order wave-drift forces and damping. *Journal of Engineering Mathematics*, 35:181–198, February 1999. doi: 10.1023/A:1004323229079.

[25] J. E. W. Wichers. *A simulation model for a single point moored tanker*. Phd thesis, Delft University of Technology, Delft, The Netherlands, 1988. URL `https://resolver.tudelft.nl/uuid:efd9dd4e-da6a-48b7-9349-4a7541e89456`. TU Delft Repository. Sometimes cited with a 1987 publication date in external catalogs.

[26] Z. X. Zhou, Edmond Y. M. Lo, and S. K. Tan. Effect of shallow and narrow water on added mass of cylinders with various cross-sectional shapes. *Ocean Engineering*, 32:1199–1215, 2005.

[27] Y. Drobyshevski. Hydrodynamic coefficients of a two-dimensional, truncated rectangular floating structure in shallow water. *Ocean Engineering*, 31:305–341, 2004.

[28] L. Xiong et al. Motion responses of a moored barge in shallow water. *Ocean Engineering*, 2015. Uses damping ratio from free-decay model tests to account for viscous damping.

[29] Tahsin Tezdogan and Atilla Incecik. Cfd simulations of vertical ship motions in shallow water. In *Proceedings of the International Conference on Maritime Technology (ICMT 2016)*, Harbin, China, 2016.

[30] B. Molin. On the piston and sloshing modes in moonpools. *Journal of Fluid Mechanics*, 430:27–50, 2001.

[31] R. H. M. Huijsmans, J. A. Pinkster, and J. Wildenhuijs. Diffraction and radiation of waves around side-by-side moored vessels. *11th International Offshore and Polar Engineering Conference*, 2001.

[32] J. N. Newman. Wave effects on multiple bodies. *Hydrodynamics of Ocean Engineering*, 2003.

[33] X. B. Chen. Hydrodynamics in offshore and naval applications. *Keynote lecture, 6th International Conference on Hydrodynamics*, 2005.

[34] Willem van der Molen. *Behaviour of Moored Ships in Harbours*. Dissertation (tu delft), Delft University of Technology, Delft, The Netherlands, 2006.

[35] Bas Buchner, Adri van Dijk, and Jaap de Wilde. Numerical multiple-body simulations of side-by-side mooring to an FPSO. In *Proceedings of the Eleventh (2001) International Offshore and Polar Engineering Conference*, pages 343–353, Stavanger, Norway, June 2001. International Society of Offshore and Polar Engineers. ISBN 1-880653-51-6.

[36] Bas Buchner, G. E. Loots, G. Z. Forristall, and E. J. van Iperen. Hydrodynamic aspects of gravity based structures in shallow water. In *Offshore Technology Conference (OTC 16716)*, Houston, Texas, 2004. Offshore Technology Conference.

[37] O. M. Faltinsen. *Sea Loads on Ships and Offshore Structures*. Cambridge University Press, 1990.

[38] J. M. J. Journée and W. W. Massie. *Offshore Hydromechanics*. Delft University of Technology, Delft, The Netherlands, 2nd edition, 2008.

[39] H. K. Versteeg and W. Malalasekera. *An Introduction to Computational Fluid Dynamics: The Finite Volume Method*. Pearson Education Limited, Harlow, England, 2nd edition, 2007. ISBN 978-0-13-127498-3.

[40] H. Asmuth, P. Schmitt, B. Elsaesser, and A. Henry. Determination of non-linear damping coefficients of bottom-hinged oscillating wave surge converters using numerical free decay tests. In Guedes Soares, editor, *Renewable Energies Offshore*, pages 507–513. Taylor & Francis Group, London, 2015. ISBN 978-1-138-02871-5.

[41] Norbert Bulten and Petra Stoltenkamp. Full scale cfd: the end of the froude-reynolds battle. In *Fifth International Symposium on Marine Propulsion (SMP'17)*, Espoo, Finland, June 2017.

[42] Momchil Terziev, Tahsin Tezdogan, and Atilla Incecik. Scale effects and full-scale ship hydrodynamics: A review. *Ocean Engineering*, 245:110496, 2022. doi: 10.1016/j.oceaneng.2021.110496.

[43] Alessio Pistidda, Harald Ottens, and Richard Zoontjes. Using CFD to assess low frequency damping. In *Proceedings of the ASME 2012 31st International Conference on Ocean, Offshore and Arctic Engineering (OMAE 2012)*, pages 657–665, Rio de Janeiro, Brazil, July 2012. American Society of Mechanical Engineers. doi: 10.1115/OMAE2012-83326. URL https://doi.org/10.1115/OMAE2012-83326. Paper No. OMAE2012-83326.

[44] Frédérick Jaouën, Arjen Koop, and Lucas Vatinel. URANS predictions of low-frequency damping of a LNGC. In *Proceedings of the ASME 2019 38th International Conference on Ocean, Offshore and Arctic Engineering (OMAE 2019)*, Glasgow, Scotland, UK, June 2019. American Society of Mechanical Engineers. doi: 10.1115/OMAE2019-95171. URL https://doi.org/10.1115/OMAE2019-95171. Paper No. OMAE2019-95171.

[45] Arjen Koop, Sebastien Loubeyre, Kai Yu, Haihua Xu, Yingying Zheng, and Zhenjia Huang. Development and verification of modelling practice for CFD calculations to obtain hydrodynamic damping of offshore vessels. In *Proceedings of the ASME 2022 41st International Conference on Ocean, Offshore and Arctic Engineering (OMAE 2022)*, Hamburg, Germany, June 2022. American Society of Mechanical Engineers. doi: 10.1115/OMAE2022-78981. URL https://doi.org/10.1115/OMAE2022-78981. Paper No. OMAE2022-78981.

[46] Zongyu Jiang, Fang Li, Sasan Tavakoli, Pentti Kujala, Mikko Suominen, and Spyros Hirdaris. A viscous investigation on the hydrodynamic coefficients and wave loads under the interaction of side-by-side cylinders in regular waves. *Ocean Engineering*, 297:117156, 2024. doi: 10.1016/j.oceaneng.2024.117156.

[47] A. Stampoultzoglou. Determination of the nonlinear roll damping of a barge by means of viscous flow simulations: An advanced approach to compute roll damping characteristics with cfd. Master's thesis, Delft University of Technology, Delft, The Netherlands, September 2017.

[48] J. N. Newman. *Marine Hydrodynamics*. MIT Press, 2 edition, 2018.

[49] W. E. Cummins. The impulse response function and ship motions. Technical Report DTMB Report 1661, David Taylor Model Basin, Washington, DC, 1962.

[50] ITTC. Resistance test. ITTC – Recommended Procedures and Guidelines 7.5-02-02-01, Revision 05, International Towing Tank Conference, 2021.

[51] Polar mexico: Container vessel. In Richard Halfhide, editor, *Significant Ships of 2017*, pages 66–67. The Royal Institution of Naval Architects, London, 2018.

[52] Bas Buchner, Gerrit de Boer, and Jaap de Wilde. The interaction effects of mooring in close proximity of other structures. In *The Fourteenth International Offshore and Polar Engineering Conference (ISOPE)*, Toulon, France, 2004. International Society of Offshore and Polar Engineers.

[53] Hao Chen, Qianlong Xu, Xiaobo Zheng, Luke G. Bennetts, Bin Xie, Zhiliang Lin, Zaibin Lin, and Ye Li. Viscous effects on the added mass and damping forces during free heave decay of a floating cylinder with a hemispherical bottom. *European Journal of Mechanics - B/Fluids*, 98:8–20, 2023. doi: 10.1016/j.euromechflu.2022.11.002.

[54] Lulu Liu, Ian A. Milne, Hugh A. Wolgamot, Raúl Guanche, and Wenhua Zhao. Viscous added mass effects on the pitch motion prediction of a semi-submersible floating wind turbine. *Ocean Engineering*, 367:127869, 2026. doi: 10.1016/j.oceaneng.2026.127869.

A

Experiment

A.1 Additional Photographs of the Setup

This appendix collects photographs of the experimental setup that support the description given in Sections 4.6 and 4.8, so that the arrangement can be checked against the real components.



Figure 32: Overview of the assembled setup from above, showing the model with its backbone and the metal frame at each end, which slides across the flume on the aluminium profile.



Figure 33: One end of the model seen from above, showing the electromagnet, the bolt mounted on the backbone extender that engages it, the springs attached to the backbone, and the two pulleys that redirect them.

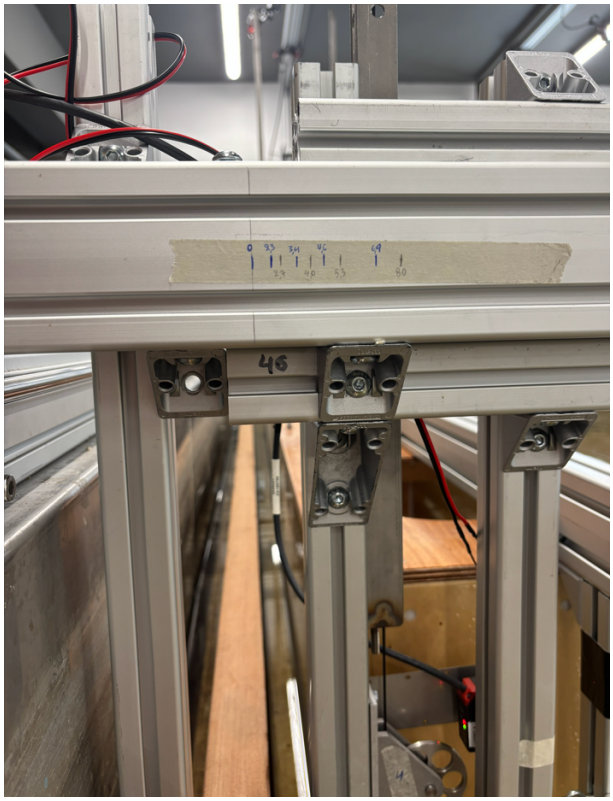

Figure 34: Setting the lateral gap, with the 69 mm aluminium spacer fitted between the reference bracket and the sliding unit.



Figure 35: Verification of the gap, with the aluminium spacer fitted between the model and the wooden wall.



Figure 36: The stainless steel ruler mounted on the wooden wall, used as a fixed reference for measuring the water depth.

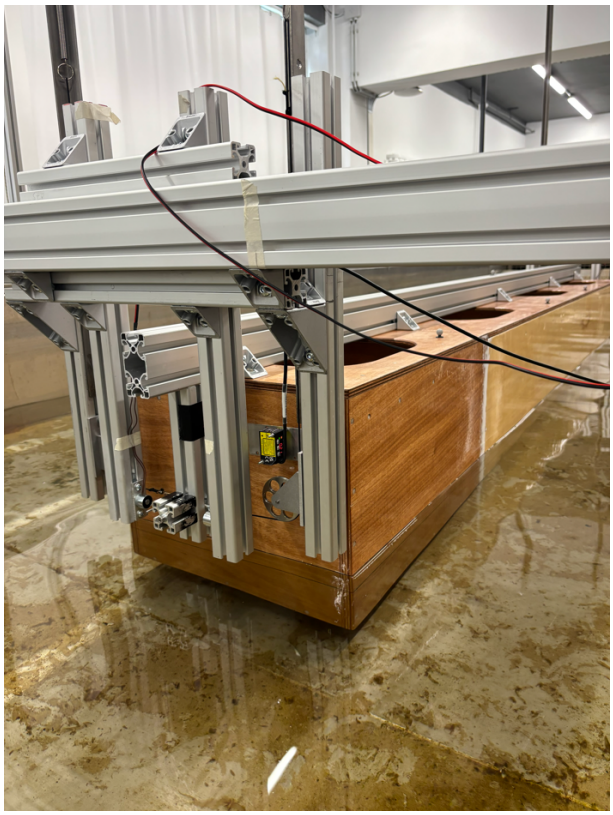

Figure 37: The laser sensor, mounted above the pulley on a plate that extends towards the model, at the fore of the model. The sliding frame carrying the pulley and the vertical spring holder is visible alongside.

A.2 Facility Documentation

This appendix documents the known imperfections of the Wave Flume Tank introduced in Section 4.2.

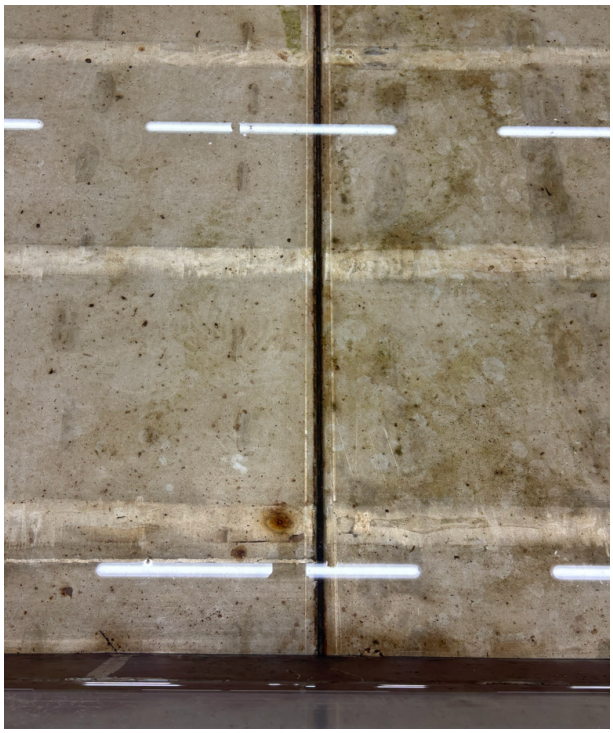

Figure 38: Close up of the flume bottom, showing the weld seam bump and the thin algae layer covering the tank floor.



Figure 39: Close up of the flume wall, showing the wall bump.

A.3 Mass Properties and Ballasting

This appendix documents the derivations behind the dry testing and ballasting of the model vessel described in Section 4.3.

A.3.1 Yaw Inertia via Torsional Swing Test

The empty model's yaw mass moment of inertia was measured by suspending it from two threads of equal length l, fixed to the ceiling and attached to the model symmetrically about the centerline at a distance d on either side. A small angular displacement about the vertical axis was applied, and the resulting torsional period T was measured over 50 oscillations. The yaw mass moment of inertia about the model's centre of gravity follows from

$$I_{zz} = \frac{m\, d^2\, T^2\, g}{4\pi^2\, l} \tag{32}$$

where m is the mass of the unballasted model and g is gravitational acceleration.

A.3.2 Ballast Placement

The mass, centre of gravity, and yaw moment of inertia of the model were set by placing lead blocks on foam supports. For all components together (hull, backbone, ballast, and instrumentation), the total mass and the centre of gravity follow from

$$m = \sum_i m_i, \qquad \mathbf{x}_{cg} = \frac{1}{m} \sum_i m_i\, \mathbf{x}_i \tag{33}$$

where m_i is the mass of component i, $\mathbf{x}_i$ is the position of its centre of gravity, m is the total mass of the model, and $\mathbf{x}_{cg}$ is the position of the model's centre of gravity.

The yaw moment of inertia I_{zz} about this centre of gravity is the sum of the contributions of all components. For a ballast block, the contribution follows from the parallel axis theorem as

$$I_{zz,b} = m_b \left(x_b^2 + y_b^2\right) + \tfrac{1}{12}\, m_b \left(l_b^2 + w_b^2\right) \tag{34}$$

where m_b is the block's mass, x_b and y_b are the coordinates of the block's centre relative to the model's centre of gravity, and l_b and w_b are the length and width of the block in the horizontal plane (for a stack, the footprint of the stack).

The positions of the available lead blocks were solved for so that the combined mass, centre of gravity, and I_{zz} matched the target values of Table 3, while keeping the ballast as symmetric about the centreline as the available blocks allowed, to limit the product of inertia I_{xy}. The resulting layout is shown in Figure 40. The grey areas are the foam blocks that carry the lead. The large lead blocks are labelled with their mass in kg. The small unlabelled block has a mass of 0.5 kg. The blocks that carry only a number are stacks of lead blocks of approximately 1 kg each, where the number gives how many blocks are stacked. All dimensions in the figure are in mm.

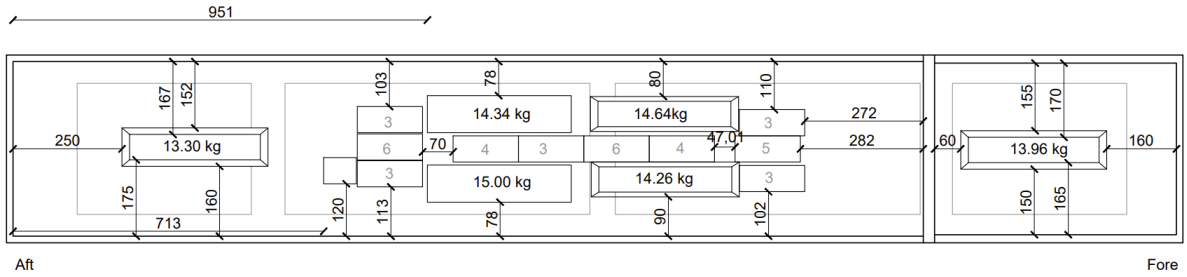

Figure 40: Plan view of the ballast layout, aft on the left and fore on the right. All dimensions in mm.

A.4 Mooring Stiffness Derivation

This appendix documents the full derivation behind the mooring stiffness values used in Section 4.4. It covers the geometric projection that turns individual mooring line stiffnesses into the stiffness matrix terms $C_{\text{moor},11}$, $C_{\text{moor},22}$ and $C_{\text{moor},66}$ of Equations (8) and (9), the full scale comparison of candidate mooring lines, the Froude scaling used to bring the selected configuration down to model scale, and the as-built stiffness of the spring and pulley setup actually used.

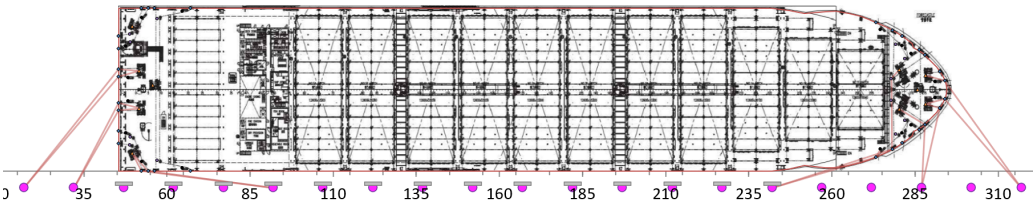

(a) Plan view, mooring lines to the quay bollards.

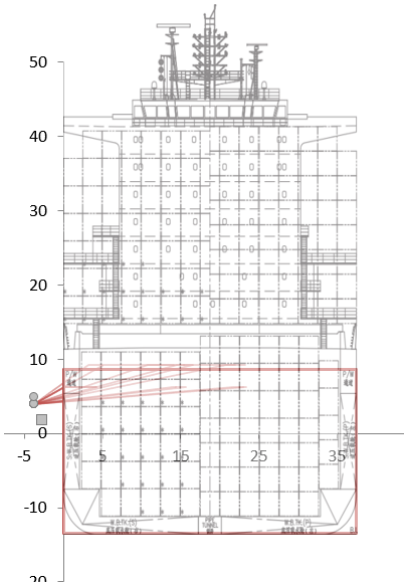

(b) Stern section, vertical lead angle to the bollards.

Figure 41: General arrangement of the Polar Mexico [51], annotated with the mooring line layout used to derive the target stiffness.

A.4.1 Line Stiffness Projection

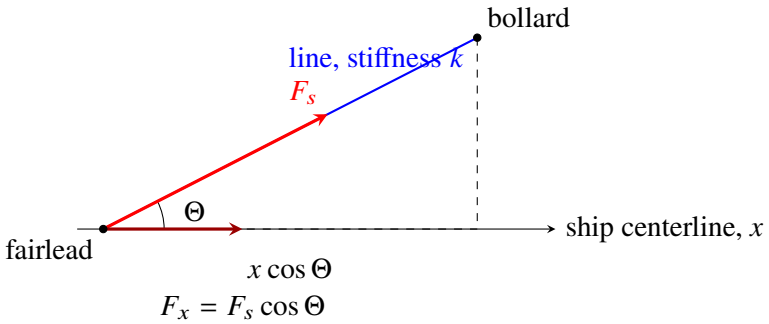

Figure 42: Projection of a single mooring line's axial force onto the vessel's motion, following the geometry of Figure 41. A displacement x stretches the line by $x\cos\Theta$, producing a line force $F_s = kx\cos\Theta$ whose component along x is $F_x = F_s\cos\Theta = kx\cos^2\Theta$, so the line contributes a stiffness $k\cos^2\Theta$ to that direction.

Consider a single mooring line running from a fairlead on the vessel to a bollard on the quay, making a horizontal lead angle Θ with the ship's centerline (Figure 42). Over the small displacements relevant to a moored decay test, the line is idealized as a linear spring of axial stiffness k, read from the load elongation gradient of the line material at its working pretension [13]. A vessel displacement x along the centerline stretches the line by the projection of x onto the line's own axis,

$$\delta l = x\cos\Theta, \tag{35}$$

so the resulting increment in line tension is

$$F_s = k\,\delta l = k\,x\cos\Theta. \tag{36}$$

Only the component of F_s along the direction of x resists the vessel's motion, giving a restoring force

$$F_x = F_s\cos\Theta = k\,x\cos^2\Theta, \tag{37}$$

so that this one line contributes $k\cos^2\Theta$ to the diagonal stiffness in that direction. The same argument applied to a displacement perpendicular to the ship's centerline gives a contribution $k\sin^2\Theta$, and projecting the elongation onto one direction and the reaction force onto the other gives the cross coupling term $k\sin\Theta\cos\Theta$. Summing over the full set of n mooring lines, with attachment point (x_i, y_i) relative to the vessel's centre of gravity and lead angle Θ_i, gives the mooring stiffness matrix terms used in Equations (8) and (9):

$$C_{\text{moor},11} = \sum_{i=1}^{n} k_i\cos^2\Theta_i, \qquad C_{\text{moor},22} = \sum_{i=1}^{n} k_i\sin^2\Theta_i, \tag{38}$$

$$C_{\text{moor},66} = \sum_{i=1}^{n} k_i\,(x_i\sin\Theta_i - y_i\cos\Theta_i)^2\,, \tag{39}$$

where $x_i\sin\Theta_i - y_i\cos\Theta_i$ is the perpendicular distance from the vessel's centre of gravity to the line of action of line i, i.e. its yaw moment arm. Equations (38) and (39) are the method implemented in

the Haskoning mooring stiffness tool used to produce Table 17 below, with each k_i taken from OCIMF MEG4 line load elongation data at the pretension listed for that option [13].

A.4.2 Full Scale Stiffness Comparison

With the line layout of Figure 41 fixed, the full scale stiffness matrix was computed for eight candidate mooring line configurations, spanning two line materials, two minimum breaking loads (MBL), and two pretension levels expressed as a percentage of MBL. Table 17 lists the result. A higher pretension moves the operating point further up the material's nonlinear load elongation curve and therefore increases the tangent stiffness, which is why every material and MBL pair stiffens between its 5 % and 10 % row.

Table 17: Full scale mooring stiffness matrix terms for eight candidate mooring line configurations, computed from the layout of Figure 41 using OCIMF MEG4 line data [13]. Option 7 was selected as representative of the range spanned by the eight configurations.

Option	Line Material	MBL (kN)	Pretension	$C_{\text{moor},11}$ (kN/m)	$C_{\text{moor},22}$ (kN/m)	$C_{\text{moor},66}$ (kN m/rad)
1	Nylon	600	5 %	300	296	4,422,663
2	Nylon	600	10 %	371	366	5,447,686
3	Nylon	750	5 %	366	361	5,399,143
4	Nylon	750	10 %	452	446	6,669,280
5	Polyester/PP	600	5 %	488	482	7,204,682
6	Polyester/PP	600	10 %	638	630	9,411,715
7	**Polyester/PP**	**750**	**5 %**	**596**	**588**	**8,796,888**
8	Polyester/PP	750	10 %	776	766	11,452,566
Minimum				300	296	4,422,663
Maximum				776	766	11,452,566
Mean				538	531	7,937,615

Polyester/PP: polyester/polypropylene. $C_{\text{moor},66}$ is physically a moment per unit rotation.

Option 7, a polyester/polypropylene line rated at 750 kN MBL and pretensioned to 5 % of MBL, was selected because it sits close to the mean of all eight configurations in every column of Table 17 while corresponding to a mooring material and pretension combination that is itself a realistic choice for this vessel class, rather than an artificial average constructed after the fact. Its sway and yaw stiffness, $C^{\text{full}}_{\text{moor},22} = 588\,\text{kN/m}$ and $C^{\text{full}}_{\text{moor},66} = 8{,}796{,}888\,\text{kN m/rad}$, is the full scale target carried forward to model scale below. $C_{\text{moor},11}$ is not used further, since surge is outside the scope of this thesis (Section 4.1).

A.4.3 Froude Scaling of the Target Stiffness

Under Froude similitude, force scales as λ^3 (mass scales as λ^3 at equal g) and length as λ, so a translational stiffness, force over length, scales as

$$C^{\text{model}}_{\text{moor},kk} = C^{\text{full}}_{\text{moor},kk}/\lambda^2, \qquad kk = 11, 22. \tag{40}$$

A rotational stiffness is a moment, force times length, over an angle, which is itself dimensionless and therefore scale invariant, so

$$C^{\text{model}}_{\text{moor},66} = C^{\text{full}}_{\text{moor},66}/\lambda^4. \tag{41}$$

With $\lambda = 87$ (Section 4.1) and the selected full scale configuration, Option 7 of Table 17 ($C^{\text{full}}_{\text{moor},22} = 588\,\text{kN/m}$, $C^{\text{full}}_{\text{moor},66} = 8{,}796{,}888\,\text{kN m/rad}$), Equations (40) and (41) give the target model scale values

$$C^{\text{target}}_{\text{moor},22} = \frac{588{,}000}{87^2} = 77.7\ \text{N/m}, \qquad C^{\text{target}}_{\text{moor},66} = \frac{8.797 \times 10^9}{87^4} = 153.6\ \text{N m/rad}, \tag{42}$$

These are the targets the spring and pulley arrangement of Section 4.4 was designed against. The stiffness it actually realizes is derived next.

A.4.4 As-Built Spring Stiffness

Rather than have springs manufactured to this exact rating, the setup was built from four springs already available in the laboratory, nominally rated at 20 N/m, and each was calibrated individually rather than assumed identical: loaded with a known mass and set into free vertical oscillation, its stiffness was recovered from the measured period (full procedure in Section 4.5). This gave four somewhat different values, 17.9, 17.9, 18.0 and 17.8 N/m, summing to $\sum k_i = 71.6\,\text{N/m}$, close to but not identical to $4 \times 17.9\,\text{N/m}$ above purely by coincidence of rounding.To achieve the correct yaw stiffness the two springs were attached at the aft and two at the fore with a lever arm of $x = 1.41$ m from the vessel's centre of gravity and oriented perpendicular to the centerline.

A.4.5 Spring Calibration

Each of the four springs used in the mooring setup (Section 4.4) was calibrated individually before installation, since springs nominally rated at the same 20 N/m were found to vary slightly in practice. Each spring was suspended from a crane and loaded with a known mass of $m = 1$ kg, and its own mass was measured beforehand across the four springs (Figure 43). The loaded spring was displaced and released into free vertical oscillation, and the time for 20 complete cycles was recorded with a stopwatch, from which the period T follows directly. The stiffness was then obtained from

$$k = \frac{4\pi^2 \left(m + 0.5 m_{\text{spring}}\right)}{T^2}, \tag{43}$$

with m_{spring} the spring's own mass. Each spring was measured 3 to 4 times to check repeatability, and the resulting values were averaged to give the $\bar{k}$ used throughout this thesis.

A.5 Instrumentation Specifications

This appendix collects the full manufacturer specifications, calibration results, and bench supply settings for the instrumentation introduced in Section 4.7.



Figure 43: Calibration setup.

A.5.1 OptiTrack Motion Capture



Figure 44: The OptiTrack cameras, mounted on aluminium profiles at the ceiling above the flume.

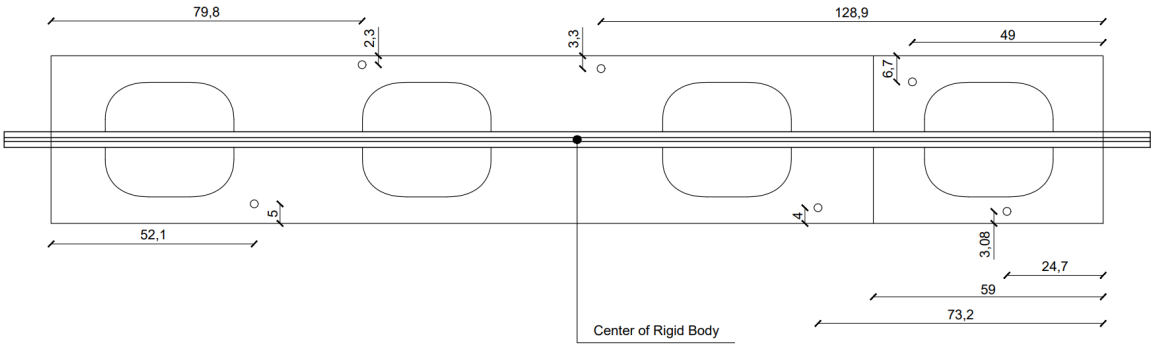

Figure 45: Top view of the deck showing the OptiTrack marker positions and the centre of the rigid body, to which the measured motions are referenced. Dimensions in cm.

The system was calibrated before testing began, achieving the accuracy summarized in Table 18.

Table 18: OptiTrack calibration result summary.

Metric	Value	Rating
Overall reprojection, mean 3D error	0.244 mm	Exceptional
Overall reprojection, mean 2D error	0.081 px	Exceptional
Worst camera, mean 3D error	0.229 mm	Exceptional
Worst camera, mean 2D error	0.096 px	Exceptional
Triangulation, residual mean error	0.3 mm	within 2.6 mm recommended
Overall wand error, mean error	0.076 mm	Exceptional
Ray length, suggested max	5.4 m	–

A.5.2 Panasonic HG-C1100 Laser Sensor

The fore-end laser sensor is a Panasonic HG-C1100, a CMOS laser displacement sensor. Table 19 lists the specifications relevant to this thesis, taken from the manufacturer datasheet.

Table 19: Panasonic HG-C1100 specifications (manufacturer datasheet).

Parameter	Value
Measurement center distance	100 mm
Measurement range	±35 mm
Repeatability	70 μm
Light source	red semiconductor laser, Class 2, 1 mW max, 655 nm
Supply voltage	12 to 24 V DC ±10 %
Analog output	0 to +5 V (+5.2 V at alarm), 100 Ω output impedance
Response time	switchable between 1.5, 5 and 10 ms

A.5.3 Micro-Epsilon optoNCDT 1420 Laser Sensor

The aft-end laser sensor is a Micro-Epsilon optoNCDT 1420, ILD1420-25 variant. Table 20 gives its factory settings, taken from the manufacturer datasheet.

Table 20: Micro-Epsilon optoNCDT ILD1420-25 factory settings (manufacturer datasheet).

Parameter	Value
Measuring range	25 mm
Start of measuring range	25 mm
End of measuring range	50 mm
Y	21 mm

The sensor has a current output interface, with a measurement frequency of 2 kHz and a digital interface at 921.6 kBps. The measuring range corresponds to an analog output of $I = 4$ mA (digital 643) at 0 % FSO and $I = 20$ mA (digital 64877) at 100 % FSO.

A.5.4 Electromagnet Release Mechanism

Each end of the model was held in place before release by an ITS-MS 2015 electromagnet, specified in Table 21.

Table 21: ITS-MS 2015 electromagnet specifications (manufacturer datasheet).

Parameter	Value
Holding force	20 N
Supply voltage	24 V DC
Power	2.0 W
Weight	25 g

A.5.5 Bench Power Supplies

The electromagnets were powered from a Tenma bench supply, set to 24 V with a 1.2 A current limit (Figure 46a), matching the electromagnet's 24 V DC rating and comfortably above its 83 mA rated draw at 2.0 W. A Multicomp Pro MP710080 bench supply, set to 15.00 V and drawing 0.089 A (Figure 46b), was used for both of the laser sensors.

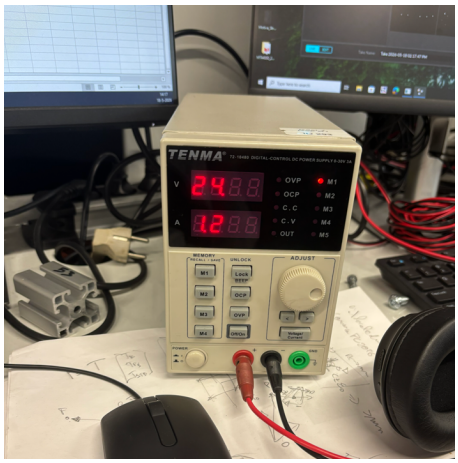

(a) Tenma bench supply, set to 24 V, powering the electromagnets.

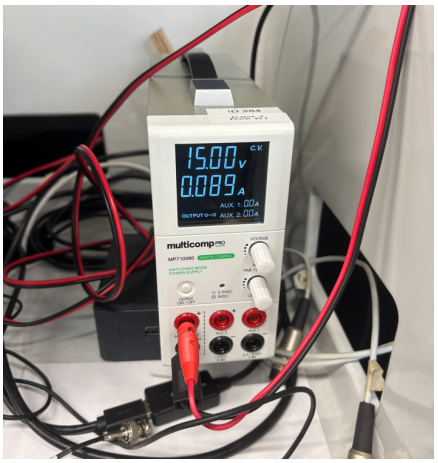

(b) Multicomp Pro bench supply, set to 15 V.

Figure 46: Bench power supplies used for the instrumentation.

A.5.6 Laser Calibration Coefficients

Both laser sensors output a voltage that varies with the distance to the target, so each sensor was calibrated to convert the recorded voltage into a distance. The target was placed at known distances and the output voltage of the sensor was recorded at each distance, giving the calibration points in Table 22. A straight line was fitted to the points of each sensor with the method of least squares. Only changes in distance are used in the processing, so only the slope of the line is needed,

$$\Delta d = c_1 \, \Delta U \tag{44}$$

where Δd is the change in distance to the target in mm, ΔU is the change in the output voltage of the sensor in V, and c_1 is the calibration slope in mm/V.

Table 22: Laser calibration points.

Sensor	Distance (mm)	Voltage (V)
Panasonic HG-C1100	80	3.90
	100	2.50
	110	1.80
	125	0.67
optoNCDT 1420	50	4.50
	70	7.65
	80	9.38

The resulting slopes are $c_1 = -13.96\,\text{mm/V}$ for the Panasonic HG-C1100 and $c_1 = 6.17\,\text{mm/V}$ for the Micro-Epsilon optoNCDT 1420. The output of the Panasonic sensor decreases with distance, which gives the negative sign. The slopes are valid within the calibrated distances, 80 to 125 mm for the Panasonic and 50 to 80 mm for the optoNCDT.

B

Data Processing

This appendix gives the parameter values, the checks and the discarded runs behind the processing of the moored decay records in Chapter 5. It follows the order of the chapter.

B.1 Release Detection and Zero Centering

Table 23 gives the parameters of the release detection (Equation 17) and of the zero centering (Equation 18). The baseline is the mean of a window of 100 samples whose standard deviation is below the noise of the held signal. The threshold is about three times this noise. The tail used for the zero centering is the last 2 s of the camera record.

Table 23: Parameters of the release detection and the zero centering.

Parameter	Symbol	Sway	Yaw
Noise of the held signal (limit for the baseline window)		0.08 mm	0.003°
Baseline window		100 samples	100 samples
Threshold	δ	0.25 mm	0.01°
Window length	n_w	5 samples	5 samples
Tail for zero centering	N_t	200 samples (2 s)	200 samples (2 s)

The calibration factors of the lasers were applied in the acquisition software, which converted the sensor output from volts to millimeters, so the laser files need no conversion. The offset of the calibration was not corrected in the software.

B.2 Comparison of the Camera with the Laser Reconstruction

A run was discarded if the difference of Equation 20 exceeds 1.0 mm in sway or 0.03° in yaw anywhere in the record, about five percent of the release amplitude. Table 24 lists all runs that were discarded during the processing.

Table 24: Runs discarded during the processing of the moored decay records.

Degree of freedom	Run	Reason
Sway	248	Laser comparison, largest difference 1.03 mm
Sway	347	Filter cutoff check
Yaw	334	Laser comparison, largest difference 0.033°
Yaw	365	Laser comparison, largest difference 0.031°
Yaw	264	Marked as failed in the test log
Yaw	328	Marked as failed in the test log

B.3 Filtering

The sway frequency of every run was measured from the time between two troughs of the unfiltered signal. This measurement uses the small, fast cycles at the end of the decay, so it gives the highest sway

frequency of the run. The cutoff frequency was required to be at least 1.3 times this frequency. Because the filter is applied forward and backward, the gain at a frequency is the square of Equation 21,

$$|H_{fb}(f)| = |H(f)|^2 = \frac{1}{1 + (f/f_c)^{2n}}, \tag{45}$$

where $|H_{fb}|$ is the gain of the filter applied forward and backward, and f, f_c and n are as in Equation 21. At a ratio of 1.3 between the cutoff and the checked frequency the gain is 0.89, so the amplitude of the checked cycle is reduced by at most 11 %. The first two half-cycles have lower frequencies, and their amplitude is reduced by less than 0.5 %. Sway run 347 did not meet the requirement and was discarded.

The yaw frequency of the cases lies between 0.09 and 0.16 Hz. The cutoff frequency of the yaw filter was chosen per case, and is given in Table 25.

Table 25: Cutoff frequency of the yaw filter.

Case	Cutoff frequency [Hz]
1 to 4	0.4
5	0.3
6 to 8	0.5
9 to 12	0.3

B.4 Quadratic Damping

Figure 47 shows both methods for the run with the largest quadratic damping in Cases 2, 3 and 6. Case 4 is shown in Figure 22. The fitted decays differ by at most 0.14, 0.16 and 0.28 mm in Cases 2, 3 and 6 in both methods, and the RMSE increases by at most 0.01, 0.01 and 0.04 mm.

With B_2 free, the quadratic damping was positive in 11 of the 43 sway runs in both methods, all in Cases 2, 3, 4 and 6, and zero in all other runs and in every yaw run. The values of these 11 runs are given in Table 9 of Section 5.1.7.

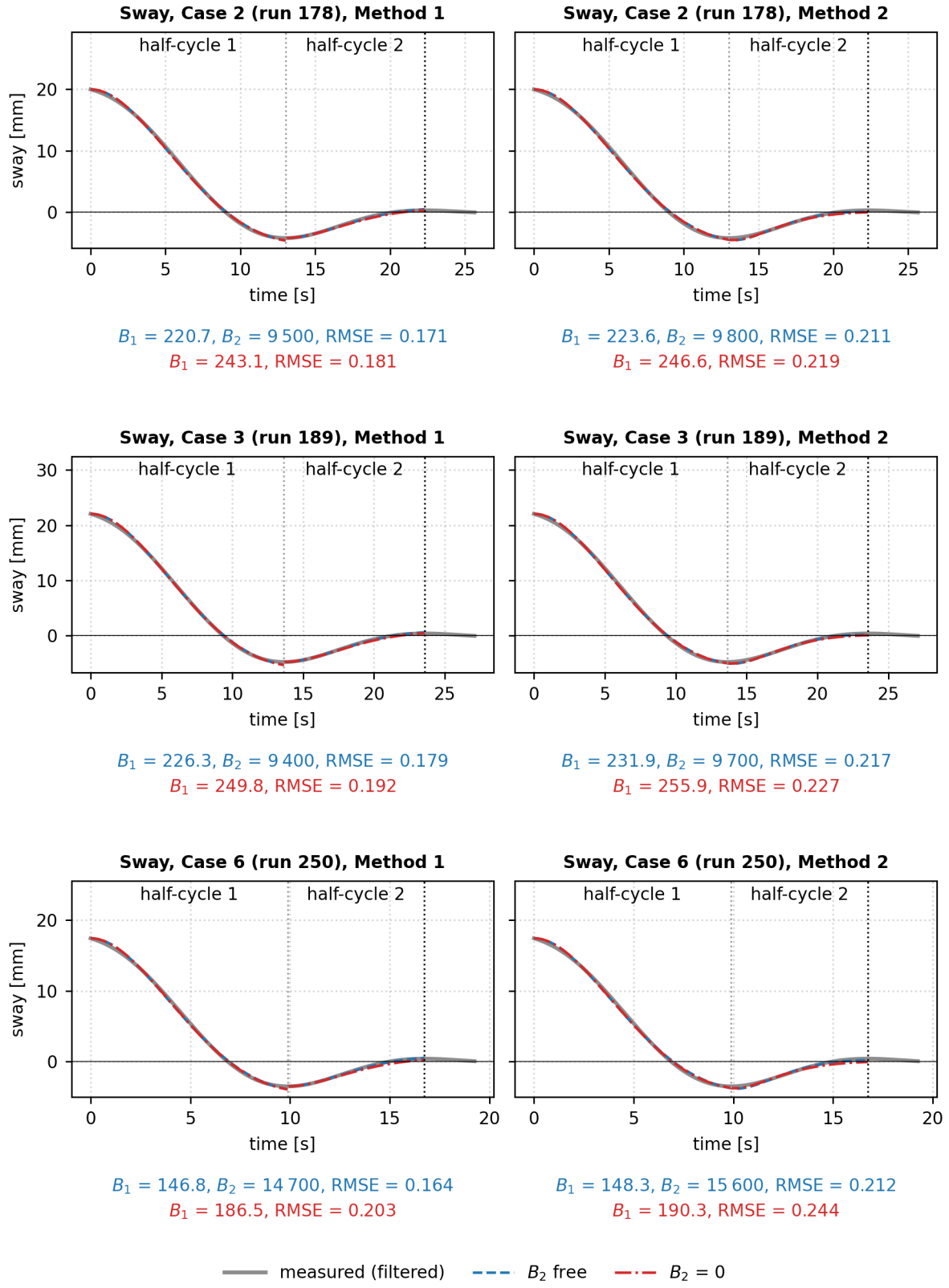

Figure 47: Sway decay of the run with the largest quadratic damping in Cases 2, 3 and 6, fitted with B_2 free and with $B_2 = 0$ in Method 1 (left) and Method 2 (right). Values: B_1 [N s/m], B_2 [N s^2/m^2], RMSE [mm].

B.4.1 Convergence of the Fit

Every fit was started from several starting values. Method 1 used 5 starting values of B_1 (and of B_2 when it is free). Method 2 used 12 combinations of A_0, A_1, B_1 and B_2 with B_2 free, and 16 combinations of A_0, A_1 and B_1 with $B_2 = 0$. Although B_2 is fixed in the second case, it has more starting points, because 4 starting points with $B_1 = 500$ N s/m were added to the 12 without B_2. The optimizer improves the values step by step, and one step is one iteration. Figures 48 to 53 show B_1 and B_2 against the iteration, with one line per starting point, for the run of each case with the largest B_2 (runs 178, 189, 157 and 250). The dashed line is the value of the best starting point, the one with the lowest cost. A starting point converges if its final B_1 and B_2 are within 1 % of those of the best starting point. Table 26 gives the number of starting points that converge in each of the 11 runs. The convergence of Method 1 with $B_2 = 0$ for all runs and cases is shown in Section B.5.

In Method 1, all starting points converge in every run, with $B_2 = 0$ and with B_2 free (Figures 48 to 50). With $B_2 = 0$ the lines meet after 25 to 35 iterations. With B_2 free they need 84 to 168 iterations, and some stay on a plateau for a long time before they reach the common value.

In Method 2, 164 of the 176 starting points converge with $B_2 = 0$ (Figure 51). The others stay at a wrong value, for example at $B_1 = 107$ N s/m in Case 4. With B_2 free, only 72 of the 132 starting points converge (Figures 52 and 53). Those that converge need up to 690 iterations, and the others end at $B_2 = 0$ or at other values, for example at about 3 000 N s^2/m^2. The fit needs 204 to 912 iterations with B_2 free and 91 to 528 with $B_2 = 0$.

Table 26: Number of starting points that converge in each run: the final B_1 (and B_2 when it is free) is within 1 % of that of the best starting point.

		Method 1		Method 2	
Case	Run	$B_2 = 0$	B_2 free	$B_2 = 0$	B_2 free
2	178	5 of 5	5 of 5	15 of 16	5 of 12
	180	5 of 5	5 of 5	15 of 16	6 of 12
	182	5 of 5	5 of 5	16 of 16	7 of 12
3	185	5 of 5	5 of 5	15 of 16	7 of 12
	187	5 of 5	5 of 5	15 of 16	7 of 12
	189	5 of 5	5 of 5	15 of 16	7 of 12
4	157	5 of 5	5 of 5	14 of 16	6 of 12
	201	5 of 5	5 of 5	14 of 16	6 of 12
	203	5 of 5	5 of 5	14 of 16	6 of 12
6	250	5 of 5	5 of 5	15 of 16	8 of 12
	252	5 of 5	5 of 5	16 of 16	7 of 12
All		55 of 55	55 of 55	164 of 176	72 of 132

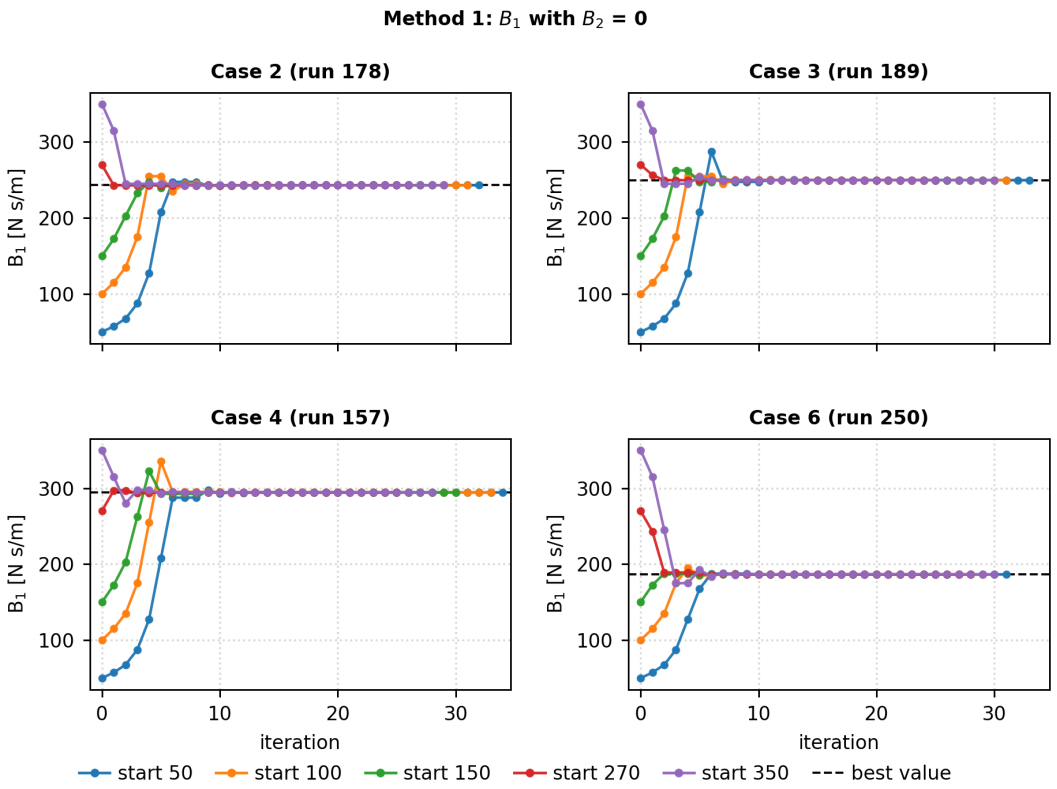

Figure 48: Method 1: B_1 with $B_2 = 0$ against the iteration. Dashed line: best value.

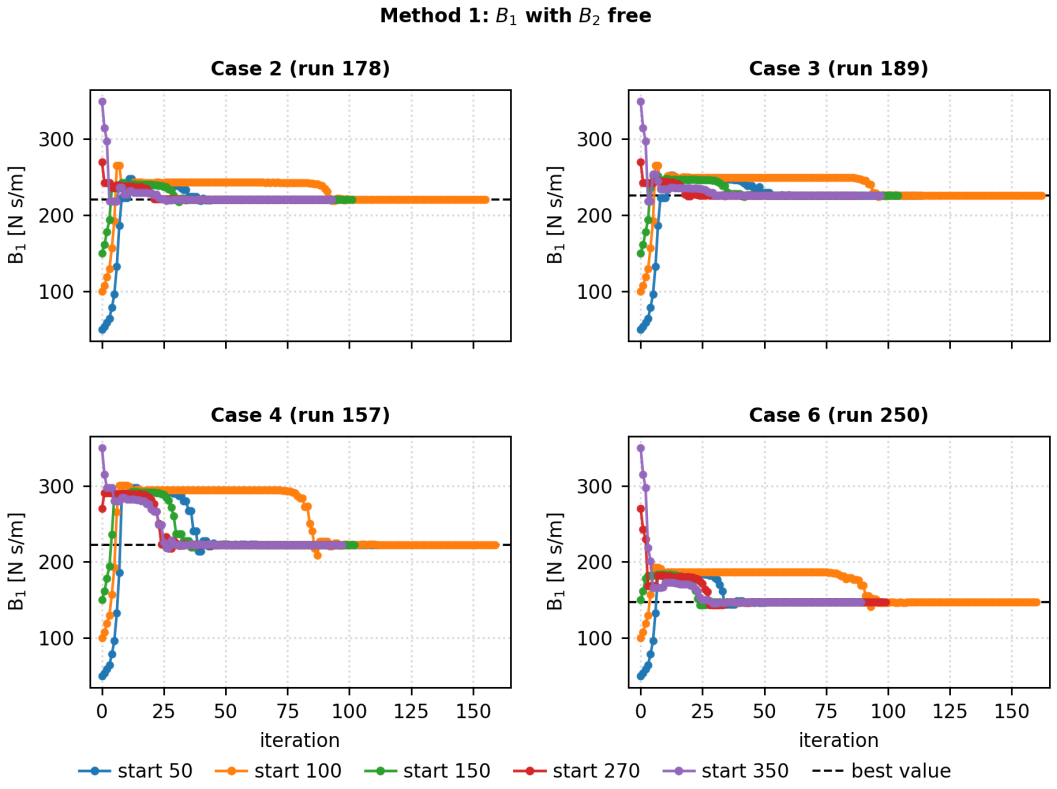

Figure 49: Method 1: B_1 with B_2 free against the iteration. Dashed line: best value.

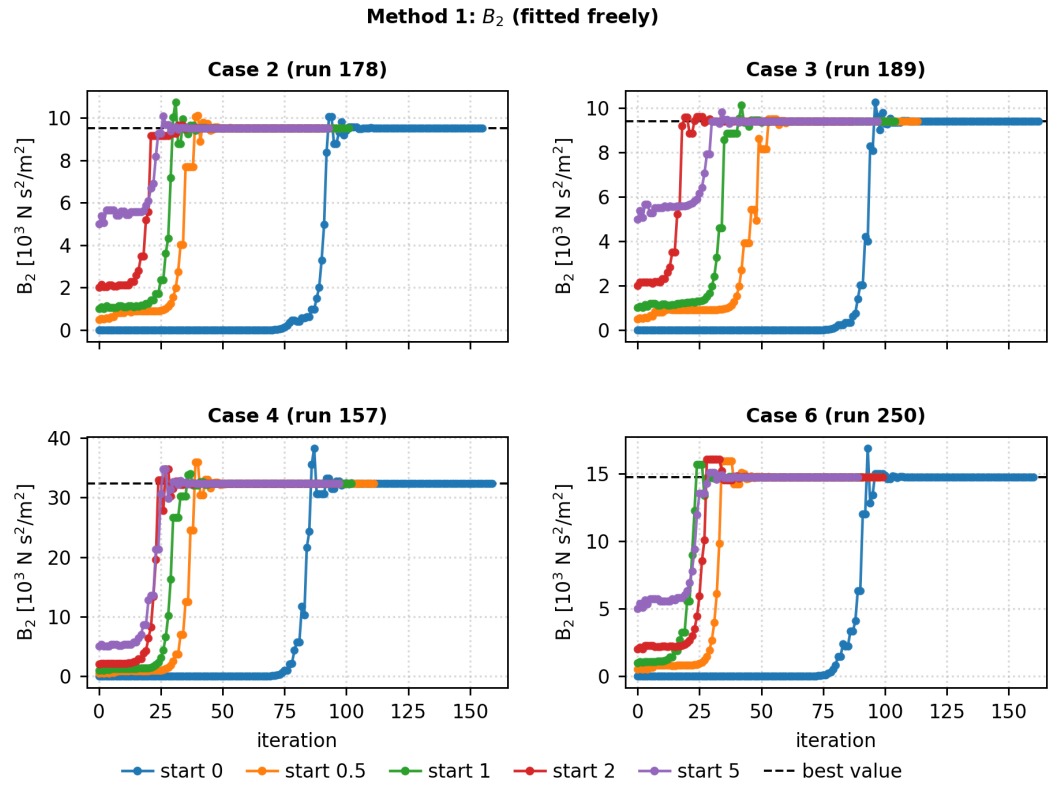

Figure 50: Method 1: B_2 (free) against the iteration. Dashed line: best value.

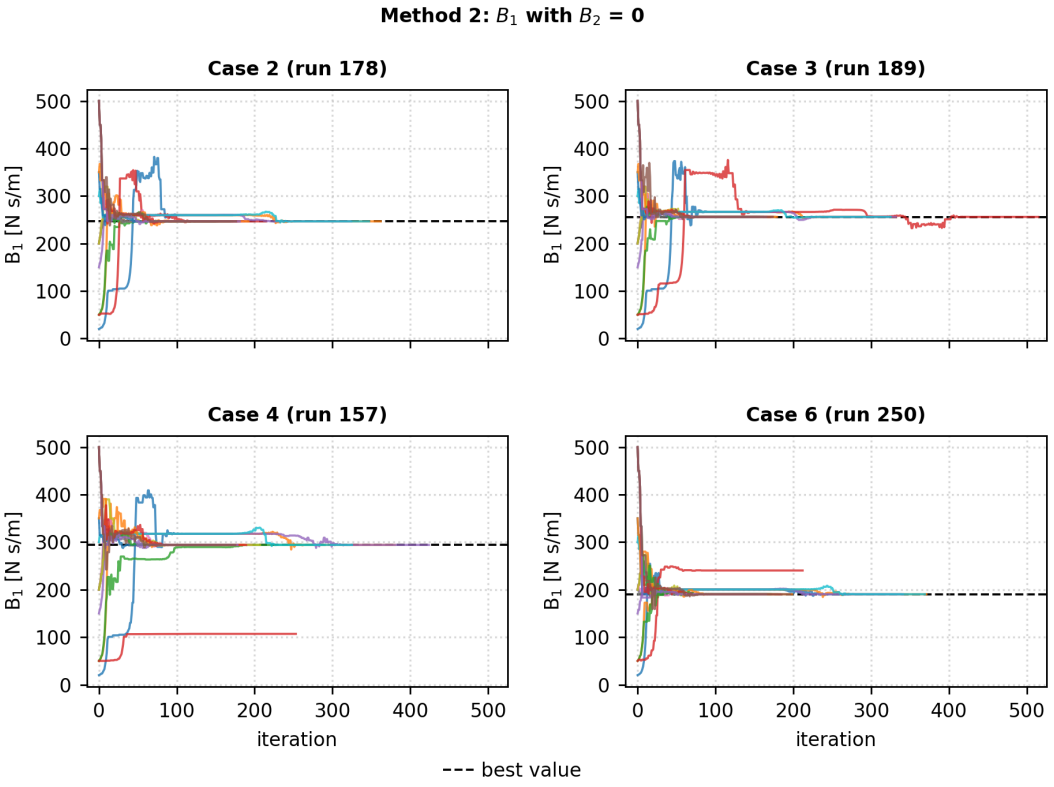

Figure 51: Method 2: B_1 with $B_2 = 0$ against the iteration. Dashed line: best value.

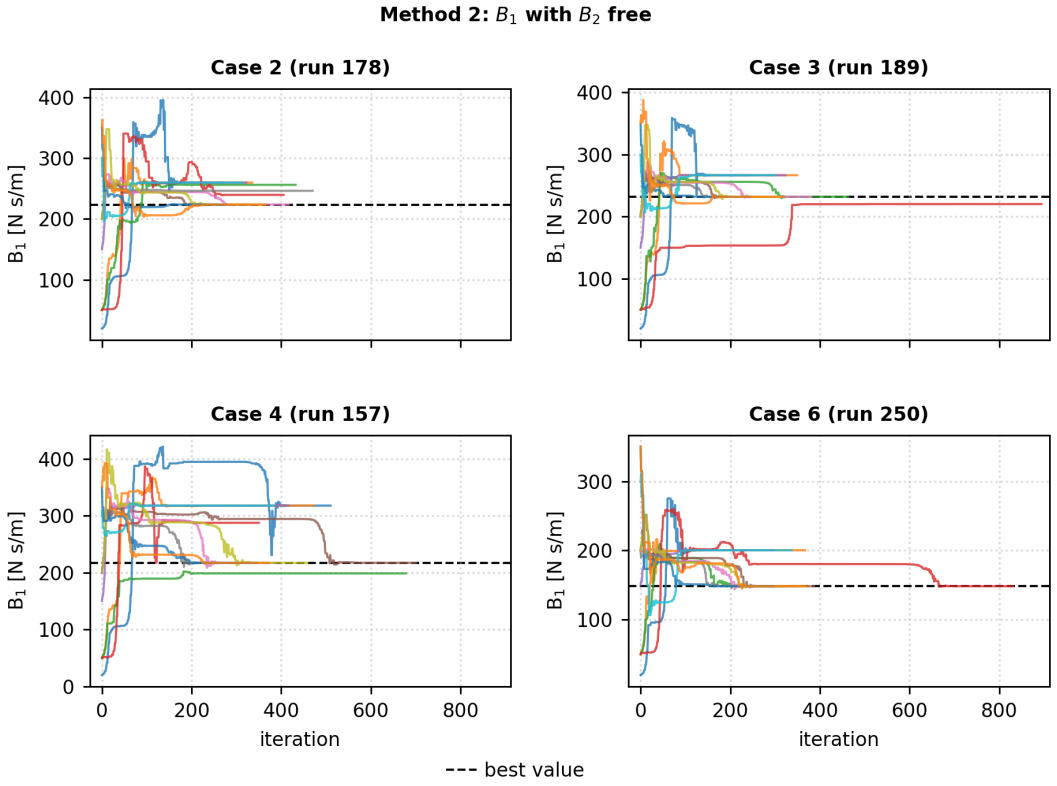

Figure 52: Method 2: B_1 with B_2 free against the iteration. Dashed line: best value.

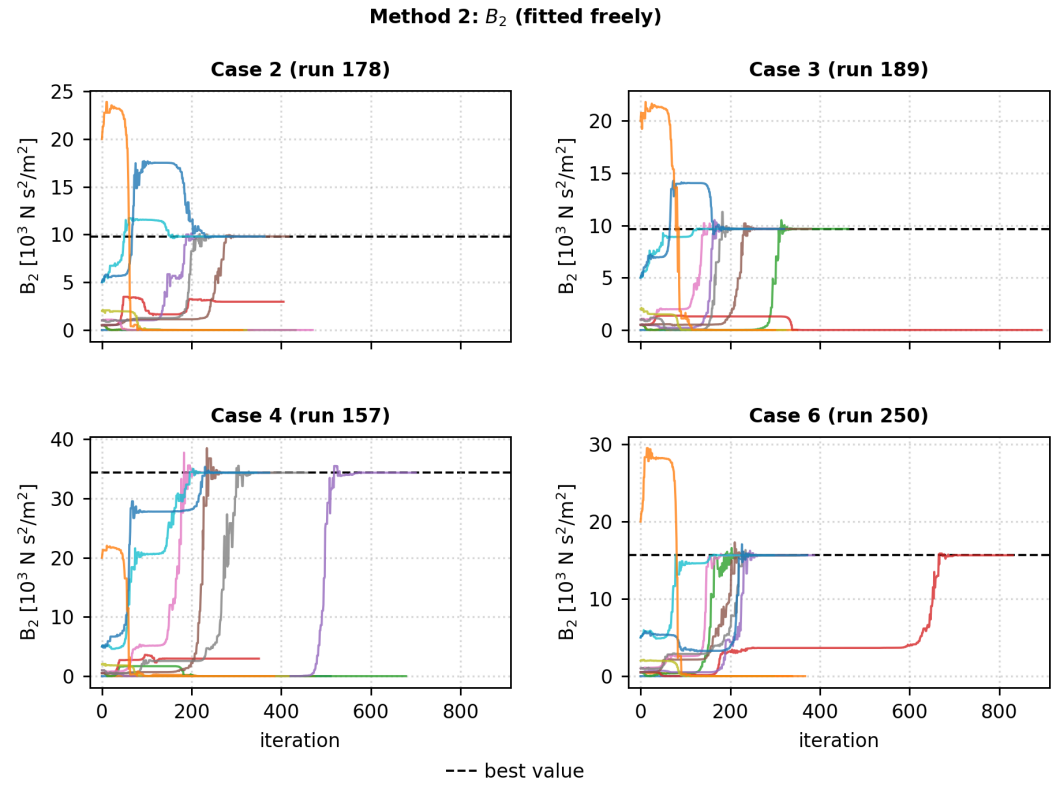

Figure 53: Method 2: B_2 (free) against the iteration. Dashed line: best value.

B.5 Convergence for All Cases

Section B.4.1 shows the convergence of the fit for the runs with a positive B_2. This section shows it for all runs of all cases in Method 1, the method used for the results (Section 6.2), with $B_2 = 0$, in sway and in yaw. The starting points and the criterion for convergence are the same as in Section B.4.1.

All starting points converge, 215 of 215 in the 43 sway runs and 195 of 195 in the 39 yaw runs (Table 27). Figures 54 and 55 show the worst run of each case, which is the run that needs the most iterations. The lines meet after 24 to 35 iterations in sway and after 24 to 33 in yaw.

Table 27: Number of starting points that converge in each case with $B_2 = 0$ in Method 1. Runs: number of runs of the case.

	Sway		Yaw	
Case	Runs	Converging	Runs	Converging
1	4	20 of 20	3	15 of 15
2	3	15 of 15	5	25 of 25
3	3	15 of 15	3	15 of 15
4	3	15 of 15	3	15 of 15
5	5	25 of 25	4	20 of 20
6	2	10 of 10	3	15 of 15
7	3	15 of 15	3	15 of 15
8	3	15 of 15	3	15 of 15
9	5	25 of 25	3	15 of 15
10	5	25 of 25	3	15 of 15
11	4	20 of 20	3	15 of 15
12	3	15 of 15	3	15 of 15
All	43	215 of 215	39	195 of 195

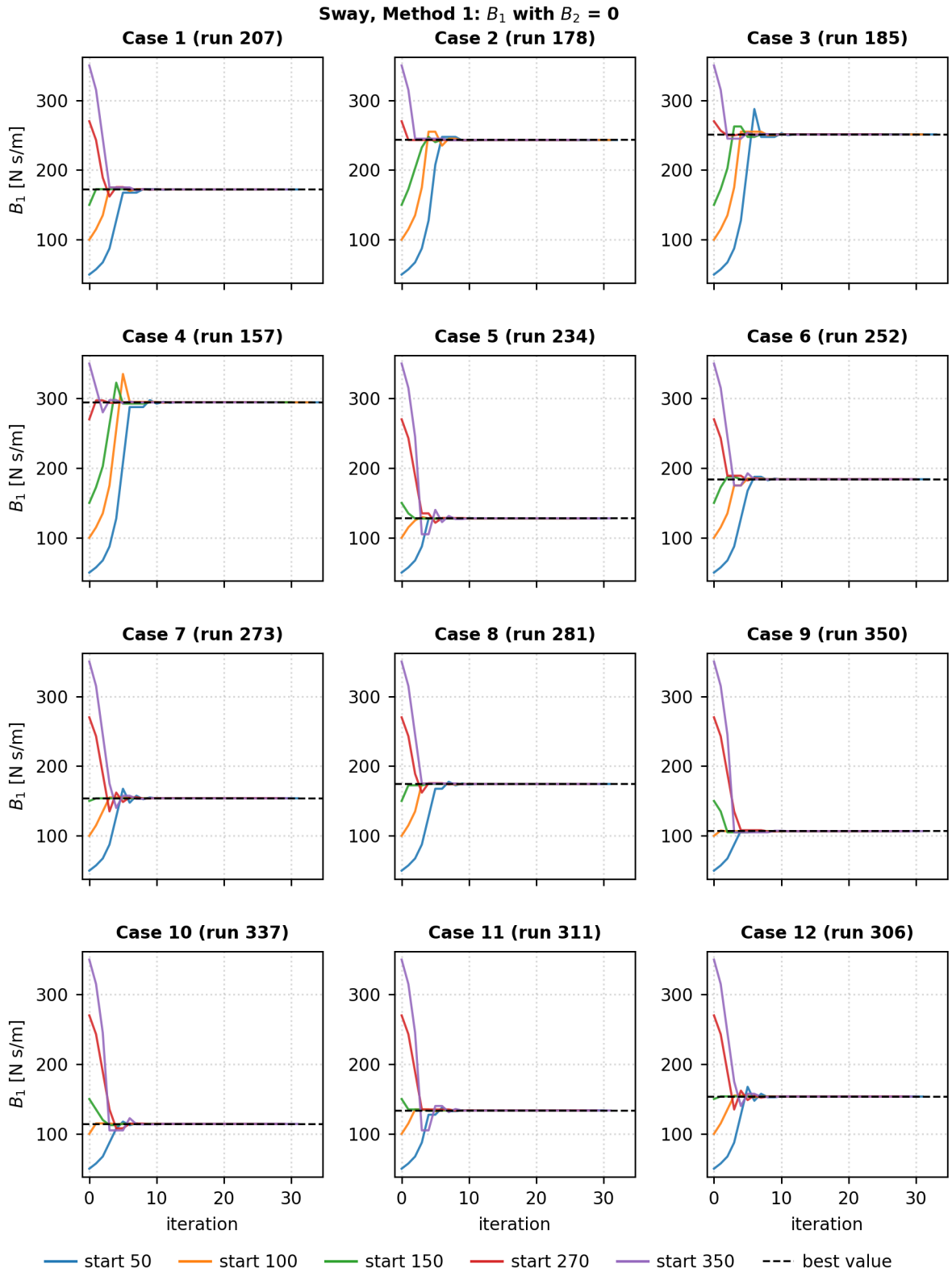

Figure 54: Sway, Method 1: B_1 with $B_2 = 0$ against the iteration for the worst run of each case. One line per starting point. Dashed line: best value.

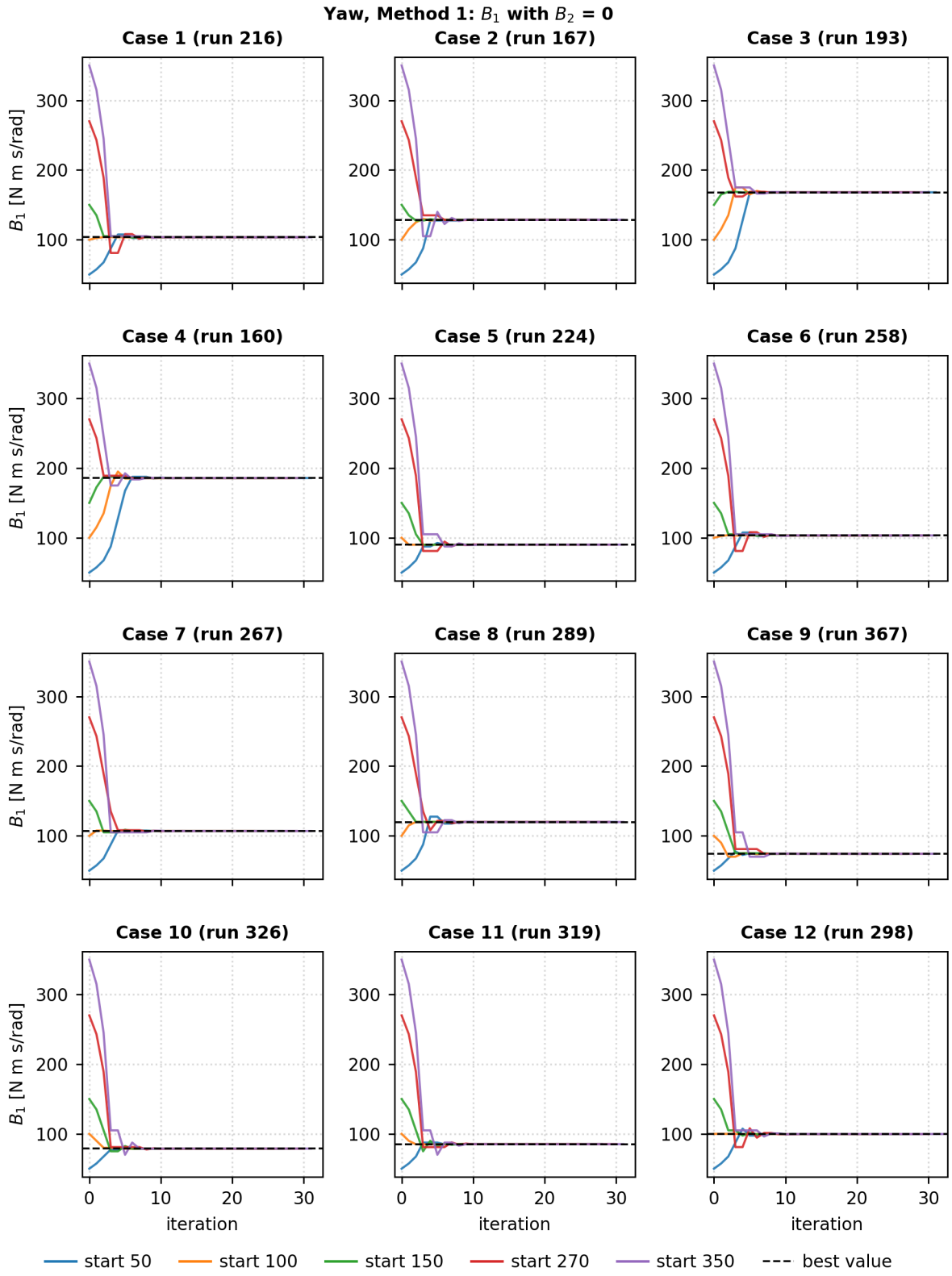

Figure 55: Yaw, Method 1: B_1 with $B_2 = 0$ against the iteration for the worst run of each case. One line per starting point. Dashed line: best value.

B.6 Dry Test Pendulum

The period of a cycle of the bare pendulum is taken between successive crests or troughs. The damping follows from the logarithmic decrement of two consecutive crests or troughs,

$$B = 2\zeta m\omega_n, \qquad \zeta = \frac{\delta}{\sqrt{4\pi^2 + \delta^2}}, \qquad \delta = \ln \frac{x_i}{x_{i+1}}, \tag{46}$$

where B is the linear damping coefficient, ζ is the damping ratio, m is the mass, $\omega_n = 2\pi/T$ is the natural frequency with period T, δ is the logarithmic decrement and x_i and x_{i+1} are the displacements of two consecutive crests or troughs. The rope stiffness follows from the mean period of three runs as $k_p = m\omega_n^2$. The length of the rope was validated in situ, based on the period measured in the first run. The stiffness of the springs and pulleys obtained from the dry fit, after subtraction of k_p, is higher than the calibrated stiffness. The most likely cause is the rope, whose stiffness depends on its length: 1 cm of rope changes the stiffness by about 1 N/m, so an uncertainty of a few centimeters is enough to explain the difference.

B.7 DIFFRAC Calculations

This section gives the parameter values behind the DIFFRAC calculations of behind the DIFFRAC calculations of Section 5.3. Section 5.3.

B.7.1 Quay and Damping Lid

For the berth cases the quay is a rigid vertical wall over the full water depth at the lateral position

$$y_{quay} = \frac{B}{2} + G, \tag{47}$$

where y_{quay} is the lateral position of the quay measured from the centerline of the model, B is the beam of the model and G is the lateral gap between the hull and the quay, both at model scale.

The damping lid has the length of the model and fills the gap, apart from a small clearance c to the hull and to the quay on each side,

$$w_{lid} = G - 2c, \qquad y_{lid} = \frac{B}{2} + \frac{G}{2}, \tag{48}$$

where w_{lid} is the width of the lid, y_{lid} is the lateral position of its center and c is a clearance of 1 mm at full scale ($1.15 \cdot 10^{-5}$ m at model scale) that keeps the lid panels from touching the hull and the quay. The center of the lid lies at half the length of the model, and the damping coefficient is 0.03. The number of lid panels along the length follows the number of hull panels along the length, rounded to an odd number, and the lid is refined along its length and across its width together with the hull (Table 29). A damping coefficient of 0.10 gave the same coefficients as 0.03. Table 28 gives the position of the quay and the dimensions of the lid for each lateral gap.

Table 28: Quay position and damping lid dimensions at model scale. The lid is 2.70 m long, and its center lies at 1.35 m along the model.

G [m] full scale	G [mm] model scale	y_{quay} [m]	w_{lid} [m]	y_{lid} [m]
3	34	0.249	0.03398	0.2320
4	46	0.261	0.04598	0.2380
6	69	0.284	0.06898	0.2495

B.7.2 Mesh Convergence

The mesh of the hull is defined by the number of panels along the length n_L, across the half beam n_{Bh} and over the draft n_T. All three were multiplied by the same scale factor s,

$$n_L = s\, n_{L,0}, \qquad n_{Bh} = s\, n_{Bh,0}, \qquad n_T = s\, n_{T,0}, \qquad N_{hull} \approx s^2 N_0, \tag{49}$$

where $n_{L,0}$, $n_{Bh,0}$ and $n_{T,0}$ are the numbers of panels of the coarsest mesh, N_0 is its number of hull panels and N_{hull} is the number of hull panels of the refined mesh. Because the factor is the same in all directions, the shape of the panels stays approximately constant and the number of panels grows with about s^2. Table 29 gives the levels. The coarsest level was verified against the hydrostatics: the displacement, the center of buoyancy and the wetted area computed by DIFFRAC matched the hand calculations.

The convergence was assessed for the smallest gap, $G = 34$ mm at $h = 172$ mm, because the flow through the narrow gap between the hull and the quay wall places the highest demand on the mesh. For every level, the added mass and the potential damping were computed over a frequency range that includes the range of the case. In sway, levels 1 to 6 were computed (Figure 56). In yaw, only levels 5 and 6 were computed (Figure 57), since the sway study had already shown that the added mass no longer changes noticeably at these levels.

In sway, the added mass A_{22} decreases with refinement and levels off. It changes by about 0.3 % between levels 4 and 5 and by about 0.2 % between levels 5 and 6, and it is nearly constant over the frequency range of the case. The potential damping B_{22} converges more slowly and still decreases by about 10 % between levels 5 and 6. Its absolute value, however, is very small: about 0.04 N s/m (Table 10), which is less than 0.5 % of the pulley damping of 9.1 N s/m. The remaining mesh dependence of B_{22} therefore has no noticeable effect on the viscous damping obtained from Equation 11.

In yaw, levels 5 and 6 give almost the same coefficients. The added mass A_{66} differs by less than 0.1 % over the whole frequency range, and the potential damping B_{66} by at most about 2 % at the highest frequencies, above the range of the case. Over the frequency range of the case, B_{66} is about 0.2 N m s/rad (Table 10), which is about 1 % of the pulley damping of 18.2 N m s/rad.

Level 6 was used for all DIFFRAC calculations.

Table 29: Mesh levels of the box shaped hull, with the number of panels along the length n_L, across the half beam n_{Bh} and over the draft n_T, and the number of panels of the damping lid along its length and across its width.

						Damping lid	
Level	s	n_L	n_{Bh}	n_T	N_{hull}	Length	Width
0	1	27	4	2	356	27	3
1	1.5	40	6	3	792	39	5
2	2	54	8	4	1 424	53	7
3	3	81	12	6	3 204	81	9
4	4	108	16	8	5 696	107	13
5	5	135	20	10	8 900	135	15
6	6	162	24	12	12 816	161	21

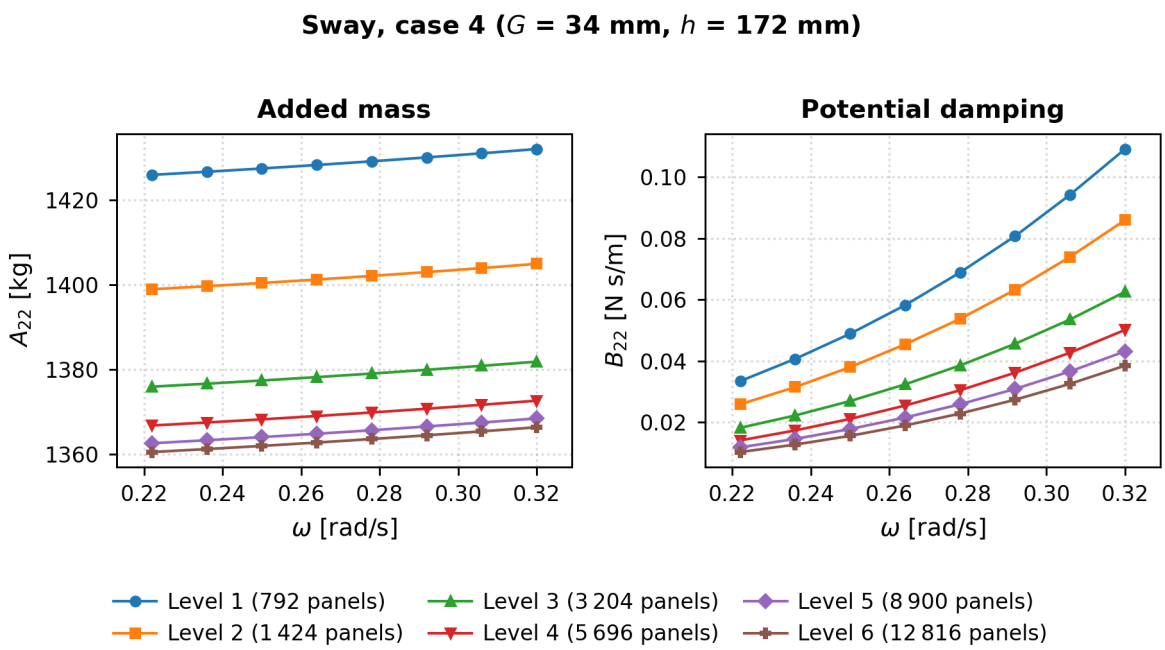

Figure 56: Added mass A_{22} (left) and potential damping B_{22} (right) in sway against the angular frequency for mesh levels 1 to 6, for the smallest gap (G = 34 mm, h = 172 mm).

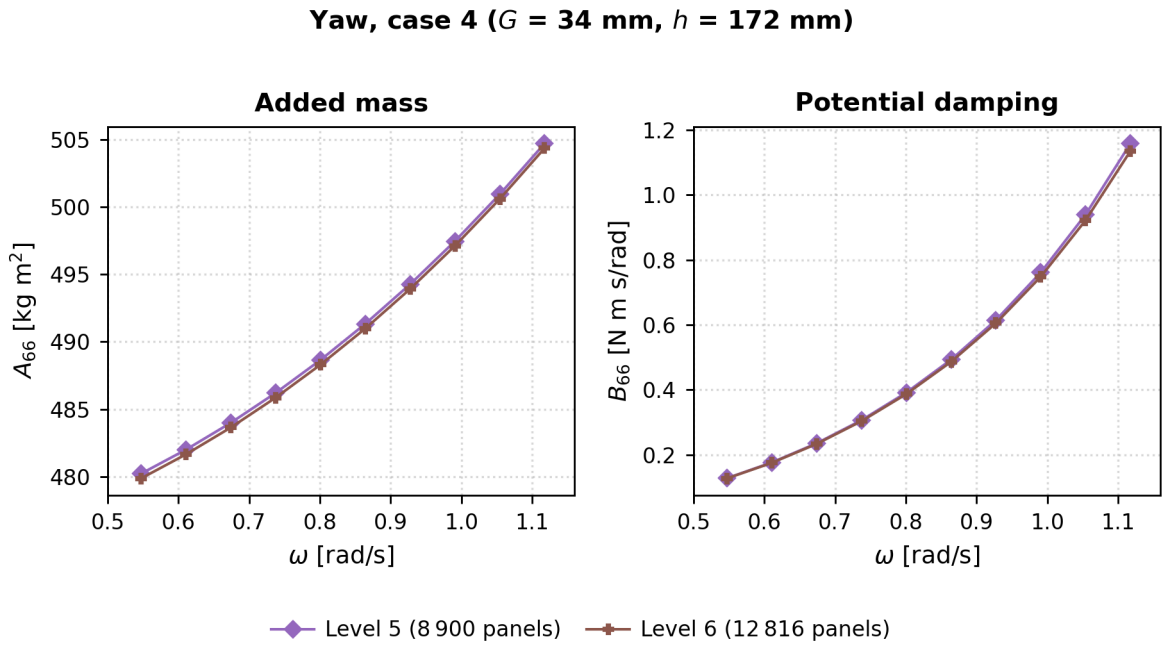

Figure 57: Added inertia A_{66} (left) and potential damping B_{66} (right) in yaw against the angular frequency for mesh levels 5 and 6, for the smallest gap (G = 34 mm, h = 172 mm). The shaded band marks the frequency range of the case.

C

Results

C.1 Decay fits per case

This appendix shows the measured decays and the fits of Method 1 for all cases, for sway in Figures 58 to 60 and for yaw in Figures 61 to 63. Each figure covers one water depth, with one panel per gap. Each panel contains the individual repeat runs and their average, for the measured decay as well as for the fit. Only the runs used in the analysis are shown. The fits cover the first two swings, which are the swings used in the analysis (Section 5.1.6). Since Method 1 restarts each swing from the measured turning point, the fit shows a small step at the start of the second swing.

The box in each panel gives the root mean square error (RMSE) between the measured decay and the fit, as the mean and standard deviation over the repeat runs, together with the number of runs. Sway case 6 is shown in grey, as it is excluded from the results (Section 6.1.1).

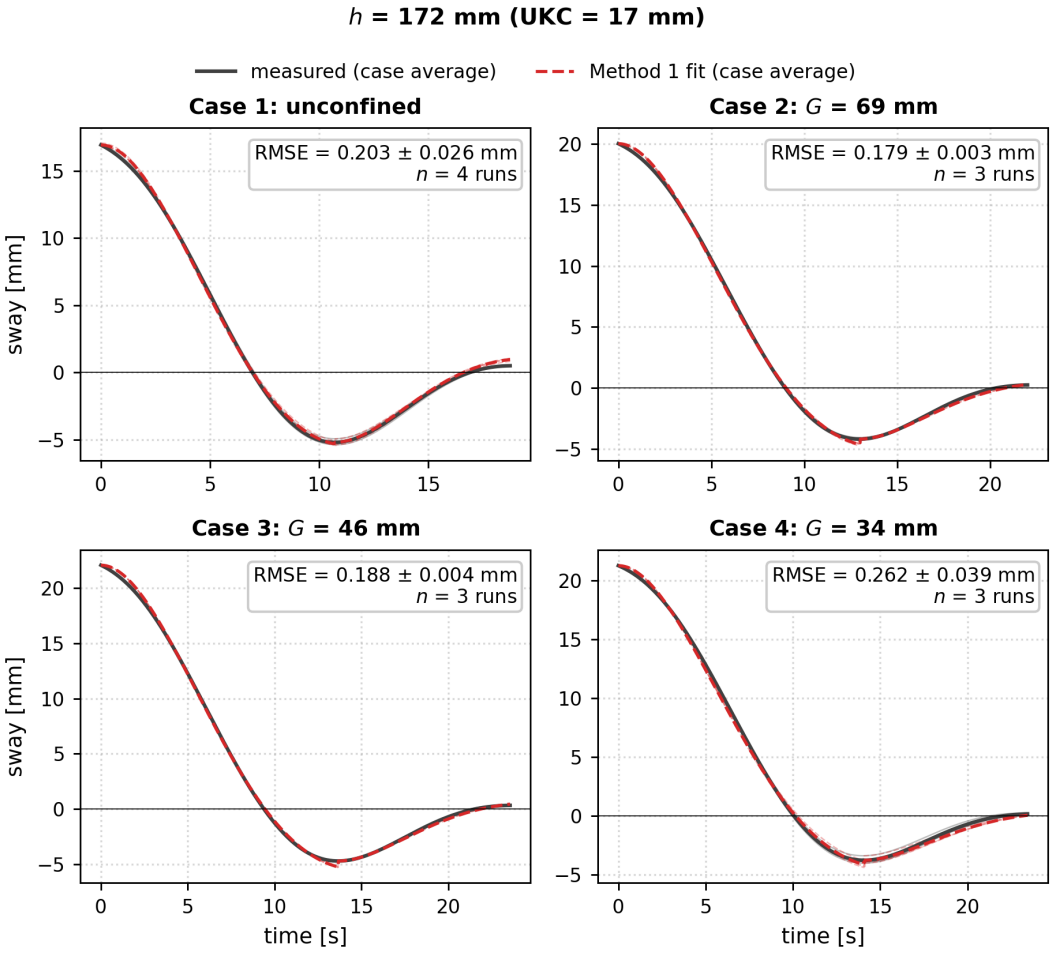

Figure 58: Measured sway decay and Method 1 fit, $h = 172$ mm (cases 1 to 4). Thin lines: individual runs. Thick lines: case average. Box: RMSE of the fit (mean ± sd over the runs) and number of runs.

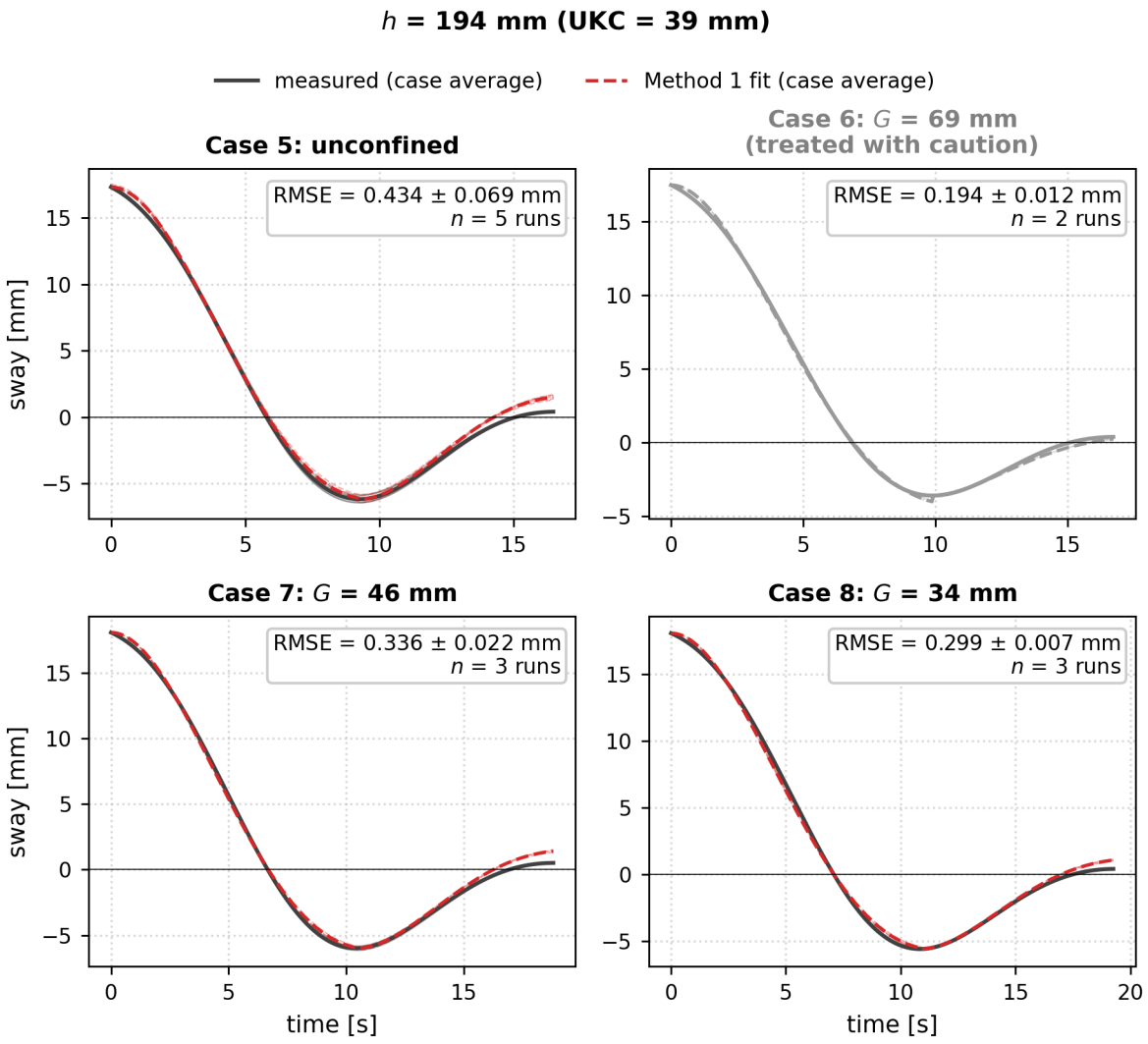

Figure 59: Measured sway decay and Method 1 fit, h = 194 mm (cases 5 to 8). Thin lines: individual runs. Thick lines: case average. Box: RMSE of the fit (mean ± sd over the runs) and number of runs. Case 6 (grey) is excluded from the results.

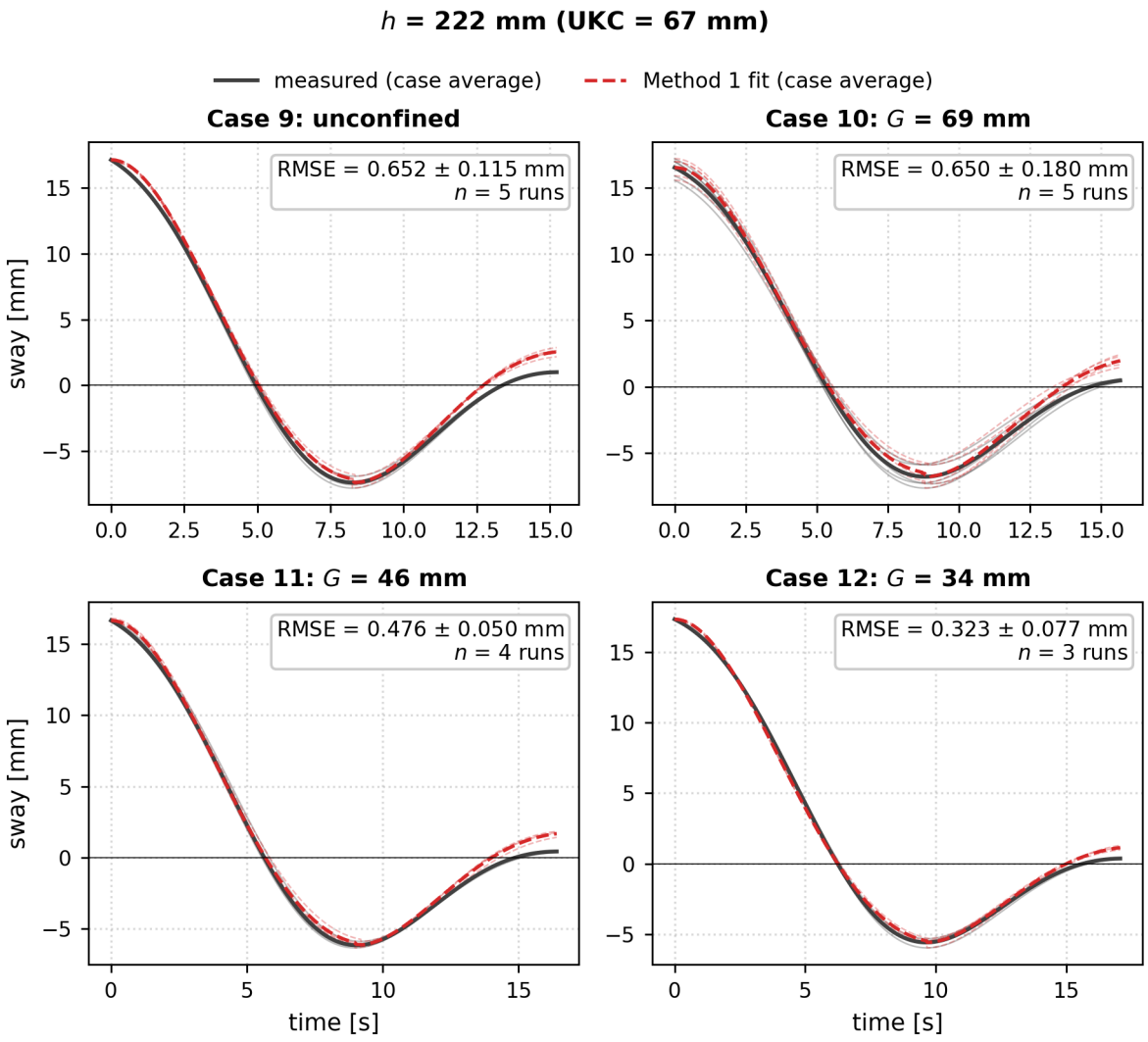

Figure 60: Measured sway decay and Method 1 fit, h = 222 mm (cases 9 to 12). Thin lines: individual runs. Thick lines: case average. Box: RMSE of the fit (mean ± sd over the runs) and number of runs.

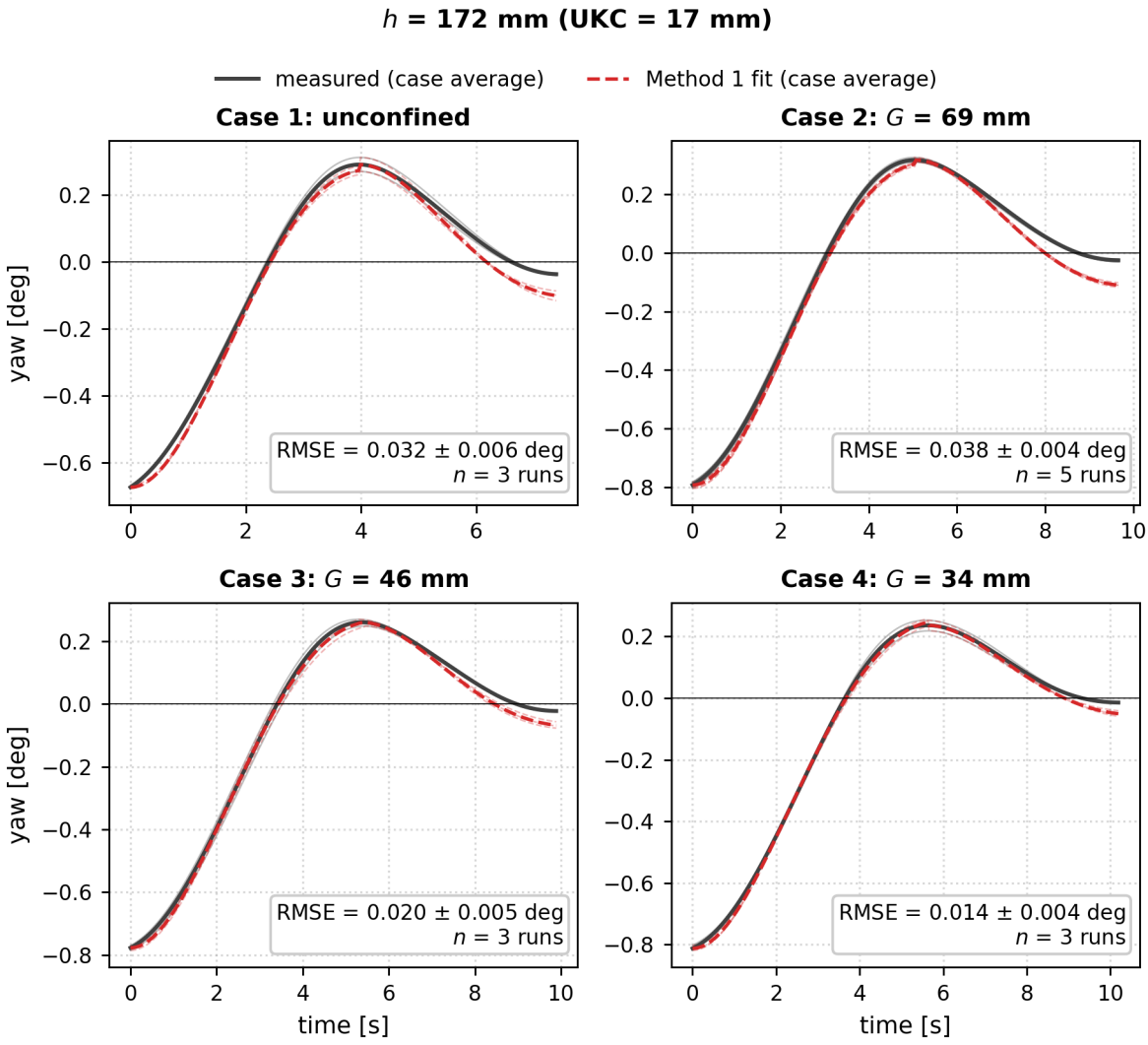

Figure 61: Measured yaw decay and Method 1 fit, h = 172 mm (cases 1 to 4). Thin lines: individual runs. Thick lines: case average. Box: RMSE of the fit (mean ± sd over the runs) and number of runs.

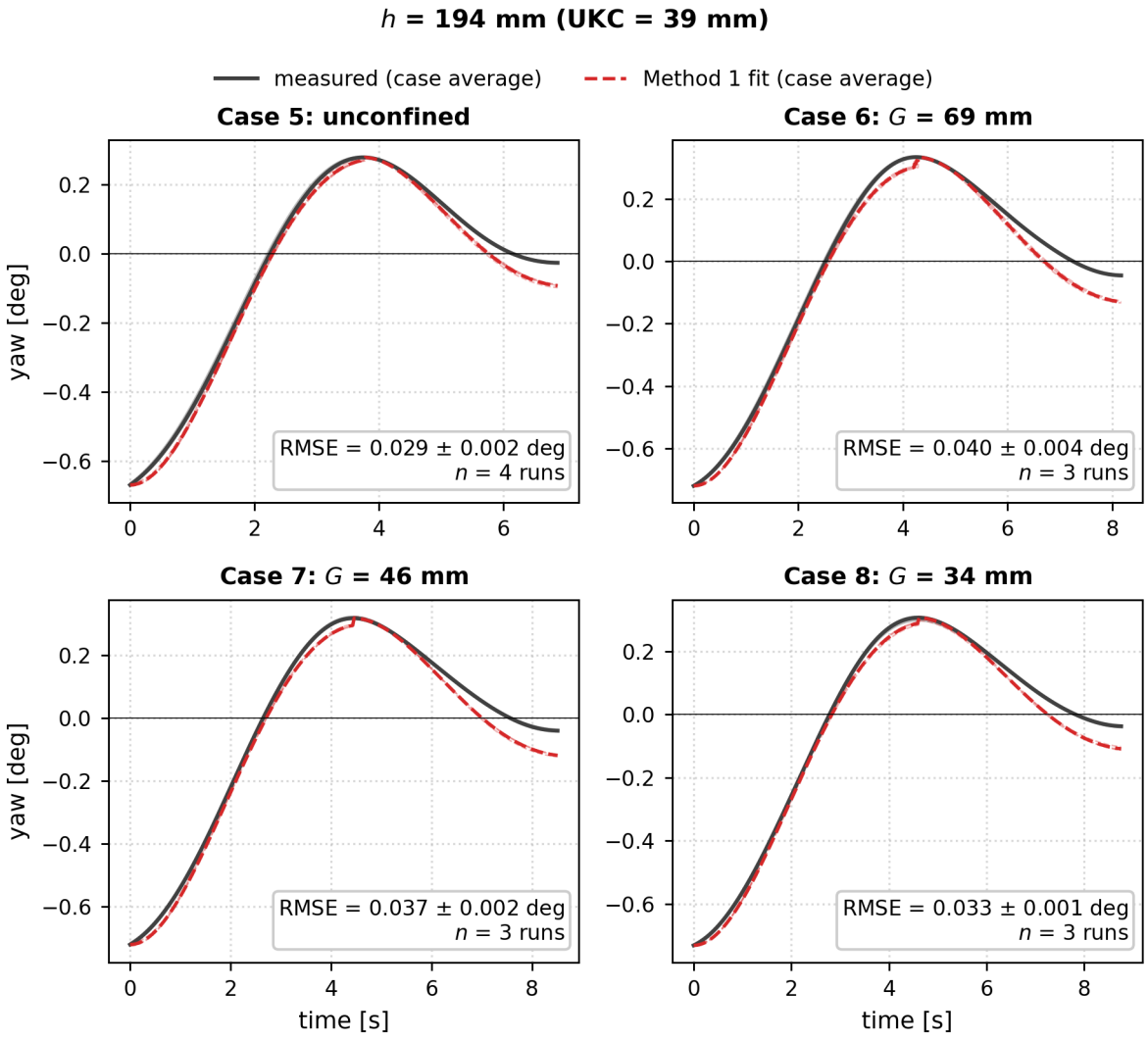

Figure 62: Measured yaw decay and Method 1 fit, h = 194 mm (cases 5 to 8). Thin lines: individual runs. Thick lines: case average. Box: RMSE of the fit (mean ± sd over the runs) and number of runs.

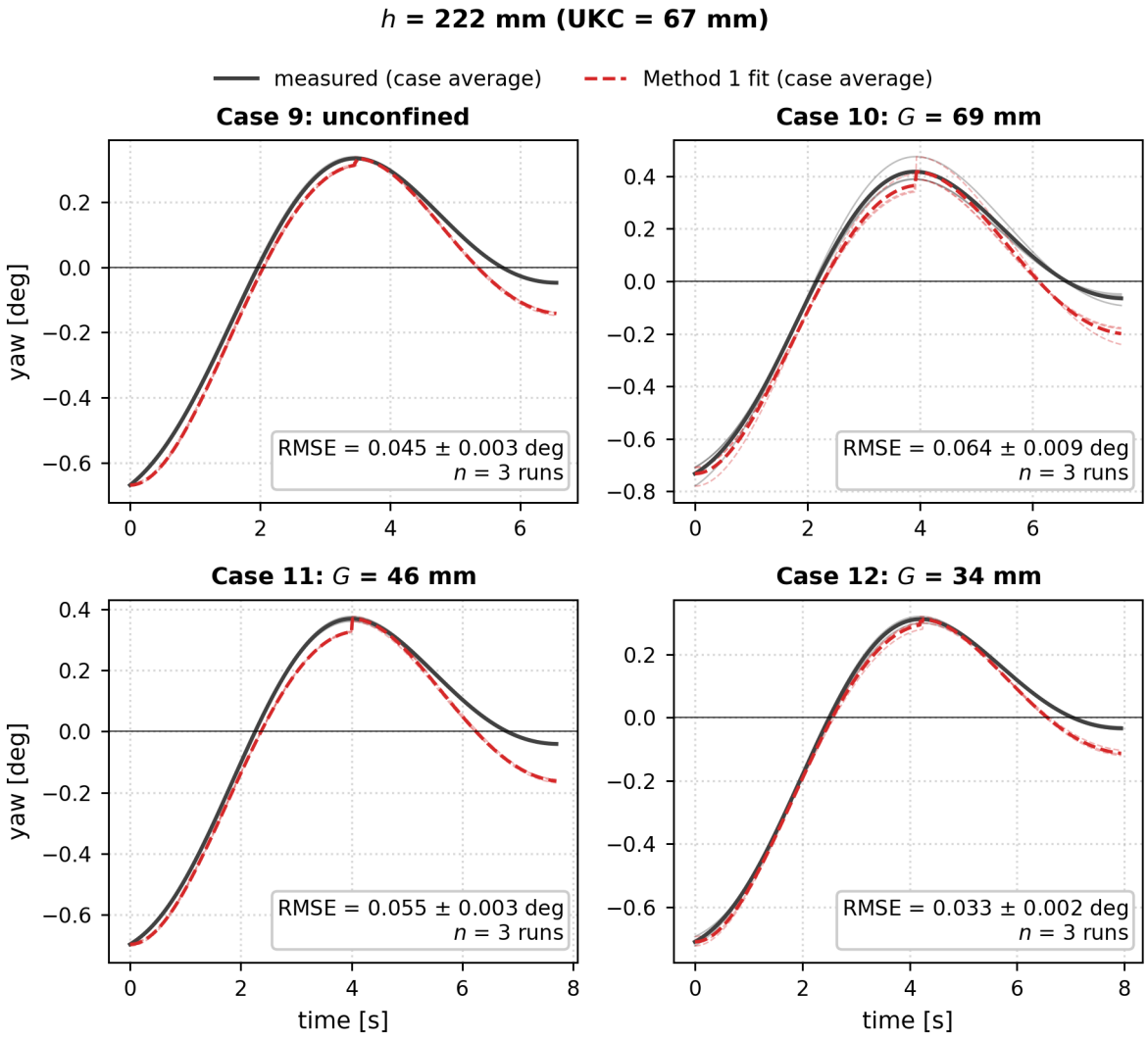

Figure 63: Measured yaw decay and Method 1 fit, $h = 222$ mm (cases 9 to 12). Thin lines: individual runs. Thick lines: case average. Box: RMSE of the fit (mean ± sd over the runs) and number of runs.

D

Cruise Ship

This appendix lists the properties of the reference cruise ship and the mooring options considered for it. The cruise ship model was prepared but not tested.

D.1 Vessel Properties

The reference vessel is the representative cruise ship of PIANC MarCom WG 235 [3]. Its length to beam ratio of 6.29 is almost equal to that of the container ship (6.28), so the same box shaped model is used, at a scale factor λ of 75.2 that fits the 203 m length between perpendiculars to the 2.70 m model length. Table 30 lists the properties.

Table 30: Principal particulars of the reference cruise ship, full scale and model scale (λ = 75.2). Full scale data from PIANC MarCom WG 235 [3].

Parameter	Symbol	Unit	Scaling	Full Scale	Model Scale
Length overall	L_{oa}	m	λ	238	3.166
Length between perpendiculars	L_{bp}	m	λ	203	2.70
Beam	B	m	λ	32.26	0.430
Draft	T	m	λ	8.1	0.108
Depth	D	m	λ	11	0.146
Air draft	n/a	m	λ	66	0.878
Block coefficient	C_b	n/a	n/a	0.65	1.00
Displacement	Δ	t	n/a	34479.3	125.26 kg[a]
Lateral windage area	$A_{w,lat}$	m^2	λ^2	7700	1.362
Longitudinal windage area	$A_{w,long}$	m^2	λ^2	1230	0.218
Yaw radius of gyration	k_{zz}	m	λ	50.75	0.675
Roll radius of gyration	k_{xx}	m	λ	11.94	0.159

[a] As a rectangular box, the model has C_b = 1.00, so its displacement is calculated from the model dimensions and is not scaled from the full scale value.

D.2 Mooring Options

The full scale mooring stiffness was computed for 24 candidate configurations with the same procedure as for the container ship (Section A.4), varying the line type, minimum breaking load (MBL), pretension and number of lines. Table 31 lists the result. HMSF denotes high modulus synthetic fibre lines, which are fitted with a nylon tail of 11 m length and an MBL 1.25 times that of the line. As for the container ship, Polyester/PP lines were used, and Option 18 was taken as representative of the average of the twelve Polyester/PP options, since its sway and yaw stiffness lie within 3 % of their mean. Its $C_{\text{moor},22}$ of 799 kN/m and $C_{\text{moor},66}$ of 10,029,463 kN m/rad give model scale targets of 141.3 N/m and 313.9 N m/rad, scaled as in Section A.4.3. Based on the available springs, the tests were planned with four springs of 37.0 N/m at a lever arm of 1.48 m from the centre of gravity, which give a model scale sway stiffness of 148 N/m and yaw stiffness of 324.2 N m/rad, 105 % and 103 % of the targets, with a minimum pretension of 1.72 N.

Table 31: Full scale mooring stiffness of the candidate configurations. Option 18 was selected.

Option	Line Material	MBL (kN)	Pretension	Tail	Lines	$C_{\text{moor},11}$ (kN/m)	$C_{\text{moor},22}$ (kN/m)	$C_{\text{moor},66}$ (kN m/rad)
1	HMSF	800	5 %	Yes	16	1,653	1,087	13,621,689
2	HMSF	1100	5 %	Yes	16	2,140	1,402	17,565,107
3	HMSF	800	10 %	Yes	16	1,894	1,249	15,645,042
4	HMSF	1100	10 %	Yes	16	2,600	1,714	21,474,770
5	HMSF	800	5 %	Yes	14	1,484	858	10,721,001
6	HMSF	1100	5 %	Yes	14	1,932	1,107	13,830,881
7	HMSF	800	10 %	Yes	14	1,696	985	12,311,456
8	HMSF	1100	10 %	Yes	14	2,328	1,352	16,899,034
9	HMSF	800	5 %	Yes	12	1,495	570	7,011,916
10	HMSF	1100	5 %	Yes	12	1,938	744	9,163,700
11	HMSF	800	10 %	Yes	12	1,712	650	7,991,602
12	HMSF	1100	10 %	Yes	12	2,351	892	10,970,479
13	Polyester/PP	800	5 %	No	16	1,132	776	9,723,958
14	Polyester/PP	800	10 %	No	16	1,478	1,013	12,702,696
15	Polyester/PP	1100	5 %	No	16	1,729	1,185	14,856,056
16	Polyester/PP	1100	10 %	No	16	2,027	1,390	17,418,929
17	Polyester/PP	800	5 %	No	14	977	612	7,677,589
18	**Polyester/PP**	**800**	**10 %**	**No**	**14**	**1,276**	**799**	**10,029,463**
19	Polyester/PP	1100	5 %	No	14	1,492	935	11,729,657
20	Polyester/PP	1100	10 %	No	14	1,750	1,096	13,753,183
21	Polyester/PP	800	5 %	No	12	1,015	365	4,451,790
22	Polyester/PP	800	10 %	No	12	1,326	477	5,815,505
23	Polyester/PP	1100	5 %	No	12	1,551	558	6,801,349
24	Polyester/PP	1100	10 %	No	12	1,818	654	7,974,675
Minimum, Polyester/PP						977	365	4,451,790
Maximum, Polyester/PP						2,027	1,390	17,418,929
Mean, Polyester/PP						1,464	822	10,244,571

The dry test used to identify the pulley damping (Section 4.5) was also performed for these springs, but they were not used in any test.

D.3 Planned Test Matrix

The cruise ship was to be tested in the same way as the container ship, with the same box ballasted to the draft of the cruise ship, which gives a model draft of 108 mm. Three water depths were planned, 11.6, 10.85 and 10.1 m, corresponding to under keel clearances of 3.5, 2.75 and 2.0 m and to T/h of 0.70, 0.75 and 0.80. At each water depth, three lateral gaps of 6, 4 and 3 m were planned, corresponding to G/B of 0.186, 0.124 and 0.093, together with a laterally unconfined case with the model centered in the flume. As for the container ship, the gap of 2 m was excluded (Section 4.1). The resulting twelve cases are listed in Table 32. Each case was to be tested in both sway and yaw.

Table 32: Planned test matrix of the cruise ship at full scale and model scale (λ = 75.2). These cases were prepared but not tested.

		Full scale			Model scale				
Case	Condition	UKC (m)	G (m)	h (m)	UKC (mm)	G (mm)	h (mm)	T/h	G/B
C1	Laterally unconfined	3.5	–	11.6	47	–	154	0.70	–
C2	Near quay	3.5	6	11.6	47	80	154	0.70	0.186
C3	Near quay	3.5	4	11.6	47	53	154	0.70	0.124
C4	Near quay	3.5	3	11.6	47	40	154	0.70	0.093
C5	Laterally unconfined	2.75	–	10.85	37	–	144	0.75	–
C6	Near quay	2.75	6	10.85	37	80	144	0.75	0.186
C7	Near quay	2.75	4	10.85	37	53	144	0.75	0.124
C8	Near quay	2.75	3	10.85	37	40	144	0.75	0.093
C9	Laterally unconfined	2.0	–	10.1	27	–	134	0.80	–
C10	Near quay	2.0	6	10.1	27	80	134	0.80	0.186
C11	Near quay	2.0	4	10.1	27	53	134	0.80	0.124
C12	Near quay	2.0	3	10.1	27	40	134	0.80	0.093